Particles and Cirrus Clouds (PAZI): Overview of results 2000 - 2003

B. Kärcher[*], U. Schumann, S. Brinkop, R. Busen, M. Fiebig, H. Flentje, K. Gierens, J. Graf,
W. Haag, J. Hendricks, H. Mannstein, S. Marquart, R. Meyer, A. Minikin, A. Petzold, M. Ponater,
R. Sausen, H. Schmid, P. Wendling
DLR-Institut für Physik der Atmosphäre, Oberpfaffenhofen, Germany

M. Aigner, P. Frank, K.-P. Geigle, P. Gerlinger, B. Noll, W. Stricker, C. Wahl
DLR-Institut für Verbrennungstechnik, Stuttgart, Germany

U. Schurath, O. Möhler, S. Schaefers, O. Stetzer
Forschungszentrum Karlsruhe, Institut für Meteorologie und Klimaforschung, Karlsruhe, Germany

O. Schrems, G. Beyerle, F. Immler
Alfred-Wegener-Institut für Polarforschung, Sektion Physik und Chemie der Atmosphäre, Bremerhaven, Germany

H. Kruse, A. Döpelheuer, M. Plohr
DLR-Institut für Antriebstechnik, Köln, Germany

C. Schiller, M. Bläsner, M. Krämer, A. Mangold, A. Wollny
Forschungszentrum Jülich, Institut für Stratosphärenchemie, Jülich, Germany

S. Borrmann, J. Curtius, S. Henseler, N. Hock, J. Schneider, S. Weimer
Universität Mainz, Institut für Physik der Atmosphäre, and Max-Planck-Institut für Chemie, Abteilung Wolkenphysik und Chemie, Mainz, Germany

F. Arnold, H. Aufmhoff, K. Gollinger, A. Kiendler, Th. Stilp, S. Wilhelm, K.-H. Wohlfrom
Max-Planck-Institut für Kernphysik, Bereich Atmosphärenphysik, Heidelberg, Germany

C. Timmreck, J. Feichter
Max-Planck-Institut für Meteorologie, Hamburg, Germany

U. Lohmann
Dalhousie University, Department of Physics and Atmospheric Science, Halifax, Nova Scotia, Canada

J. Ström
Stockholm University, Institute of Applied Environmental Research, Stockholm, Sweden

T. Rother
DLR-Deutsches Fernerkundungsdatenzentrum, Oberpfaffenhofen, Germany

ABSTRACT: PAZI is a national research project supported by the German Secretary of Education and Research (BMBF) through the Helmholtz-Gesellschaft Deutscher Forschungszentren (HGF). Research in PAZI is performed in concert with the projects SiA, INCA, PartEmis, and PARTS funded by the European Commission. PAZI investigates the interaction of aerosols with cirrus clouds, with an emphasis on aviation-produced aerosols and contrails, and their impact on atmospheric composition, radiation, clouds, and climate. This overview summarizes important results obtained during the first phase and highlights the following issues. Measurements and models addressing the formation and evolution of black carbon (BC) particles in burners and jet engines; physico-chemical characterization of aircraft-produced BC particles; measured freezing properties of liquid and BC particles; calculated global atmospheric distribution of BC from various sources; observed differences in cirrus properties between clean and polluted air masses; correlations between air traffic and cirrus cloud cover deduced from satellite observations; process

---

[*] *Corresponding author:* Bernd Kärcher, DLR-Institut für Physik der Atmosphäre, Oberpfaffenhofen, D-82234 Weßling, Germany. Email: bernd.kaercher@dlr.de

studies of aerosol-cirrus interactions; parameterization of cirrus cloud formation; representation of ice supersaturation and cirrus clouds in a climate model and possible aviation impact on global cirrus properties.

1 THE PAZI PROJECT

The project studied the formation of soot particles and other aerosols in jet engines and in the atmosphere, their influence on the formation of the ice phase in contrails and cirrus clouds, and their impact on air composition, cirrus, and climate. It provided a first estimate of the contribution of aviation to changes of the upper tropospheric aerosol and ice particle budget.

To achieve these goals, the participating teams employed highly innovative and complementary methods: combustion test facility, aerosol/cloud chamber, ground-based lidar, research aircraft, satellite sensors, process and climate models. One cornerstone of the project was the close collaboration with projects funded externally by the European Commission and other agencies. Partners from industry such as Lufthansa, MTU, and Rolls-Royce Germany also contributed to PAZI.

Work in PAZI was organized in four main workpackes, the results of which are presented in Section 2 and summarized in Section 3. The workpackages contained several subprojects, each of which was represented by a responsible scientist. Collaboration within and between the subprojects and workpackages proved to be very fruitful, resulting in a large number of joint publications summarized in Section 4 (as of fall 2003).

2 WORKPACKAGE RESULTS

It is not possible to cover every single result of a large-scale project in the limited space available in workshop proceedings. What follows is a brief overview of some of the highlights of PAZI and its associated EU projects.

2.1 *Soot emissions and aerosol precursors*

This workpackage consists of three subprojects dealing with soot particle formation and prediction of global, fleet-averaged aerosol emission indices (Plohr et al., 2000; Döpelheuer, 2000, 2002; Kärcher et al., 2000; Kunz et al., 2001; Braun-Unkhoff et al., 2001; Noll et al., 2002; Schumann et al., 2002; Böhm et al., 2003; Krüger et al., 2003; Wahl and Aigner, 2003). Measurement campaigns were carried out in laboratory flames, behind real jet engines and segments of combustors (hot end simulator), and in DLRs novel high pressure combustor test facility Stuttgart (HBK-S). The various techniques employed allowed the teams to characterize exhaust gas and aerosol chemical speciation as well as size distribution and state of mixing of exhaust aerosols.

The laminar coflame burner fueled with various non-methane hydrocarbons was used to measure temperature and soot volume mixing ratios. With this device, basic soot formation and oxidation processes were systematically studied as a function of operating pressure and fuel stoichiometry. With the data base set up over three years, a kinetic soot model describing soot formation was considerably improved. The HBK-S contains a subscale combustion chamber that operates with high mass fluxes, fully turbulent under high pressures, and with kerosene. It was shown that this device produces soot particles with size distributions similar to those measured in flight.

The combustor measurements carried out within PartEmis confirmed the weak dependence of soot emissions on the fuel sulfur content known from airborne campaigns, but more clearly revealed that exhaust soot contains significant amounts of organic material, besides fully oxidized sulfur. This enhances the hygroscopicity of soot particles and may probably influence their ice-nucleating behavior. Suprisingly, a new electrically charged soot mode at very small sizes (<10 nm in diameter) has been detected in mass spectrometric data of chemi-ions and carbon-containing particles and, independently, in measurements of the size distribution. The role of these ultrafine soot particles in ice formation is unclear and will remain under scrutiny.

An empirical model to estimate mass and number emission indices, size distributions, and total surface area concentrations of soot particles emitted by aircraft engines in flight conditions has been

developed. This model requires only a few basic parameters as input, namely pressure and temperature at the combuster inlet and soot mass concentration at the combustor exit, which are correlated with the above soot properties. Using this correlation model in conjunction with the DLR fuel usage inventory from 1992, fleet-averaged global spatial and temporal profiles of soot emission quantities have been generated for use in the ECHAM general circulation model (see Section 2.4).

2.2 *Ice formation in the atmosphere*

This workpackage integrates four subprojects dealing with the measurement of freezing processes in atmospheric aerosols in cirrus conditions (Szakáll et al., 2001; Gierens et al., 2002; Ovarlez et al., 2002; Möhler et al., 2003; Kärcher and Haag, 2003; Haag et al., 2003a/b; Ström et al., 2003; Kärcher, 2003). A key tool to study ice nucleation in PAZI - with many instruments simultaneously determining thermodynamic consitions, gas concentrations, and the state of aerosol and ice particles - is the aerosol-cloud chamber AIDA in Karlsruhe. Data from the Microwave Limb Sounder (MLS) were analyzed to provide a global view of ice supersaturated regions. Ice supersaturation was measured on the cloud scale with aircraft in relatively clean and relatively polluted air masses during the INCA project.

Measurements in the AIDA very closely mimic real atmospheric conditions prevailing in cirrus or polar stratospheric ice clouds in terms of temperature, relative humidity, and cooling rate conditions. The ability of the numerical simulations carried out with DLRs microphysical cirrus model APSC (Advanced Particle Simulation Code) to provide detailed explanations of the observed formation of ice in supercooled aqueous sulfuric acid particles greatly increased confidence in attempts to model this process under real atmospheric conditions, provided that accurate temperature and humidity measurements are available. It was found that the threshold values of relative humidity for homogeneous freezing from recent laboratory studies, however, may not exactly hold when applied to atmospheric conditions, as enhanced supersaturations and non-equilibrium compositions of the largest liquid particles caused by rapid cooling and low temperatures can lead to somewhat higher values than determined assuming equilibrium conditions.

Besides supercooled liquid particles, heterogeneous ice formation triggered by pure and coated soot and mineral dust particles was also observed in the AIDA. The measurements indicate that these ice nuclei may initiate the formation of the ice phase at relative humidities over ice some 25% below the homogeneous thresholds (>145%). Interpretation of these data sets is ongoing, and more coordinated measurements and detailed comparisons are needed to understand existing differences between available laboratory data sets for soot and dust aerosols.

The fact that supersaturation of ice in the upper troposphere and tropopause region is a global phenomenon was corroborated by analyses of MLS data. For example, at 215 hPa, ice supersaturation is seen not only in the tropical and polar regions, but is also common at midlatitudes, in particular along the storm tracks. Naturally, these satellite data do not capture local variability. High supersaturations up to the homogeneous freezing thresholds have been measured in situ near but outside of and inside cirrus clouds during INCA. It was found that the onset of freezing over Prestwick occurred at relative humidities over ice significantly lower (at ~130%) than required for homogeneous freezing, suggesting that the northern hemisphere background aerosol over Prestwick exhibited signatures of pollution in terms of cirrus nucleation, in contrast to the data taken over Punta Arenas in the southern hemisphere. The ice formation mechanisms at work there likely involved a limited number of efficient heterogeneous ice nuclei. The most likely cause for the observed difference in the data sets are differences in chemical and morphological particle properties.

2.3 *Measurements of aerosols and cirrus clouds*

This workpackage encompasses three subprojects (Rother et al., 2001; Baehr et al., 2002; Gayet et al., 2002; Kärcher, 2002; González et al., 2002; Marquart and Mayer, 2002; Immler and Schrems, 2002a/b, 2003; Immler, 2003; Kärcher and Ström, 2003; Mannstein and Schumann, 2003; Minikin et al., 2003; Meyer et al., 2002, 2003; Seifert et al., 2003a/b/c). The main objective was to characterize aerosols and cirrus clouds in the atmosphere using a wide range of instruments: the large set of meteorological, chemical, optical, and microphysical probes employed in the INCA campaigns, Aerodyne's aerosol mass spectrometer operated by the University of Mainz, AWIs

Mobile Aerosol Raman Lidar (MARL), DLRs aerosol and water vapor lidars, and remote sensing data from METEOSAT and ATSR-2 (Along Track Scanning Radiometer).

Vertical profiles of aerosol properties were taken at northern and southern hemisphere midlatitudes and in the tropics. The midlatitude data sets show surprisingly high concentrations of non-volatile particles at the respective tropopause, probably indicating that soot or dust particles reach these altitudes via complex transport processes in the lower(most) stratosphere. Ambient concentrations of nonvolatile condensation nuclei at 10-12 km altitude are ~35 cm^{-3} (Prestwick) and ~12 cm^{-3} (Punta Arenas). This demonstrates the potential for insoluble particles from natural and anthropogenic sources to influence the formation of cirrus clouds.

The counterflow virtual impactor (CVI) allowed the INCA team to accurately determine the total number density of ice crystals, down to the aerodynamic size range of a few μm. The derived distributions of number density show a predominant peak at values 0.1-10 cm^{-3} and a broad feature extending to the detection limit of ~0.3 l^{-1}. The primary maximum at high concentrations is very likely caused by homogeneous freezing in vertical wind fields at times generated by rapid mesoscale temperature fluctuations and occasionally by convection. The broad feature at lower concentrations is determined by the variability in cooling rates, dynamically-induced dilution of cloudy air parcels, sedimenting ice crystals, and, in the case of the Prestwick data, heterogeneous freezing processes. It was inferred that buoyancy waves with mean wave periods of 10-20 min (horizontal length scales of several 10 km) induce mean updraft speeds of 25-35 cm/s were responsible for the generation of the high number densities of small (<20 μm) ice particles in young cirrus. Such high cooling rates tend to minimize the impact of heterogeneous freezing on the total crystal number density (Section 2.2).

These results have important implications for climate studies. Climate change may bring about changes in the global distribution of updraft speeds, air mass temperatures, and aerosol properties. These changes could significantly modify the probability distribution of cirrus ice crystal concentrations. In any effort to ascribe cause to trends of cirrus properties, a careful evaluation of dynamical changes in cloud formation should be done before conclusions regarding the role of other anthropogenic factors, such as changes in aerosol composition, are made.

Mass spectrometric measurements were performed in one of the PAZI field campaigns carried out over Central Europe. The data confirm that sulfate is a prominent chemical constituent of accumulation mode aerosol there, and that aerosol nitrate was very low during these observations. The OLEX lidar detected an extremely tenuous cirrus cloud at 52°N/10°E at an altitude of 13 km. The cloud was geometrically thin and optically invisible: it barely showed up in the backscatter signal at 523 nm wavelength, but clearly showed backscatter signal and volume depolarisation at 1064 nm. The H$_2$O lidar was operated simultaneously and recorded mixing ratios near 15-20 ppm. A rough analysis suggests that cirrus particles of 2-4 μm mean radius caused the aerosol lidar signals. Taken together, the observed midlatitude subvisible cirrus cloud appears to be comparable to the ultrathin tropical tropopause clouds detected during APE/THESEO in 1999 – an interesting finding that requires further studies but demonstrates how little is actually known about this type of clouds.

The MARL recorded a large data set of cirrus cloud optical depths during INCA. Like OLEX, this lidar is sensitive to even very thin cirrus and can detect cloud with optical depths as low as several 0.0001 in the visible. The probability distributions of cirrus optical depth over Punta Arenas and Prestwick are similar, peaking around 0.2, the largest value being ~7. However, the distribution is skewed towards small optical depths, and about 1/3 of the measurements revealed the presence of subvisible cirrus with values < 0.02. These lidar studies thus confirm the surprisingly high frequencies of occurrence of subvisible cirrus clouds at midlatitudes reported earlier from measurements taken at the Observatoire Haute Provence, France.

The cirrus cloud cover over Europe was determined with the help of METEOSAT data in conjunction with actual air traffic movement data provided by EUROCONTROL. Typical background cirrus coverages amount to 20-25% in this area. Both data sets were correlated, revealing a linear relationship between coverage and mean air traffic density, which saturates at the highest traffic densities near 30-35% coverage. This result could be explained by persistent contrails being spread out through the action of wind shear, i.e., the generation of contrail cirrus, although indirect effects caused by freezing of soot particles without contrail formation or natural cirrus formation in the flight corridors cannot be fully ruled out. By implication, this study confirms the frequent presence and large extent of ice-supersaturated regions in the upper troposphere.

One subproject spent efforts on improving retrievals of cirrus parameters in the presence of lower level water clouds. A convincing case study was analyzed with ATSR-2 data during INCA. Yet another improvement concerned the use of ATSR-2 reflectances from the 0.87 μm and 1.6 μm channels to retrieve optical depth and effective particle radius in frontal cirrus over the North Sea. The APOLLO cloud classification tool was used to detect cirrus over sea and the cirrus properties were then retrieved by comparing the radiances calculated by the comprehensive radiative transfer package libRadtran with the radiances measured by the ATSR-2.

2.4 *Modeling of aerosols and cirrus clouds*

This workpackage integrates three subprojects dealing with process studies and global modeling (Ponater et al., 2002; Lin et al., 2002; Lohmann and Kärcher, 2002; Kärcher and Lohmann, 2002a/b, 2003; Lohmann et al., 2003; Gierens, 2003; Marquart et al., 2003; Hendricks et al., 2003a/b; Lauer et al., 2003). Two subprojects devoted their work to interpreting observations from INCA and MOZAIC, improving microphysical cloud models, and developing innovative parameterization schemes used in the climate model ECHAM. The global modeling subproject synthesized results from all workpackages and provided a first preliminary global assessment of soot-cirrus interaction.

Physically-based parameterizations of homogeneous freezing, heterogeneous immersion freezing, and initial growth of the pristine ice crystals were developed and validated with parcel model simulations. The DLR aerosol/cirrus model APSC and the cloud-resolving model MESOSCOP participated in model intercomparison exercises in the frame of the GEWEX (Global Energy and Water Cycle Experiment) Cloud System Study (GCSS) activity. Both, parameterizations and numerical solutions reveal a strong dependence of the number of ice crystals formed on the vertical velocity and the temperature. Aerosol size effects are comparatively less important, except for very efficient ice nuclei. Using the homogeneous scheme, the first interactive simulations of ice-supersaturation and cirrus were carried out in ECHAM, addressed further below.

Liquid particles may compete with heterogeneous ice nuclei during cirrus formation, as it was probably the case over Prestwick during INCA. Which particle type dominates depends on the relative concentrations, sizes, and freezing properties of the aerosol particles, the temperature and spectrum of vertical winds. The critical number densities of ice nuclei above which homogeneous freezing is suppressed were calculated analytically. Evaluating this solution at typical conditions prevailing during INCA (freezing temperature 222 K, mean updraft speed 20-30 cm/s, heterogeneous ice nucleation at 130%) reveals that less than 0.03-0.08 ice nuclei per cm^3 of air must have been present during the measurements, because homogeneous freezing did take place. It was concluded from the Prestwick observations that heterogeneous ice nuclei triggered the first ice particles but was not the dominant freezing mode (see Sections 2.2 and 2.3), consistent with this estimate. Efforts to corroborate this hypothesis with detailed microphysical simulations are underway.

The implementation of the new cirrus parameterization and the simultaneous abandonment of the frequently used saturation adjustment scheme resulted in the first calculations of global relative humidity in ice-supersaturated regions. Comparisons with MOZAIC data showed that the typical, quasi-exponential shape of the distribution function could be reproduced by the model. Previously, excess humidity created during one time step was removed instantaneously and defined as cloud ice. Basic cirrus parameters such as the total number of crystals and the effective radius used in subsequent radiative calculations were prescribed. With the new parameterizations, the simulated ice water contents are lower and the total crystal concentrations are significantly higher than those computed with the standard saturation adjustment schemes, in better agreement with observations.

The improved cloud scheme enables a self-consistent treatment of cirrus, rendering new studies of cirrus cloud-triggered feedbacks in the climate system possible. It was shown that even very strong enhancements of the background sulfate aerosol mass caused by the Mount Pinatubo eruption likely caused only weak changes in cirrus properties, consistent with a recent reevaluation of ISCCP (International Satellite Cloud Climatology Project) data. However, alterations of the properties of very thin and subvisible cirrus by volcanic eruptions could not be excluded. This implies that the initially very small (5-10 nm) aviation-produced volatile aerosols, albeit present in relatively high number concentrations, do not exert any significant impact on cirrus cloud formation.

The global distribution of black carbon soot was reevaluated with the global model ECHAM. The simulations were based on updated emission inventories, including the aircraft soot emission

model described in Section 2.1. It was found that several 0.1 cm^{-3} soot particles in the upper troposphere and tropopause region originate from aircraft emissions (annual mean figure); compared to the <0.03-0.08 cm^{-3} heterogeneous ice nuclei that influenced cirrus formation over Prestwick (see above), these emissions seem to be sufficiently high to impact cirrus formation in principle, provided that a corresponding fraction of the soot particles act as efficient ice nuclei. The exact magnitude of the calculated aircraft-induced perturbations of the soot budget depends on the relative contributions of the other black carbon sources and on details of soot ageing processes in the atmosphere on time scales of several weeks, both of which are not well known.

A first attempt to calculate the global impact of aircraft soot emissions on cirrus was also undertaken at the very end of the project. For this purpose, two scenarios were defined. The default scenario calculates cirrus formation caused by homogeneous freezing only. This is contrasted with a scenario where heterogeneous freezing of aircraft-emitted soot particles is prescribed, but only in regions where the aircraft soot concentrations exceed 0.5 cm^{-3} (to compensate for errors in the simulated vertical winds that are too low compared with observations); otherwise cirrus form homogeneously as in the first case. The soot increase by aircraft emissions was maximized by assuming minimal particle losses during ageing. In treating this indirect effect of soot-cirrus interactions, the direct effect of spreading contrails (as noted in Section 2.3) has been neglected in these studies.

By comparing annually averaged results from ten years of ECHAM simulations, total ice crystal concentrations are found to be reduced by several tens of percent at northern hemisphere midlatitudes. This is explained by the fact that the assumed soot threshold concentration above which homogeneous freezing is supressed at the prevailing model updraft speeds is frequently surpassed by aircraft emissions. In another conceivable scenario, where soot particles (irrespective of their origin) as well as mineral dust particles can serve as heterogeneous ice nuclei, aviation leads to enhancements of ice crystal concentrations. Feedbacks of the cirrus changes on cloud cover have not been considered in the two scenarios. However, the ECHAM results obtained here reveal the potential of aircraft-induced soot particles to cause significant changes in cirrus microphysical properties.

3 SUMMARY AND CONCLUSIONS

- Among all exhaust particles, soot is key in further studies of potential aerosol-cirrus interactions
- Kinetic algorithms improve the prediction of soot physical properties in combustion models
- Accurate measurements better define the chemical composition and the size distributions of soot particles emitted by aircraft jet engines
- Innovative measurements in an aerosol/cloud chamber suggest early freezing of soot particles in cirrus conditions
- Interpretation of freezing experiments in the chamber increases confidence in the current ability to model homogeneous freezing and growth of small ice crystals in cirrus
- In-situ studies unambiguously confirm the presence of high number densities of small ice crystals in cirrus, tied to homogeneous freezing
- Aircraft-based, size-resolved chemical analysis of aerosol particles in the accumulation mode become available, providing important information on freezing aerosols in future campaigns
- Field measurements reveal mesoscale variability in vertical velocities as the key factor controlling cirrus formation
- Lidar studies confirm surprisingly high frequencies of occurrence of midlatitude subvisual cirrus
- Retrieval algorithm allows remote sensing of cirrus cloud optical properties in the presence of low level stratus
- Satellite analysis reveals close correlation between cirrus cloud cover changes and air traffic density
- Global model studies better constrain the apportionment of black carbon soot to a large number of sources, including aircraft
- Freezing parameterization enables more realistic predictions of ice supersaturation and cirrus clouds in global models

- First preliminary global assessment of soot-cirrus interaction shows potentially significant indirect impact of aircraft soot on cirrus crystal concentrations, if the effect is maximized

Future progress in the area of aerosol-cirrus-radiation interaction depends crucially on a better understanding of
- small-scale dynamical variability;
- indirect aerosol effects on cirrus;
- cirrus radiative properties and cover;
and the representation of these effects in global atmospheric models.

The viewgraphs of the invited talk presented at the workshop are available under http://www.pa.op.dlr.de/aac/. Most of the material presented here has been published in the open literature and we refer to the list of references for more details. In addition, the following contributions in this volume provide further information: Wahl et al., Petzold et al. (Section 2.1); Möhler et al., Mangold et al. (Section 2.2); Immler et al., Mannstein et al. (Section 2.3); Marquart et al., Hendricks et al. (Section 2.4).

REFERENCES

Arnold, F., Th. Stilp, R. Busen, and U. Schumann. Jet engine exhaust chemiion measurements: Implications for gaseous SO_3 and H_2SO_4. *Atmos. Environ., 32,* 3073-3077, 1998.

Arnold, F., K.-H. Wohlfrom, M.W. Klemm, J. Schneider, K. Gollinger, and U. Schumann. First gaseous ion composition measurements in the exhaust plume of a jet aircraft in flight: Implications for gaseous sulfuric acid, aerosols, and chemiions. *Geophys. Res. Lett., 25,* 2137-2140, 1998.

Arnold, F., J. Curtius, B. Sierau, V. Bürger, and R. Busen. Detection of massive negative chemiions in the exhaust plume of a jet aircraft in flight. *Geophys. Res. Lett., 26,* 1577-1580, 1999.

Arnold, F., A. Kiendler, V. Wiedemer, S. Aberle, Th. Stilp, and R. Busen. Chemiion concentration measurements in jet engine exhaust at the ground: Implications for ion chemistry and aerosol formation in the wake of a jet aircraft. *Geophys. Res. Lett., 27,* 1723-1726, 2000.

Baehr, J., H. Schlager, H. Ziereis, P. Stock, P. van Velthoven, R. Busen, J. Ström, and U. Schumann. Aircraft observations of NO, NO_y, CO, and O_3 in the upper troposphere from 60ºN to 60ºS – Interhemispheric differences at midlatitudes. *Geophys. Res. Lett., 30,* 1598, doi:10.1029/2003GL016935, 2003.

Braun-Unkhoff, M., und P. Frank. *Untersuchungen zum Start der Rußbildung bei hohen Drücken*, VDI Berichte 1629, 467, VDI Verlag Düsseldorf, 2001.

Böhm, H., M. Braun-Unkhoff, and P. Frank. *Investigations on Initial Soot Formation at High Pressure*, Progress in Computational Fluid Dynamics, Vol.3, No.2-4, in press, 2003.

Döpelheuer, A. *Aircraft Emission Parameter Modelling*, Dossier "Aviation and the Environment" in: Air & Space Europe, Editions Elsevier, ISSN 1290-0958, May-June 2000.

Döpelheuer, A., *Anwendungsorientierte Verfahren zur Bestimmung von CO, HC und Ruß aus Luftfahrttriebwerken*. Dissertation, DLR-FB 2002-10, DLR Institut für Antriebstechnik, Köln, 2002.

Eichkorn, S., K.-H. Wohlfrom, F. Arnold, and R. Busen. Massive positive and negative chemiions in the exhaust of an aircraft jet engine at ground level: Mass distribution measurements and implications for aerosol formation. *Atmos. Environ., 36,* 1821-1825, 2002.

Gayet, J.-F., F. Auriol, A. Minikin, J. Ström, M. Seifert, R. Krejci, and A. Petzold, G. Febvre, and U. Schumann. Quantitative measurement of the microphysical and optical properties of cirrus clouds with four different in situ probes: Evidence of small ice crystals. *Geophys. Res. Lett., 29,* 2230, doi:10.1029/ 2001GL014342, 2002.

Gierens, K.M., M. Monier, and J.-F. Gayet. The deposition coefficient and its role for cirrus clouds. *J. Geophys. Res., 108,* 4069, doi:10.1029/2001JD001558, 2003.

Gierens, K. On the transition between heterogeneous and homogeneous freezing. *Atmos. Chem. Phys., 3,* 437-446, 2003.

González, A., P. Wendling, B. Mayer, J.-F. Gayet, and T. Rother. Remote sensing of cirrus cloud properties in the presence of lower clouds: An ATSR-2 case study during the Interhemispheric Differences in Cirrus Properties From Anthropogenic Emissions (INCA) experiment. *J. Geophys. Res., 107,* doi:10.1029/ 2002JD002535, 2002.

Gysel, M., S. Nyeki, E. Weingartner, U. Baltensperger, H. Giebl, R. Hitzenberger, A. Petzold, and C.W. Wilson. Properties of jet engine combustion particles during the PartEmis experiment: Hygroscopicity at subsaturated conditions. *Geophys. Res. Lett.*, *30,* doi:10.1029/2003GL016896, 2003.

Haag, W., B. Kärcher, S. Schaefers, O. Stetzer, O. Möhler, U. Schurath, M. Krämer, and C. Schiller. Numerical simulations of homogeneous freezing processes in the aerosol chamber AIDA. *Atmos. Chem. Phys., 3,* 195-210, 2003a.

Haag, W., B. Kärcher, J. Ström, A. Minikin, U. Lohmann, J. Ovarlez, and A. Stohl. Freezing thresholds and cirrus cloud formation mechanisms inferred from in situ measurements of relative humidity, *Atmos. Chem. Phys., 3,* in press, 2003b.

Hendricks, J., B. Kärcher, A. Döpelheuer, J. Feichter, and U. Lohmann. Simulating the global atmospheric black carbon cycle: A revisit to the contribution of aircraft emissions, in preparation, 2003a.

Hendricks, J., B. Kärcher, and U. Lohmann. Potential impact of aviation-induced soot particles on cirrus clouds: Global model studies with the ECHAM GCM, in preparation, 2003b.

Hitzenberger, R., H. Giebl, A. Petzold, M. Gysel, S. Nyeki, E. Weingartner, U. Baltensperger, and C.W. Wilson. Properties of jet engine combustor particles during the PartEmis experiment. Hygroscopic properties at supersaturated conditions. *Geophys. Res. Lett.*, *30,* doi:10.1029/2003GL017294, 2003.

Immler, F., and O. Schrems. LIDAR measurements of cirrus clouds in the northern and southern hemisphere during INCA (55°N, 53°S): A comparative study. *Geophys. Res. Lett.*, *29,* 1809, doi:10.1029/ 2002GL015077, 2002a.

Immler, F., and O. Schrems. Determination of tropical cirrus properties by simultaneous LIDAR and radiosonde measurements. *Geophys. Res. Lett*., *29,* doi:10.1029/2002GL015076, 2002b.

Immler, F., and O. Schrems. Vertical profiles, optical and microphysical properties of Saharan dust layers determined by a ship-borne lidar. *Atmos. Chem. Phys. Discuss., 3,* 2707-2737, 2003.

Immler, F. A new algorithm for simultaneous ozone and aerosol retrieval from tropospheric DIAL measurements, *Appl. Phys., B76,* doi:10.1007/s00340-003-1157-z, 593-596, 2003.

Jensen, E. J., O.B. Toon, S.A. Vay, J. Ovarlez, R. May, P. Bui, C.H. Twohy, B. Gandrud, R.F. Pueschel, and U. Schumann. Prevalence of ice-supersaturated regions in the upper troposphere: Implications for optically thin ice cloud formation. *J. Geophys. Res.*, 106, 17253-17266, 2001.

Kärcher, B., R.P. Turco, F. Yu, M.Y. Danilin, D.K. Weisenstein, R.C. Miake-Lye, and R. Busen. A unified model for ultrafine aircraft particle emissions. *J. Geophys. Res., 105,* 29379-29386, 2000.

Kärcher, B. Properties of subvisible cirrus clouds formed by homogeneous freezing. *Atmos. Chem. Phys.*, *2,* 161-170, 2002.

Kärcher, B., and U. Lohmann. A parameterization of cirrus cloud formation: Homogeneous freezing of supercooled aerosols. *J. Geophys. Res., 107,* 4010, doi:10.1029/2001JD000470, 2002a.

Kärcher, B., and U. Lohmann. A parameterization of cirrus cloud formation: Homogeneous freezing including effects of aerosol size. *J. Geophys. Res*., *107,* 4698, doi:10.1029/2001JD001429, 2002b.

Kärcher, B. Simulating gas-aerosol-cirrus interactions: Process-oriented microphysical model and applications, *Atmos. Chem. Phys. Discuss., 3,* 4129-4181, 2003.

Kärcher, B., and U. Lohmann. A parameterization of cirrus cloud formation: Heterogeneous freezing. *J. Geophys. Res*., *108,* 4402, doi:10.1029/2002JD003220, 2003.

Kärcher, B., and J. Ström. The roles of dynamical variability and aerosols in cirrus cloud formation, *Atmos. Chem. Phys.*, *3,* 823-838, 2003.

Kärcher, B., and W. Haag. Factors controlling upper tropospheric relative humidity, *Ann. Geophys., 21,* in press, 2003.

Krüger, V., K.P. Geigle, W. Stricker, and M. Aigner. Soot particle size measurements with laser-induced incandescence: Validation of the signal interpretation model in flames, in preparation, 2003.

Kunz, O., B. Noll, R. Lückerath, M. Aigner, and S. Hohmann. Computational combustion simulation for an aircraft model combustor. *AIAA* paper 2001-3706, 2001.

Lauer, A., J. Hendricks, B. Schell, H. Hass, J. Feichter, and S. Metzger. Global modelling of tropospheric aerosols with ECHAM4/MADE, in preparation, 2003.

Lin, R.-F., D.O'C. Starr, P.J. DeMott, R. Cotton, K. Sassen, E. Jensen, B. Kärcher, and X. Liu. Cirrus parcel model comparison project. Phase 1: The critical components to simulate cirrus initiation explicitly. *J. Atmos. Sci., 59,* 2305-2329, 2002.

Lohmann, U., and B. Kärcher. First interactive simulations of cirrus clouds formed by homogeneous freezing in the ECHAM GCM. *J. Geophys. Res., 107*, 4105, doi:10.1029/2001JD000767, 2002.

Lohmann, U., B. Kärcher, and C. Timmreck. Impact of the Mt. Pinatubo eruption on cirrus clouds formed by homogeneous freezing in the ECHAM GCM. *J. Geophys. Res*., *108,* 4568, doi:10.1029/2002JD003185, 2003.

Mannstein, H., and U. Schumann. Contrail cirrus over Europe, submitted manuscript, 2003.

Marquart, S., and B. Mayer. Towards a reliable GCM estimation of contrail radiative forcing. *Geophys. Res. Lett.*, 29, 1179, doi:10.1029/2001GL014075, 2002.

Marquart, S., M. Ponater, F. Mager, and R. Sausen. Future development of contrail cover, optical depth and radiative forcing: impacts of increasing air traffic and climate change. *J. Climate*, 16, 2890-2904, 2003.

Meyer, R., H. Mannstein, R. Meerkötter, U. Schumann, and P. Wendling. Regional radiative forcing by line-shaped contrails derived from satellite data. *J. Geophys. Res., 107,* 4104, doi:10.1029/2001JD000547, 2002.

Meyer, R., R. Büll, C. Leiter, H. Mannstein, S. Marquart, T. Oki, and P. Wendling. Contrail observations over Southern and Eastern Asia in NOAA/AVHRR data and intercomparison to contrail simulations in a GCM. *Int. J. Remote Sensing*, submitted, 2003.

Minikin, A., A. Petzold, J. Ström, R. Krejci, M. Seifert, H. Schlager, P. van Velthoven, and U. Schumann. Aircraft observations of the upper tropospheric fine particle aerosol in the northern and southern hemispheres at midlatitudes. *Geophys. Res. Lett.*, 30, 1503, doi:10.1029/2002GL016458, 2003.

Möhler, O., O. Stetzer, S. Schaefers, C. Linke, M. Schnaiter, R. Tiede, H. Saathoff, M. Krämer, A. Mangold, P. Budz, P. Zink, J. Schreiner, K. Mauersberger, W. Haag, B. Kärcher, and U. Schurath. Experimental investigations of homogeneous freezing of sulphuric acid particles in the aerosol chamber AIDA. *Atmos. Chem. Phys., 3,* 211-223, 2003.

Noll, B., R. Kessler, P. Theisen, H. Schütz, M. Aigner, and S. Hohmann. Flow Field Mixing Characteristics of an Aero-Engine Combustor - Part II: Numerical Simulations. *AIAA* paper 2002-3708, 2002.

Ovarlez, J. J.-F. Gayet, K. Gierens, J. Ström, H. Ovarlez, F. Auriol, R. Busen, and U. Schumann. Water vapour measurements inside cirrus clouds in Northern and Southern hemispheres during INCA, *Geophys. Res. Lett., 29,* 1813, doi:10.1029/2001GL014440, 2002.

Petzold, A., C. Stein, S. Nyeki, M. Gysel, E. Weingartner, U. Baltensperger, H. Giebl, R. Hitzenberger, A. Döpelheuer, S. Vrchoticky, H. Puxbaum, M. Johnson, C.D. Hurley, R. Marsh, and C.W. Wilson. Properties of jet engine combustion particles during the PartEmis experiment: Microphysics and chemistry. *Geophys. Res. Lett., 30,* doi:10.1029/2003GL017283, 2003.

Plohr, M., A. Döpelheuer, and M. Lecht. The gas turbine heat cycle and its influence on fuel efficiency and emissions, Paper 34 in " Gas Turbine Operation and Technology for Land, Sea and Air Propulsion and Power Systems". RTO MP-34, AC/323(AVT)TP/14, 2000.

Ponater, M., S. Marquart, and R. Sausen. Contrails in a comprehensive global climate model: parameterisation and radiative forcing results, *J. Geophys. Res.*, *107,* 10.1029/2001JD000429, 2002.

Rother, T., K. Schmidt, and S. Havemann. Light scattering on hexagonal ice columns. *J. Opt. Soc. Am. A*, *18,* 2512-2517, 2001.

Schumann, U., R. Busen, and M. Plohr. Experimental test of the influence of propulsion efficiency on contrail formation. *J. Aircraft, 37,* 1083-1087, 2000.

Schumann, U. Influence of propulsion efficiency on contrail formation. *Aerosp. Sci. Technol., 4,* 391-401, 2000.

Schumann, U., J. Ström, F. Arnold, T.K. Berntsen, P.M. de F. Forster, J.-F. Gayet, and D. Hauglustaine. Aviation impact on atmospheric composition and climate, in: European Research in the Stratosphere 1996-2000. Chapter 7, EUR 19867, pp. 257-307, European Commission, Brussels, 2001.

Schumann, U. Contrail Cirrus, in: D. K. Lynch, K. Sassen, D. O'C. Starr, and G. Stephens (Eds.), *Cirrus*, Oxford Univ. Press, p. 231-255, 2002a.

Schumann, U. Aircraft Emissions. *Encyclopedia of Global Environmental Change*, Wiley, Vol. 3, 178-186, 2002b.

Schumann, U., F. Arnold, R. Busen, J. Curtius, B. Kärcher, A. Kiendler, A. Petzold, H. Schlager, F. Schröder, and K.-H. Wohlfrom. Influence of fuel sulfur on the composition of aircraft exhaust plumes: The experiments SULFUR 1-7. *J. Geophys. Res., 107,* 4247, doi:10.1029/2001JD000813, 2002.

Seifert, M., J. Ström, R. Krejci, A. Minikin, A. Petzold, J.-F. Gayet, U. Schumann, and J. Ovarlez. In situ observations of aerosol particles remaining from evaporated cirrus crystals: Comparing clean and polluted air masses. *Atmos. Chem. Phys., 3,* 1037–1049, 2003a.

Seifert, M., J. Ström, R. Krejci, A. Minikin, A. Petzold, J.-F. Gayet, H. Schlager, H. Ziereis, U. Schumann, and J. Ovarlez. Aerosol-cirrus interactions: A number based phenomenon at all? *Atmos. Chem. Phys. Discuss., 3,* 3625-3657, 2003b.

Seifert, M., J. Ström, R. Krejci, A. Minikin, A. Petzold, J.-F. Gayet, H. Schlager, H. Ziereis, U. Schumann, and J. Ovarlez. Thermal stability analysis of particles incorporated in cirrus crystals and of non-activated particles in between the cirrus crystals: Comparing clean and polluted air masses. *Atmos. Chem. Phys. Discuss.,* 3, 3659-3679, 2003c.

Starik, A.M., A.M. Savel'ev, N.S. Titova, and U. Schumann. Modeling of sulfur gases and chemiions in aircraft engines. *Aerosp. Sci. Technol., 6,* 63-81, 2002.

Ström, J., M. Seifert, B. Kärcher, J. Ovarlez, A. Minikin, J.-F. Gayet, R. Krejci, A. Petzold, F. Auriol, R. Busen, U. Schumann, W. Haag, and H.-C. Hansson. Cirrus cloud occurrence as a function of ambient relative humidity: A comparison of observations obtained during the INCA experiment, *Atmos. Chem. Phys., 3,* in press*, 2003.

Szakáll, M., Z. Bozóki, M. Krämer, N. Spelten, O. Möhler, and U. Schurath. Evaluation of a photoacoustic detector for water vapor measurements under simulated tropospheric/lower stratospheric conditions, *Environ. Sci. Technol., 35,* 4881-4885, 2001.

Wahl, C., and M. Aigner. Aircraft gas turbine soot emission tests under technically relevant conditions in an altitude test facility and validation of soot measurement techniques. Paper No. GT 2003-38797, *ASME*, 2003.

Ice-nucleating ability of soot particles in UT/LS

J. Suzanne[*],D. Ferry F.
CRMC2-CNRS, Campus de Luminy, Case 913, F-13288 Marseille cedex 9, France

O.B. Popovicheva, N.K. Shonija
Department of Microelectronics, Institute of Nuclear Physics, Moscow State University, Moscow, Russia

Keywords: soot, ice nucleation, atmosphere, cirrus formation, neutron scattering

ABSTRACT: Morphology, microstructure and water adsorbability of laboratory made kerosene soot taken as an aircraft soot surrogate were studied to establish the correlation between the morphology porosity and the ice nucleation ability of the soot surface. Quasi-Elastic Neutron Scattering (QENS) and neutron diffraction (ND) have been used to highlight the dynamics and structure of water/ice confined in the porous soot network. The routine of these experiments roughly followed the evolution of temperature (T) and relative humidity (RH) in the plume and down to UT/LS conditions. There is a depression of the homogeneous nucleation point and ~ 15% of the water is in a highly supercooled state down to 204K. The frozen water is a mixture of amorphous ice probably located in the soot pores coexisting with ice Ih at the soot surface. At 220 K, 75% of ice component inside the soot pores increase the ability of soot to act as secondary ice nuclei for cirrus clouds.

1 INTRODUCTION

In-situ studies have shown that carbonaceous particles are primary components in evaporated contrail residues at cirrus altitudes (Petzhold et al. 1999). Observational and numerical investigations have shown that soot particles may play a role as potential ice nuclei in contrail formation (Kärcher et al. 1996). Enhancement in the occurrence frequency of cirrus clouds up to 10% per decade over North America has attracted the attention of the scientific community on the effect of emitted soot aerosols on contrails and cirrus formation. An unambiguous evidence that soot particles are directly involved in ice formation is difficult to obtain from *in situ* measurements. Hence the nucleating ability of exhaust soot is still poorly understood.

To improve this situation, kerosene flame soot produced by burning aviation kerosene in an oil lamp has been used to mimic the behavior of aircraft engine soot in a laboratory scale procedure (Diehl and Mitra, 1998). Investigations of their ice nucleating ability showed that the kerosene-burner exhaust particles act as immersion freezing nuclei in supercooled exhaust polluted drops at temperatures colder than about 250K. This result support the assumption that contrails observed near threshold formation conditions are formed by frozen water on soot particles (Kärcher et al. 1996). X-ray and neutron scattering studies of the structure of water wetting activated charcoal powder confirmed the formation of the hexagonal Ih and amorphous ices depending on water content (Bellissent-Funel et al., 1996). But a comprehensive study of the kerosene soot microstructure and its role in ice nucleation is still lacking.

This paper is devoted to a study of the structure and dynamics of adsorbed water on kerosene flame soot surface in a wide range of temperatures and relative humidities related to the conditions in expanding plume and in upper troposphere. Quasi-Elastic Neutron Scattering (QENS) and Neutron Diffraction (ND) together with adsorption/structural analysis yield information about water freezing and the ice structure in the kerosene soot pore network.

---

[*] *Corresponding author:* Jean Suzanne, CRMC2-CNRS, Campus de Luminy Case 913, F-13288 Marseille cedex 9, France. Email: suzanne@crmc2.univ-mrs.fr

2 EXPERIMENTS

The soot has been obtained by burning aviation kerosene in a laboratory oil lamp and was collected at a distance of 15-20 cm above the flame. A gravimetric setup equipped with McBain scales as well as a conventional volumetric apparatus were used for C_6H_6 and Kr isotherm adsorption measurements to obtain the surface area and texture characteristics. The internal microstructure of the soot particles has been analyzed by transmission electron microscopy TEM (JEM 2000 FX) with a resolution of 2.8 Å at 200 kV using the phase-contrast imaging method. Holey amorphous carbon films on microgrids were used to support the soot particles. TEM was coupled with X-ray energy dispersive spectroscopy (XREDS) for chemical composition analysis (Popovitcheva et al., 2000).

The neutron experiments were performed at the Laboratoire Leon Brillouin (Saclay, France). Two kinds of experiments have been done : i) Incoherent quasi-elastic neutron scattering (QENS) on the MIBEMOL (G6.2) high–resolution time–of–flight spectrometer ($\lambda = 8$ Å, energy resolution $\Delta E = 39$ μeV), ii) Neutron diffraction (ND) on the two-axes diffractometer 7C.2 ($\lambda = 1{,}10$ Å, $\Delta Q/Q = 10^{-2}$ where Q stands for the scattering wave vector modulus).

QENS allows to measure the rotational and translational mobility of the water molecules through the broadening of the elastic peak. ND gives access to the structure of the soot on the one hand and of the adsorbed water (ice) on the other hand.

A cell with 0.9g of soot was introduced in the sample part of the spectrometers. Normal water H_2O was used for QENS measurements since hydrogen atoms have a large incoherent cross section. Heavy water D_2O has to be used for ND experiments since deuterium atoms have large coherent and week incoherent cross sections. Experiments were carried out for three different amounts of water corresponding to 40, 60 and 100% relative humidity (RH). In the ND experiments we also have condensed a thick ice film on soot at 180K in order to obtain a reference ice Ih spectrum.

The neutron spectra were recorded during about 13 hours when thermodynamical equilibrium was reached. Prior to any spectrum analysis, the background due to the [cell + bare soot sample] was subtracted from the [cell + soot + water] neutron spectrum.

3 RESULTS

3.1 *Soot texture*

The kerosene soot morphology and structure has been described elsewhere (Popovitcheva et al., 2000). Briefly, soot particles have a spherical-like nature with diameters in the 30 to 50 nm range has shown by TEM. They feature disordered graphitic microcrystallites about 2nm wide and thickness of about 1 nm arranged in concentric layers leading to an onion-like structure. It is similar to that of jet engine combustor soot (Popovitcheva et al., 2000). A specific surface area S near 43 m^2/g was determined from the linear BET plot of a Kr isotherm up to $p/p_S \cong 0.3$ (p_S is the saturation vapor pressure) assuming a Kr molecular surface area σ_{Kr} of 0.19 nm^2 (Gregg and Sing, 1982). $S \cong 33$ m^2/g was determined from a C_6H_6 isotherm for the same p/p_S range ($\sigma_{C6H6} \cong 0.43$ nm^2). The Kr adsorption isotherm was classified as Type I and the mechanism of adsorption was discussed in terms of the pore filling Dubinin's theory (Gregg and Sing, 1982). The micropore volume and characteristic energy of adsorption has been determined by means of the fundamental Dubinin-Astakhov equation (Dubinin and Stoeckli, 1980). In the case of kerosene soot, the adsorption isotherms of both Kr and C_6H_6 can be approximated by a complex structure with two types of micropores (Ferry et al. 2002). The volumes of the two micropore sets have been estimated to $W_{01} \cong$ $4 \cdot 10^{-3}$ $cm^{-3}g^{-1}$ and $W_{02} \cong 10^{-2}$ cm^{-3} g^{-1}. The specific behavior of C_6H_6 hysteresis extending down to complete desorption indicates a slit-like nature of the micropores with half widths $x_1 \cong 0.5$ nm and $x_2 \cong 2$ nm that enables one to differentiate the smallest micropores from supermicropores in kerosene soot. Mesopores with size larger than 2 nm exist as cavities between particles. The mesopore volume V_{me} may be roughly estimated as the difference between the total volume of adsorbed amount at $p/p_S \cong 0.95$ and both W_{01} and W_{02} that gives us $V_{me} \approx 4 \cdot 10^{-3} cm^3/g$.

3.2 *Dynamics of water on soot*

The analysis of the QENS spectra is based on the measurement of the elastic peak broadening due to neutrons scattering from the water molecules adsorbed on the soot surface and in the pores. As usual, the single particle dynamical structure factor of water is obtain as a convolution of dynamical structure factors for the translational and rotational motions under the assumption of their decoupling. The theoretical background can be found in the literature (Teixeira et al., 1984; Chen and Teixeira, 1986; Toubin et al., 2001). From this analysis we can determine both the rotational D_r and translational D_t diffusion coefficients of the water molecules and the water liquid-like fraction L_f of the water/ice mixture. The rotational diffusion is characterized by a relaxation time $\tau_r = (6D_r)^{-1}$. We interpret our spectra as resulting from two components: one solid-like, represented by a narrow elastic peak, and one liquid-like, responsible for the wings and represented by a Lorentzian function (Toubin et al., 2001). This allows us to estimate the respective integrated parts of solid and fluid components and thus to obtain the liquid/solid-like fraction L_f. For each experimental condition (T, RH) a set of 10 spectra corresponding to 10 sets of Qs ($0.4 \text{ Å}^{-1} \leq Q \leq 1.48 \text{ Å}^{-1}$) are measured. The spectra were obtained at five different temperatures, 283K, 260K, 245K, 220K and 204K and were normalized to the spectrometer monitor (that is to the number of incident neutrons).

Figure 1 shows typical QENS spectra taken at three temperatures and RH = 100% for Q = 1.25 Å^{-1}. The peak broadening is reduced with decreasing temperature due to the reduction of the water molecules mobility. It indicates that there is a decrease of the translational and rotational diffusion coefficients due to the nucleation of supercooled water in the highly constrained regions of the micropores and supermicropores. This effect causes a depression of the homogeneous nucleation point and therefore maintains some water in a highly supercooled state at 204K.

Table 1 gives the parameters extracted from QENS spectra fits for all examined temperatures at RH=60% and 100%. For comparison, the values τ_r obtained for supercooled bulk water (Teixeira et al., 1984) are shown; one sees that they are 2,5 - 4 times smaller than our values. Hence, the rotational motion of water molecules is more hindered in our soot sample than in bulk water or in the above mentioned hydrophilic adsorbates likely due to the confinement of water in the soot micropores and supermicropores. Strong active sites of oxidized soot particles may also participate to the hindrance of the molecule motion. It should be noted that at 283K 35% of the adsorbed water is in a solid-like state as deduced from the low translational diffusion coefficient ($D = 10^{-6} \text{ cm}^2 \text{ s}^{-1}$).
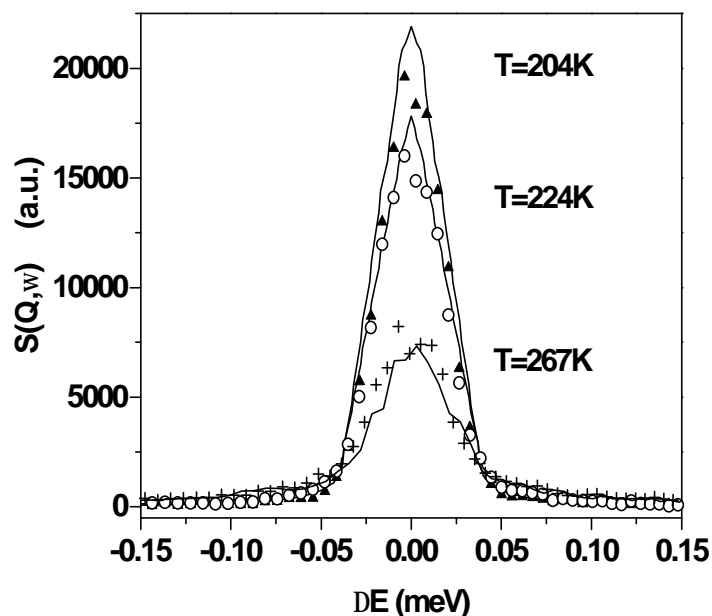

Figure 1. QENS spectra at Q = 1.25 Å and RH = 100% at 267, 224 and 204 K. The scattered intensity $S(Q,\omega)$ of the quasi-elastic peak is plotted versus the energy transfer ΔE.

Table 1 - Translational D_t and rotational D_r diffusion coefficients and rotational relaxation time τ_r for water adsorbed on kerosene soot at RH 60% and 100%.

T, K(°C)	D_t (10^{-5} cm^2/s) 2D isotropic model (Unfrozen water %)	D_t^* (10^{-5} cm^2/s) bulk water	D_r (10^{10} s^{-1})	τ_r (ps)	τ_r^* (ps) bulk water
283(+10)	2±1 (65)	1.25	5±3	0.33	
267(-6)	1±0.5 (60)	0.66	2±1	0.82	1.57
257 (-15)	1±0.5 (50)	0.5	2±1	0.82	1.92
242 (-31)	0.75±0.35 (35)		2±1	0.82	
224 (-49)	0.5±0.25 (30)		1±0.5	1.66	
204 (-69)	0.5±0.25 (15)		0.5±0.25	3.3	

Values marked by * are taken from (Teixeira et al., 1984) for bulk water

3.3 Ice nucleation and structure

The ND spectra at T = 283 K, 260 K and 180 K are shown in Fig. 2 and 3. The spectrum at 283 K features a broad intense peak centered at Q = 1.9 Å^{-1} and two smaller broad peaks at 4 Å^{-1} and 7.8 Å^{-1}. These peaks correspond to the well known structure of liquid water (Chen and Teixeira, 1986). Two spectra are measured at 260 K : i) the 260 K (1) spectrum (fig. 3a) which has been measured during 13 hours after adsorption of the water at 260K followed by 3 hours of equilibrium time and ii) the 260 K (2) spectrum (fig. 3b) which has been measured after the cycle of cooling the soot down to 204 K, measuring spectra at 245 K, 220 K and 204K and warming it up again to 260K. Besides the cycle of cooling down and warming up, about 2 days have elapsed between the two measurements. The 260 K(1) spectrum presents a broad peak centered at Q = 1.73 Å^{-1} and a narrower peak at Q = 2.28 Å^{-1} assigned to the (102) reflection of ice Ih. To explained the broad peak we propose two hypotheses. (*i*) It may be assigned to low density amorphous ice (Chen and Teixeira, 1986) or (*ii*) it comes from diffraction broadening of the three ice reflections (102), (002) and (101).In the latter hypothesis, application of the Scherrer formula leads to crystallite sizes of the order of 4.0 nm. However, one sees that the (102) peak is narrow indicating a crystal growth anisotropy. Such crystallites could form inside the mesopores and (or) on the external surfaces of the soot particles. It should be noted that the (102) reflection is slightly shifted toward low Q's since the expected value for bulk ice Ih is 2.35 Å^{-1} (fig. 3c), which corresponds to an increase of the d_{102} spacing of about 3%.
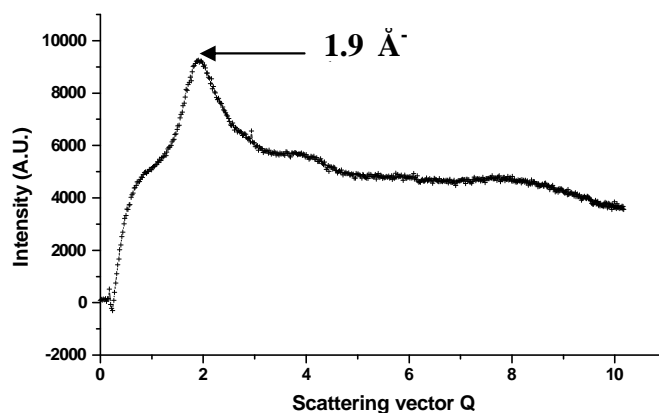

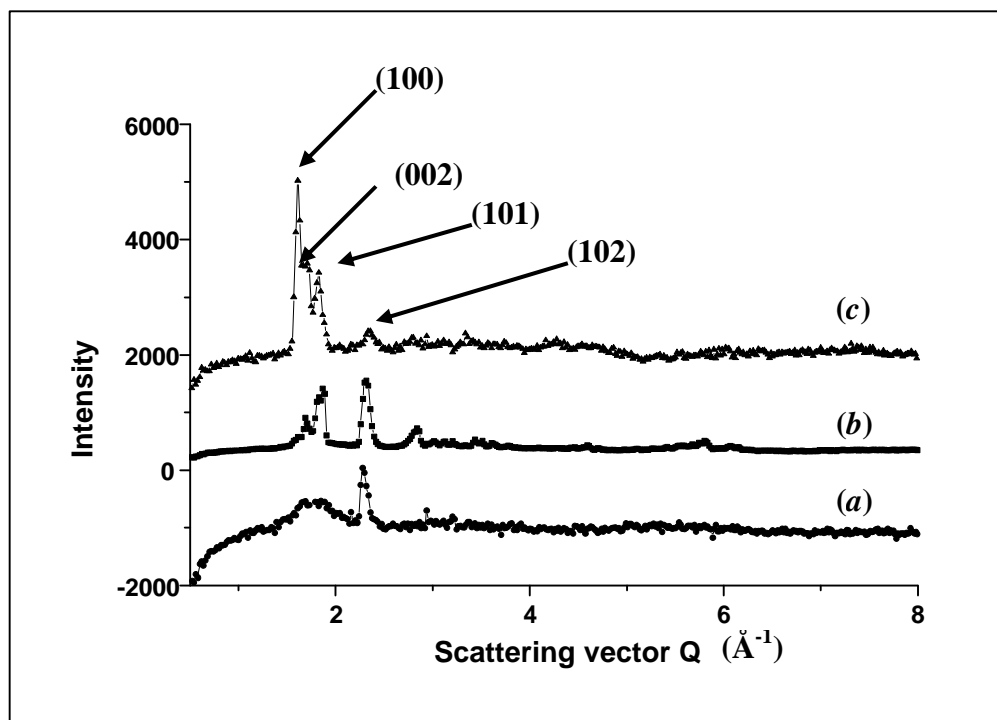Figure 2. Neutron diffraction spectrum of water adsorbed on soot at T = 283 K

Figure 3. Neutron diffraction spectra of water adsorbed on soot at (*a*)T = 260 K (1); (*b*)T= 260 K (2); (*c*)T = 180 K. The 180 K spectrum is characteristic of the ice Ih structure

The 260 K(2) spectrum is quite different from 260 K(1). The broad peak at 1.73 $\mathring{A}^{-1}$ has been replaced by narrower peaks, signature of crystalline ice Ih. It is interesting to remark that even after the annealing cycle, broad wings still persist below the (100), (002) and (101) peaks. That is a remainder of the broad peak observed in the 260 K(1) spectra and centered at Q = 1.73 $\mathring{A}^{-1}$. This broad peak does not exist in the bulk ice spectra as shown in Fig. 3c and can be considered as a remainder of either amorphous ice or small crystallites as explained above.

We would like to point out that in the neutron spectrum at 283K there is also a weak broad peak around 2.7 $\mathring{A}^{-1}$. Such a peak has been observed for low-density amorphous ice (Bellissent-Funel et al., 1996). Since we have found in our QENS experiments that about 35% of adsorbed water is in a solid-like state at 283K, we may wonder whether this solid-like water fraction presents a short range ordered structure close to that of low-density amorphous ice. More experiments are needed to confirm this hypothesis.

4 CONCLUSION AND ATMOSPHERIC IMPLICATIONS

By using two techniques namely quasi-elastic neutron scattering and neutron diffraction, combined with adsorption/texture analysis, we have shown that kerosene soot features a high freezing potential for ice nucleation and existence of a liquid water fraction down to $\cong$ 200 K.

If aircraft- emitted soot particles have properties similar to kerosene soot studied here, we may conclude that at the saturation plume conditions, T=240K, $\approx$ 30% of the water adsorbed is transformed into ice probably in the soot mesopores > 2 nm and on the external surface. But the ice nucleation/growth process is completely suppressed in the soot supermicropores because near 35 % of the water remains liquid under these conditions. At the upper troposphere conditions, at subsaturation level and T $\cong$ 220K, there are stable water/ice components inside the soot pores since 25% of the water content is unfrozen. Moreover, $\approx$ 15% of the water confined in the soot supermicropores may remain liquid down to 200K, temperature of the low stratosphere.

Upon reaching the water supersaturation conditions, ice germs may increase the freezing probability of water nuclei on soot particles and facilitate the growth of large ice crystals in

contrails. Upon evaporation of the aircraft contrail, new ice forming nuclei containing the soot particles may appear in the atmosphere. Retention of ice in the cavities of the residual soot cores after evaporation will serve as germ for secondary nucleation of ice crystals (Hobbs, 1974) which potentially grow into cirrus clouds in the supersaturated air (preactivation effect of cirrus clouds).

We would like to emphasize that recent results obtained with soot collected from a jet engine working under normal take-off and cruise conditions show that this soot is much more hydrophilic than our laboratory kerosene soot (O.B. Popovicheva, unpubl.). This behavior can be related to the high sulfur content of these soot particle. Hence we may infer an even higher ice nucleating ability for real aircraft engine soot.

REFERENCES

Bellissent-Funel, M.-C., Chen, S.H., and J.-M. Zanotti, 1995: Single particle dynamics of water molecules in confined space. *Phys. Rev.* E 51, 4558.

Bellissent-Funel, M.-C., Sridi-Dorbez, R., and L. Bosio, 1996: X-ray and neutron scattering studies of the structure of water at a hydrophobic surface. *J. Chem. Phys.* 104, 10023.

Chen, S.-H., and J. Teixeira, 1986: Structure and dynamics of low temperature water as studied by scattering techniques in *Advances in Chem. Phys.* Vol. 64, I. Prigogine and S.A. Rice (eds), J. Wiley & Sons , New-York.

Diehl, K., and S.K. Mitra, 1998: A laboratory study of the effects of kerosene burner exhaust on ice nucleation and the evaporation rate of ice crystals. *Atm. Environ.* 32, 3145.

Dubinin, M.M., and H.F. Stoeckli, 1980: Homogeneous and heterogeneous micropore structures in carbonaceous adsorbents.. *J. Colloid Interf. Sci.* 75, 34.

Ferry, D., Suzanne, J., Nitsche, S., Popovitcheva, O.B., and N.K. Shonija, 2002: Water adsorption and dynamics on kerosene soot under atmospheric conditions. *J. Geophys. Res.* 107, 4734.

Gregg, S.J., and K.S.W. Sing: 1982: Adsorption, surface area and porosity (2nd ed.), Acad. Press, San Diego

Hobbs P.V., 1974: Ice Physics. Clarendon. Press, Oxford.

Kärcher, B., Peter, Th., Biermann, U.M., and U. Schumann, 1996: The initial composition of jet condensation trails. *J. Atm. Sci.* **53**, 3066.

Petzhold, A., Dopelheuer, A., Brock, C.A., and F.P. Schroder, 1999: In-situ observations and model calculations of black carbon emission by aircraft at cruise altitude. *J. Geophys. Res.* 104, 22171-22181.

Popovitcheva, O.B., Persiantseva, N.M., Trukhin, M.E., Rulev, G.B., Shonija, N.K., Buriko, Y.Y., Starik, A.M., Demirdjian, B., Ferry, D., and J. Suzanne, 2000: Experimental characterization of aircraft combustor soot: microstructure, surface area, porosity and water adsorption. *Phys. Chem. Chem. Phys.* **2**, 4421.

Teixeira, J., Bellissent-Funel, M.C., Chen, S.-H., and A.J. Dianoux, 1984: Dynamics of supercooled water studied by neutron scattering. *J. Phys. (France)* **45**, **C7**, 65.

Toubin, C., Picaud, S., Hoang, P.N.M., Girardet, C., Demirdjian, B., Ferry, D., and J. Suzanne, 2001: Dynamics of ice layers deposited on MgO(001): Quasi-elastic neutron scattering experiments and molecular dynamics simulations. *J. Chem. Phys.* **114**, 6371.

Experimental investigation of homogeneous and heterogeneous freezing processes at simulated UTLS conditions

O. Möhler[*], C. Linke, H. Saathoff, M. Schnaiter, R. Wagner, U. Schurath
Institute of Meteorology and Climate Research, Forschungszentrum Karlsruhe, Germany.

A. Mangold, M. Krämer
ICG-1, Forschungszentrum Jülich, Germany.

1 INTRODUCTION

Ice nucleation (IN) in the UTLS region can occur either by homogeneous freezing of solution droplets below about 235 K, or be heterogeneously induced by so-called ice nuclei. At temperatures below 200 K, homogeneous IN requires high ice supersaturations of up to 60%, which are frequently observed in the upper troposphere (Gierens et al., 2000; Jensen et al., 2001). High updraft velocities favour cirrus formation at the homogeneous freezing threshold. At lower updrafts, however, heterogeneous ice nuclei, e.g. soot particles emitted from aircraft engines, may selectively be activated at lower supersaturation. The pristine ice crystals grow by water uptake, thus eventually limiting the maximum supersaturation to values below the homogeneous freezing threshold. This mechanism could explain optically thin cirrus layers with ice particles of low number concentration and large size. The large coolable and evacuable aerosol chamber AIDA (Aerosol Interaction and Dynamics in the Atmosphere) at Forschungszentrum Karlsruhe can be used as a moderate expansion cloud chamber to study processes of ice formation at simulated cirrus conditions like temperature, cooling rate, and ice supersaturation (Möhler et al., 2003; Haag et al., 2003). In this paper we briefly discuss recent ice nucleation experiments in relevant aerosol systems, e.g. soot particles coated with sulphuric acid and ammonium sulphate layers.

2 EXPERIMENTAL

Experimental methods and the instrumentation of the AIDA cloud chamber facility are described by Möhler et al. (2003) and will only briefly be reviewed here. Figure 1 shows the aluminium aerosol vessel (volume 84 m^3) located in a thermally insulated box that can homogeneously be cooled to any temperature down to 183 K. At constant wall and gas temperature, ice saturation is maintained by a thin ice layer on the chamber walls. Controlled pumping, typically from 1000 to 800 hPa, causes gas expansion and therefore ice supersaturation by adiabatic cooling. Change of ice supersaturation (up to 50 %/min) results from adiabatic cooling as well as heat and water flux from the ice-coated aluminium walls into the chamber volume. Heat and mass flux are mainly driven by the increasing difference between the almost constant wall temperature and the decreasing gas temperature T_g inside the aerosol chamber which is homogeneously mixed with a ventilator, and the difference of the water vapour saturation pressure above the wall ice coating and the water vapour pressure decreasing during pumping and after formation of cold ice particles. The relative humidity with respect to ice (RHi) is calculated from the saturation water vapour pressure at T_g and total water concentration measured with the FISH instrument (Zöger et al., 1999). In the most recent experiments, the interstitial water vapour pressure is also measured in situ by folded-path tunable diode laser absorption. After pumping is stopped at 800 hPa, the gas temperature starts to increase

---

[*] *Corresponding author:* Ottmar Möhler, Forschungszentrum Karlsruhe, Institute for Meteorology and Climate Research, Postfach 3640, 76021 Karlsruhe, Germany. Email: Ottmar.Moehler@imk.fzk.de

by heat flux from the aluminium walls approaching the wall temperature with a time scale of about 15 min. Ice particles evaporate within about the same time period and the chamber can be refilled with synthetic air to atmospheric pressure to start another expansion and ice nucleation cycle with the same aerosol.
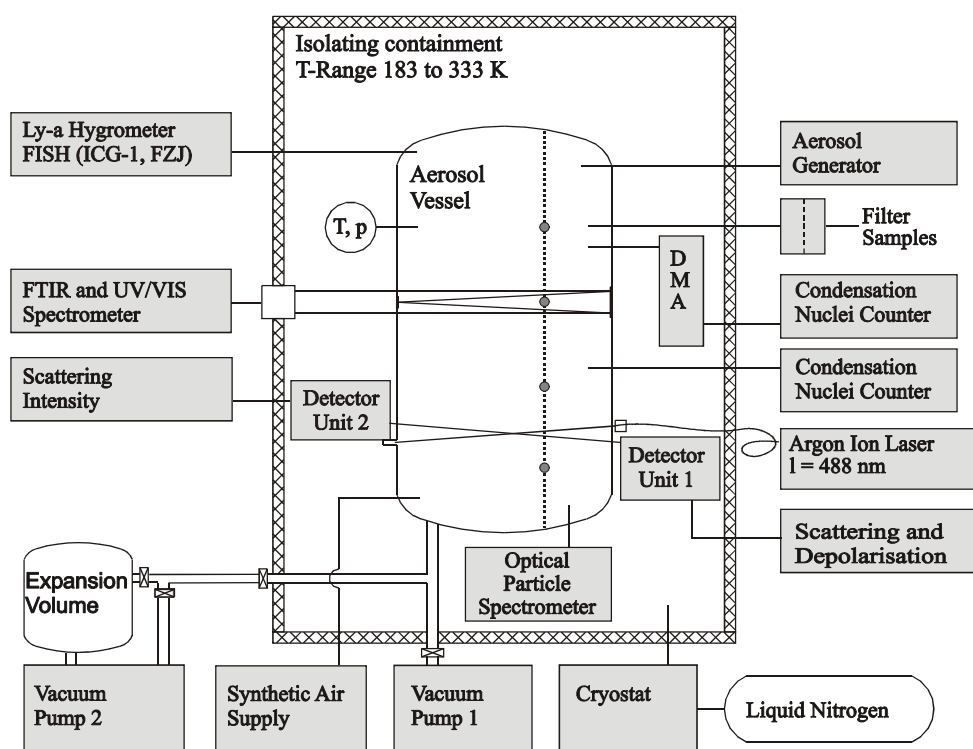
Figure 1. Schematic of the AIDA cloud chamber facility with instrumentation used for ice nucleation experiments.
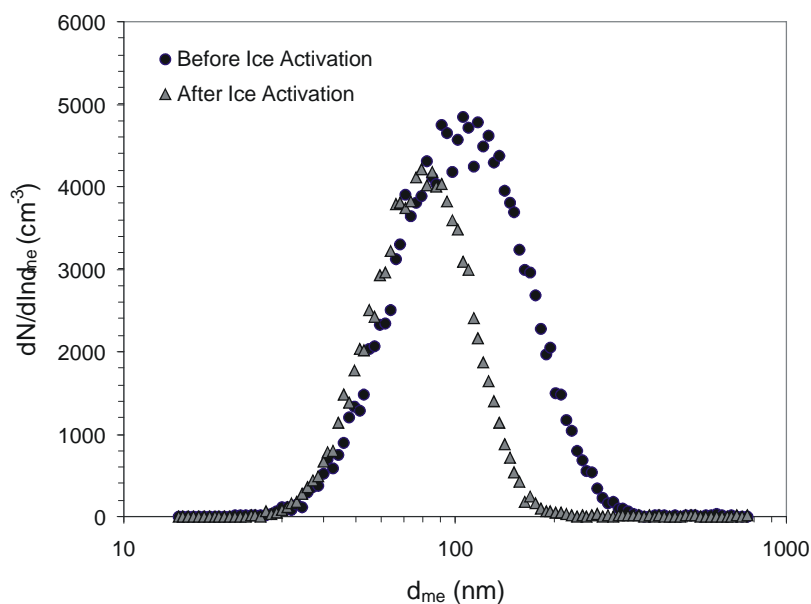
Figure 2. Size distribution of graphite sparc generator soot used for AIDA ice activation experiments. After ice activation the mobility equivalent particle diameters are smaller due to restructuring processes.

Before each set of up to 5 subsequent expansion cycles at the same temperature but different pumping speeds and cooling rates, the aerosol vessel was pumped off to below 1 hPa and refilled with particle free synthetic air to atmospheric pressure. Soot aerosol from a graphite sparc generator was added to the aerosol chamber with number concentrations between about 1000 and 3000 cm^{-3}. The soot agglomerates with mobility equivalent diameters between 30 and 300 nm (Fig. 2) are composed of primary particles with diameters between 4 and 8 nm. Ice activation caused the formation of more compact soot agglomerates which is indicated in Figure 2 by the smaller mobility equivalent diameters after ice activation. In this paper we show only ice activation results of first activations after soot aerosol formation.

Coating of soot particles with sulphuric acid was achieved in a temperature controlled flow tube system. Soot aerosol was mixed with synthetic air saturated with sulphuric acid vapour at a temperature between about 150°C and 200°C. Flow rates and cooling profile in the flow tube where adjusted in order to condense sulphuric acid vapour on the soot particles and to avoid nucleation of pure sulphuric acid droplets. The coated particles where then added to the aerosol chamber. In some experiments, the sulphuric acid coating was, after first ice activations, transferred into an ammonium sulphate coating by adding ammonia to the aerosol chamber. Therefore, the influence of both sulphuric acid and ammonium sulphate coating on the ice forming potential was investigated for the same soot aerosol.

Pristine ice crystals nucleated inside the aerosol chamber immediately after exceeding the critical ice supersaturation S_{IN} are sensitively detected by the depolarisation increase of back-scattered laser radiation at 488 nm. The growth of nucleated ice crystals was also detected with an optical particle counter located below the chamber and by FTIR extinction spectra measured in situ using a multi-path optical cell (see Fig. 1).

3 RESULTS

The heterogeneous IN on graphite sparc generator soot aerosol was investigated at temperatures between 184 and 240 K (Fig. 3). The critical ice saturation ratio S_{IN} at freezing onset was measured as described above. At temperatures above 235 K, ice nucleation on pure soot particles only occured close to or slightly above water saturation (dashed line in Figure 3). Liquid water seems to condense on the soot particles before ice forms (condensation freezing).
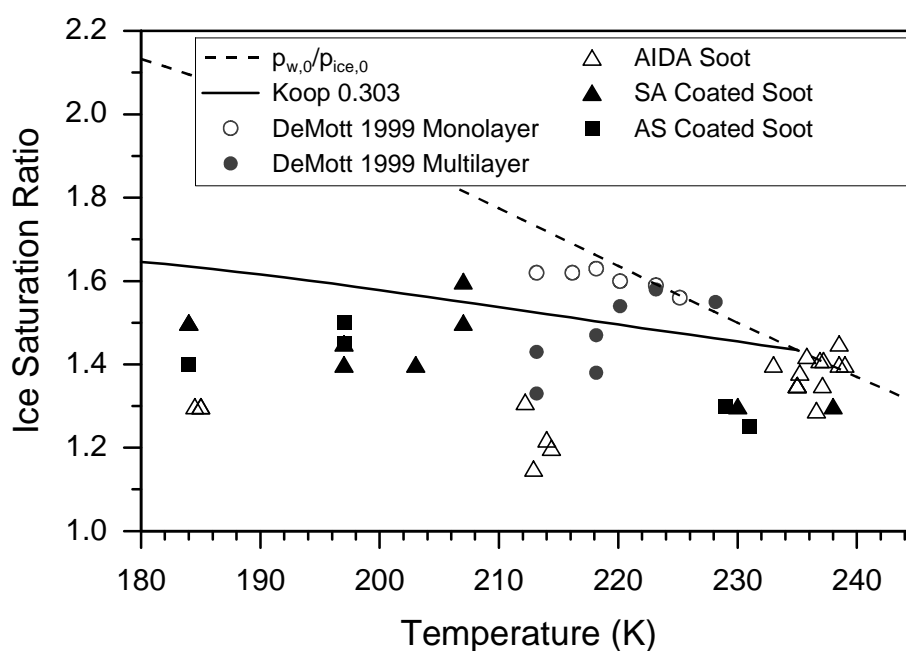

Figure 3. Ice saturation ratios measured for ice nucleation on pure soot and soot coated with sulphuric acid (SA) and ammonium sulphate (AS). The AIDA data is compared to results of DeMoot et al. (1999).

At lower temperatures, ice is formed significantly below the liquid water saturation threshold and also below the threshold for homogeneous freezing nucleation of supercooled liquid solution droplets indicated by the solid line (Koop et al., 2000). Decreasing S_{IN} with decreasing temperatures was also found by DeMott et al. (1999) who measured IN on redispersed Degussa soot at temperatures between 213 and 233 K. In that study, significant decrease of S_{IN} below the values of homogeneous IN was only measured for soot with 'multilayer' sulphuric acid coating. At 213 K, S_{IN} measured for multi-layer sulphuric acid coated Degussa soot by DeMott et al. (1999) agrees with the AIDA data measured for untreated sparc generator soot. The first AIDA measurements below 213 K indicate a slight increase of S_{IN}. This trend has to be confirmed by further data currently analysed.

Coating of soot particles with significant amount of sulphuric acid (up to some ten percent by particle mass) increases the freezing relative humidity by about 10 to 20 % at temperatures below 220 K. This is in contrast to the results by DeMott et al. (1999) who found decreasing freezing relative humidity with increasing amount of sulphuric acid coating. Neutralisation of the sulphuric acid coating to ammonium sulphate in some AIDA experiments did not significantly change the onset of ice nucleation.

4 SUMMARY AND CONCLUSION

In the AIDA experimental facility, the freezing relative humidity was measured for pure graphite sparc generator soot and soot coated with sulphuric acid and ammonium sulphate. At temperatures above 235 K, IN on untreated soot seems to occur only after liquid activation of the soot particles, whereas at lower temperatures deposition freezing was measured at ice saturation ratios between 1.2 and 1.3 which is significantly below water saturation and below the critical ice saturation for homogeneous IN of solution droplets. Coating of soot particles with sulphuric acid and ammonium sulphate increases the freezing relative humidity by about 10 to 20 % at temperatures below 220 K. In further experiments the effect of organic carbon content on the IN of soot particles will also be investigated.

REFERENCES

DeMott, P. J., Y. Chen, S. M. Kreidenweis, D. C. Rogers, and D. E. Sherman, 1999: Ice formation by black carbon particles. *Geophys. Res. Lett.* 26, 2429-2432.

Gierens, K., U. Schumann, M. Helten, H. Smit, and P. H. Wang, 2000: Ice supersaturated regions and subvisible cirrus in the northern midlatitude upper troposphere. *J. Geophys. Res.* 105, 22743-22753.

Haag, W., B. Kärcher, S. Schaefers, O. Stetzer, O. Möhler, U. Schurath, M. Krämer, and C. Schiller, 2003: Numerical simulations of homogeneous freezing processes in the aerosol chamber AIDA. *Atmos. Chem. Phys.*, 3, 195-210.

Jensen, E. J., O. B. Toon, S. A. Vay, J. Ovarlez, R. May, T. P. Bui, C. H. Twohy, B. W. Gandrud, R. F. Pueschel, and U. Schumann, 2001: Prevalence of ice supersaturated regions in the upper troposphere: Implications for optically thin ice cloud formation. *J. Geophys. Res.* 106, 17253-17266.

Koop, T., B. P. Luo, A. Tsias, and T. Peter, 2000: Water activity as the determinant for homogeneous ice nucleation in aqueous solutions. *Nature* 406, 611-614.

Möhler, O., O. Stetzer, S. Schaefers, C. Linke, M. Schnaiter, R. Tiede, H. Saathoff, M. Krämer, A. Mangold, P. Budz, P. Zink, J. Schreiner, K. Mauersberger, W. Haag, B. Kärcher, and U. Schurath, 2003: Experimental investigation of homogeneous freezing of sulphuric acid particles in the aerosol chamber AIDA. *Atmos. Chem. Phys.*, 3, 211-223.

Zöger, M., A. Afchine, N. Eicke, M.-T. Gerhards, E. Klein, D. S. McKenna, U. Mörschel, U. Schmidt, V. Tan, F. Tuitjer, T. Woyke, and C. Schiller, 1999: Fast in situ stratospheric hygrometers: A new family of balloon-borne and airborne Lyman ? photofragment fluorescence hygrometers. *J. Geophys. Res.* 104, 1807-1816.

Detailed Modelling of Cirrus Clouds – an intercomparison of different approaches for nucleation

M. Monier[*], W. Wobrock and A. Flossmann
Laboratoire de Météorologie - Physique, CNRS / OPGC, Université Blaise Pascal, Clermont-Ferrand, France

Keywords: cirrus microphysics, homogeneous and heterogeneous nucleation, residual aerosol particles

ABSTRACT: An explicit treatment of ice microphysics is presented to describe the formation and evolution of cirrus clouds and their interaction with interstitial aerosol particles and droplets. Three different mechanisms for homogeneous and heterogeneous nucleation, respectively, will be used to study the influence of the nucleation rate on ice crystal formation. The results will be compared with those of other detailed models given in literature. In addition the modelled residual particle distributions of the ice crystals were calculated and compared to the CVI measurements performed during INCA. This comparison shows that most of the actually used nucleation schemes cannot reproduce reasonably well the observed residual particle spectra found in cirrus clouds during INCA.

1 INTRODUCTION

In order to improve the treatment of the ice forming processes in cirrus models numerous schemes for nucleation of ice crystals were developed, mainly based on the results of laboratory and field experiments. Most parameterisations assume a homogeneous nucleation process of solution droplets of nitric or sulphuric acid which give reasonable crystal concentrations for temperatures below −40°C. Measurements in cirrus clouds during the flight campaign INCA (Ström et al., 2002) however document that significant numbers of ice crystals also occurs for temperatures strongly above −40°C. Thus an important question to answer is: which mechanism - homogeneous or heterogeneous nucleation – dominates the ice crystal formation. Three parameterisations for homogeneous and heterogeneous nucleation resp. are used in the dynamical frame of an air parcel model. The model results are compared with those of Lin et al. (2002) and with the residual particle spectra observed during INCA.

2 MODELLING OF MICROPHYSICAL PROCESSES

Aerosol particles grow by water vapour diffusion to solution droplets or further to cloud drops and thus serve as cloud condensation nuclei. At low temperatures and under ice supersaturated conditions aerosol particles can also be ice nuclei and thus form ice crystals. In order to consider all these components in a cloudy atmosphere we make use of two number distributions: one for solution droplets or liquid cloud droplets and another for the ice crystals.

The number distribution of droplets f_{wat} $(m, m_{AP,N}, x_i)$ is treated as a function of the total particle mass m, the dry aerosol mass $m_{AP,N}$, and the chemical composition x_i of the aerosol particle. In this study we follow only one type of aerosol particles and do not consider an external mixture. If $m \gg m_{AP,N}$ drops are present while for solution droplets m and $m_{AP,N}$ differ only by a factor of 3 or less. For $m = m_{AP,N}$, f_{wat} represents the dry aerosol particle distribution (as provided by measurements with optical particle counters or differential mobility analysers).

The number distribution of ice crystals f_{ice} $(m, m_{AP,N}, x_i)$ is given by the same variables. However,

---

[*] *Corresponding author:* Marie Monier, Laboratoire de Météorologie-Physique, 24 ave. des Landais, F-63177 Aubière Cedex, France. Email: monier@opgc.univ-bpclermont.fr

m represents the mass of the "solid" water. As above, only one species x_i of aerosol particles is treated for this study.

Both number distributions f_{wat} and f_{ice} are calculated by numerical integration of equations (1) and (2). The first term on the right hand side of eq.(1) describes the time evolution of f_{wat} by condensational or evaporational growth. As the growth of dry aerosol particles to wet particles or droplets is continuously described by the Köhler theory, no additional term for the nucleation of solution droplets occurs. The growth velocity $(dm/dt)_{wat}$ is used as given in Pruppacher and Klett (1997). For the description of cirrus clouds we have to consider the loss in wet aerosol particles due to their *nucleation* as crystals as well as their collision or riming on existing ice crystals.

Consequently, these two processes appear in equation (2) as source terms. The depositional growth of the ice crystals with the growth velocity *dm/dt* is calculated as given in Pruppacher and Klett (1997). We notice that the key parameter controlling $(dm/dt)_{ice}$ is the ice supersaturation.

$$\frac{\partial f_{wat}(m, m_{AP,N}, x_i)}{\partial t} = -\frac{\partial}{\partial m}\left[f_{wat}(m, m_{AP,N}, x_i)\frac{dm}{dt}\bigg|_{wat} \right] \qquad \text{condensation / evaporation}$$

$$- f_{wat}(m, m_{AP,N}, x_i)\ J_{\text{hom/het}} \qquad \text{loss by ice nucleation} \qquad (1)$$

$$- \int_{m_{0crys}}^{\infty} f_{wat}\ K(m_{crys}, m_{drop})\ f_{ice}\ dm_{crys} \qquad \text{loss due to riming}$$

$$\frac{\partial f_{ice}(m, m_{AP,N}, x_i)}{\partial t} = -\frac{\partial}{\partial m}\left[f_{ice}(m, m_{AP,N}, x_i)\frac{dm}{dt}\bigg|_{ice} \right] \qquad \text{diffusional growth}$$

$$+ f_{wat}(m, m_{AP,N}, x_i)\ J_{\text{hom/het}} \qquad \text{hom. and het. nucleation} \qquad (2)$$

$$- \int_{m_{0drop}}^{\infty} f_{wat}\ K(m, m_{drop})\ f_{ice}\ dm \qquad \text{riming}$$

$$+ \int_{m_{0drop}}^{\infty} \left(\int_{m_{0crys}}^{m_{crys}} f_{wat}\ K(m_{crys}^*, m_{drop})\ f_{ice}\ dm_{crys}^* \right) dm_{drop}$$

For the riming of wet aerosol particles with ice crystals we use the collection kernel *K* given by Martin et al. (1980) et Wang and Wusheng (2000). The different nucleation rates *J* used in this study for homogeneous nucleation J_{hom} and for heterogeneous nucleation J_{het} will be presented in the following chapter.

3 HOMOGENEOUS AND HETEROGENEOUS NUCLEATION

3.1 *Homogeneous nucleation*

Three different methods for the calculation of the nucleation rate J_{hom} will be compared: These are given by Tabazadeh et al. (2000), DeMott et al. (1997) and Koop et al. (2000).

The classical approach of Tabazadeh et al. is based on the results of laboratory studies for surface tension, density, and activation energy for a solution of sulphuric acid. These values are fitted as a function of temperature and weight percentage *w*. As our model concept with $f_{wat}(m, m_{AP}, x_i)$ directly provides $w\ (= m_{AP}/m)$ a further fit for *w* as used in the work Tabazadeh et al. (2000) is not needed.

The method of DeMott et al. follows the classical approach for homogeneous nucleation of pure water (Pruppacher and Klett, 1997). Herein the effect of the solution is considered by the use of a so called effective temperature, which corrects the droplet temperature by the freezing point depression.

Koop et al. (2000) found by laboratory studies that the homogeneous nucleation rate is independent of the solute nature of the aerosol and only depends on water activity. Thus, the key parameters for this approach of the nucleation rate are temperature and humidity.

3.2 *Heterogeneous nucleation*

For the heterogeneous nucleation we use the empirical approaches of Meyers et al. (1992) and DeMott et al.(1997) and DeMott et al.(1998) which are based on field or laboratory experiments.

$$N_{IN} = F \times 10^{-3} \times \exp(\text{-}0.639 + 12.96 \times S_{v,ice}) \tag{3}$$

The parameterisation of Meyers et al. (eq. 3) only needs the knowledge of the ice supersaturation $S_{v,ice}$. F represents a positive value ≤ 1, which allows to reduce the number of ice crystal nucleated due to the environmental conditions.

$$N_{IN} = 1.04 \times 10^{-4} \times 4\pi r^2{}_{soot} \times (T_0\text{-}T_{eff})^{7.767} \tag{4}$$

The approach of DeMott et al. (1997), similar to their approach for homogeneous nucleation, works with the effective temperature. In addition, this parameterisation (eq. 4) takes the surface of the insoluble soot particles into account, implying that the nucleation rate of insoluble particles increases with size (T_0 = triple point of water).

$$N_{IN} = N_{CN} \times 1.3 \times 10^{-23} \times (T_0\text{-}T_{eff})^{11.75} \tag{5}$$

The third approach for heterogeneous nucleation of DeMott et al.(1998) is mainly based on aircraft observations in cirrus clouds. In this experiment DeMott et al. found a strong correlation between the number of cloud nuclei (N_{CN}) and ice nuclei (N_{IN}). This parameterisation for ice nuclei (eq. 5) also takes the effective temperature into account.

4 RESULTS FROM AIR PARCEL MODELLING

Analogously to the recent comparative study of Lin et al. (2002) on detailed cirrus models we performed the following calculation in the dynamical frame of an air parcel model moving wet adiabatically upwards in an ice supersaturated atmosphere. Two scenarios are investigated: a cold air case, where the air parcel starts at 170 hPa, $T = \text{--}60°C$ and Rhi = 100 %, and a warm case starting at 340 hPa, $T = \text{-}40°C$ and Rhi =100 %. The aerosol particles distribution was supposed to consist in a single mode log normal distribution with a total number of N= 200 cm^{-3}, a mean radius r_{MEAN} = 20 nm, and a standard deviation σ = 2.3. More details on the dynamical and microphysical model setup are given in Lin et al. (2002).

4.1 *Air parcel results for homogeneous nucleation*

Figure 1 presents the results for the modelled ice number concentration after a vertical ascent of 800 m. The results for the cold case are displayed on the left hand side, the warm case is displayed on the right. Each case was run for a vertical wind speed of 4, 20, and 100 cm/s. For each case and each updraft speed three different rates for homogeneous nucleation (see section 3.1) were compared. The letter T on the abscissa of Figure 1 stands for the approach of Tabazadeh et al. (2000), K for the parameterisation of Koop et al. (2000), and D for DeMott et al. (1998).

The elevated bar for each case and each updraft velocity gives the range of the results found in Lin et al. (2002) for the same parcel studies. These authors compared 7 different detailed numerical cirrus models, which essentially used the same three parameterisations for homogeneous nucleation which we abbreviated by T, K, and D.

Figure 1 displays that the number of ice crystals formed increases significantly with the intensity of the vertical wind. The reason for this behaviour results from the increase of the ice supersaturation with increasing vertical wind speed (see Tab. 1). However the influence of the air temperature on ice crystal production is less pronounced. In our study a number increase for the cold case only becomes visible for the highest updraft speed of 1 m/s. In Lin et al. on the other side an increase in ice crystal number at colder temperatures becomes obvious for the lower updraft velocities of 4 and 20 cm/s.
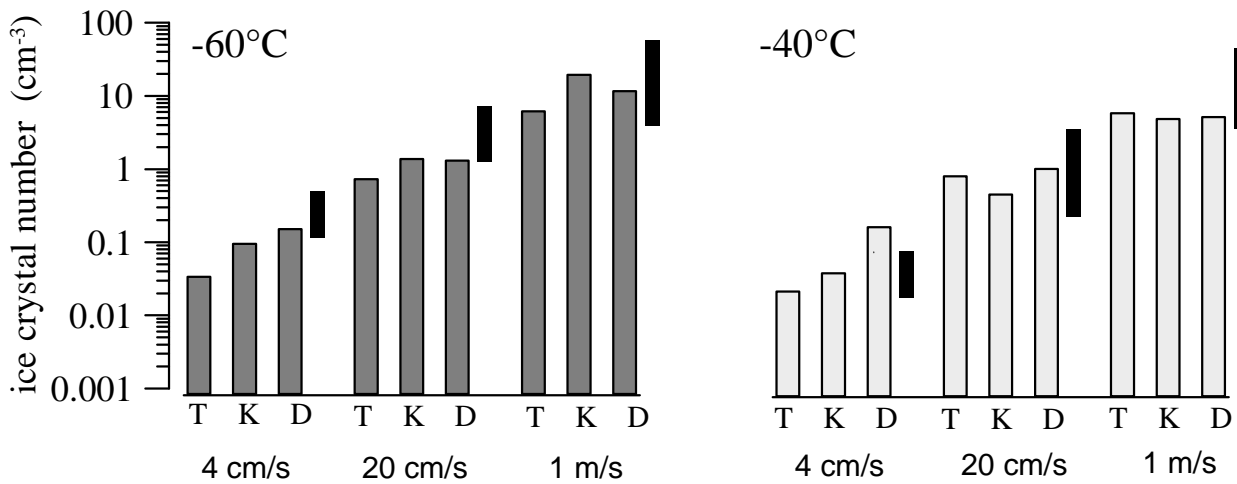
Figure 1. Total number of ice crystals formed by homogeneous nucleation using different vertical updraft velocities *w* and different nucleation rates T, K, or D. The elevated bars represent the range of results found in Lin et al. (2002) for the same scenarios.

Table 1. Maximum ice supersaturation (%) calculated for different schemes of homogeneous nucleation.

nucleation scheme	cold case			warm case		
	4 cm/s	20 cm/s	100 cm/s	4 cm/s	20 cm/s	100 cm/s
T	43.4	52.8	67.2	41.6	44.5	46.2
K	45.9	47.4	49.0	41.5	42.6	43.9
D	48.7	49.6	51.9	42.1	42.9	44.9

The difference in number concentration between the three nucleation rates T, K, and D for cases with $w \geq 20$ cm/s in Figure 1 is significantly weaker than in the study of Lin et al. This is not surprisingly as we used one numerical cloud model wherein only the rate of nucleation varied, while Lin et al. (2002) compared the results of seven different numerical cloud models in which each of them treated one (of the three) nucleation rates individually.

For the two cases with low vertical winds of 4 cm/s our range of variability in ice number concentration modelled is the same as in Lin et al. We can see from these cases with low updrafts that it is the parameterization T which always gives the lowest ice crystal numbers. The same statement holds for all updraft conditions in the cold case below –60 °C.

In order to understand the behaviour of the different nucleation rates we displayed in Figure 2 the homogeneous nucleation rate J as a function of the ice supersaturation for a small (radius = 40 nm) and a medium size aerosol particle (200 nm). We can detect from Figure 2 that larger solution droplets start to nucleate at lower supersaturations than the smaller ones. This behaviour is most pronounced for the nucleation scheme T, and less pronounced for the scheme K. In addition, Fig. 2 indicates that the important nucleation rates occur for low temperatures by an increase of the supersaturation. This is especially the case for scheme T, where ice nucleation for the small particles at −65 °C does not start until the relative humidity exceeds 167 %, while for the warm case at -45 °C this occurs already at 147 %. Considering also the maximum supersaturation values given in Tab.1 that occur during the ascent of the air parcel it becomes obvious that for the cold case scheme T will not be able to nucleate small aerosol particles. Consequently the crystal numbers of scheme T in the cold cases are smaller than those of scheme K and D (Fig. 1).
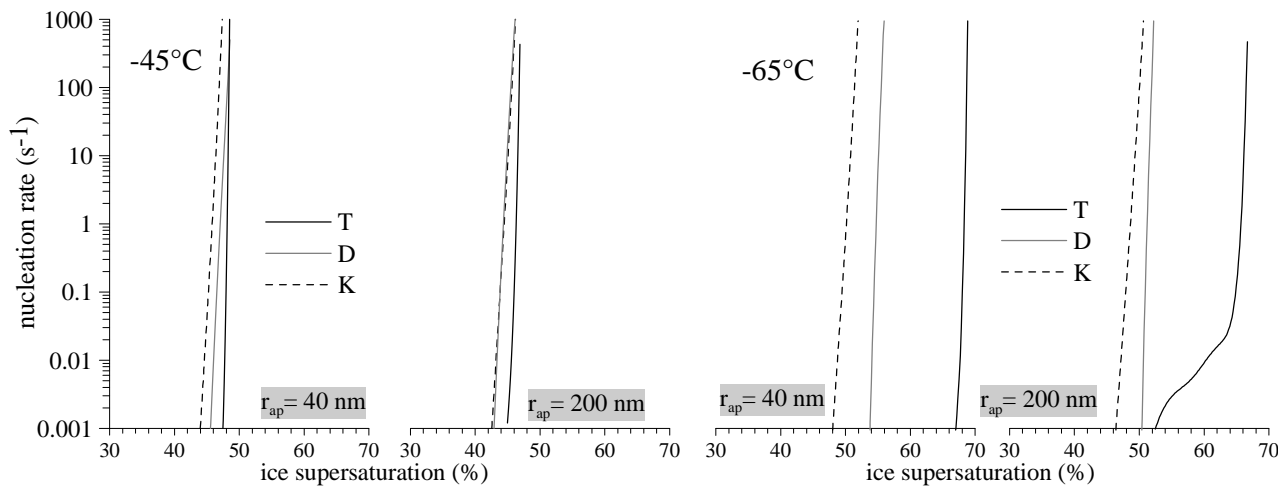
Figure 2. Homogeneous nucleation rate J (number/s) as a function of ice supersaturation for two different aerosol particle sizes and the three nucleation schemes T, K, and D.
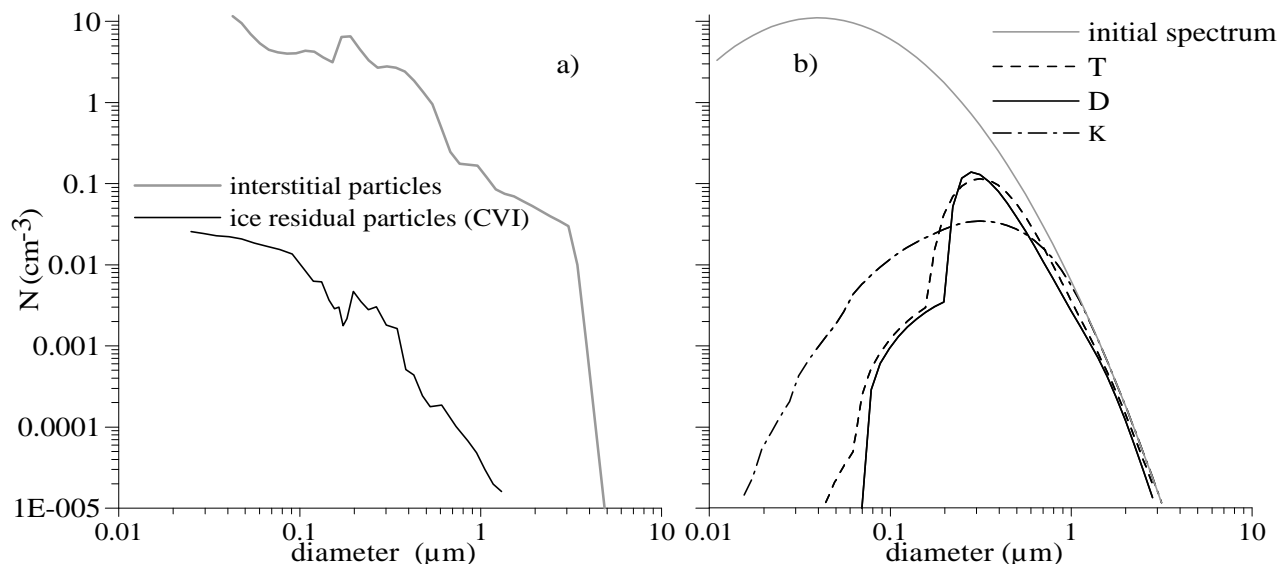

Figure 3. Comparison between interstitial and residual spectra. a) Measurements performed during INCA, on 30 mars 2000 east of Punta Arenas, b) modelling results for the homogeneous nucleation rates T, K, and D.

This behaviour of scheme T disappears for the warm cases with 20 and 100 cm/s. The differences between nucleation rates T and K or D displayed in Figure 2 at -45 °C are significantly smaller than for the cold case and thus the number concentrations of scheme T are in the same range as for K and D. Only for the warm case with 4 cm/s the values of T in Figure 1 remain again weaker than those of K and D. The lower maximum supersaturation of 41.6 % (Tab.1) in this case allows only the nucleation of a few large aerosol particles for scheme T while schemes K and D can activate significantly more particles around 41 % supersaturation (see warm case in Fig.2).

4.2 *Comparison with the cloud residual particle spectra*

Another helpful method for the assessment of the different parameterisations for homogeneous nucleation is the analysis of the particle residuals stemming from cirrus ice crystal spectra. This kind of measurements was performed by Ström et al. (2002) during the European cirrus campaign INCA (www.pa.op.dlr.de/inca/). Figure 3a shows observational results of 30 March 2000 of residual and interstitial particle spectra. Similar results were found for the northern hemisphere, indicating that only around 0.1 to 1% of the present aerosol particles nucleate and form ice crystals.

The modelling concept for ice crystals presented by eq. 2 treats explicitly the nucleus mass $m_{AP,N}$ and therefore allows the calculation of the residual particle spectra. Results for the three different schemes for homogeneous nucleation T, K, and D are displayed for the warm case with w = 20 cm/s in Figure 3b.

   The graph of the three residual spectra reflects the nucleation behaviour discussed already in Figure 2: large particles will nucleate at lower supersaturation than small particles, thus, most large particles serve as ice nuclei while the small ones nucleate only slightly or not at all. The comparison with the measurements (Fig. 3a) suggests that all three nucleation schemes strongly overestimate the nucleation of large aerosol particles while the nucleation of the small ones is almost completely absent. A possible explanation for the discrepancy with the observation could be that not homogeneous but heterogeneous nucleation dominates in the atmosphere of INCA.

4.3 *Heterogeneous nucleation*

In order to see how heterogeneous nucleation influences the modelled residual aerosol spectra we perform the same calculation as in section 4.2 (warm case, w = 20 cm/s), however using the heterogeneous nucleation rates given in section 3.2. The results are displayed in Figure 4. The preference to nucleate large particle remains only visible for the approach of DeMott et al. (1997), named D'97. The parameterisation of Meyers et al (1992), named MEY, nucleates all particle size with the same efficiency as the nucleation rate (eq. 5) only depends on the ice supersaturation. A size dependency for the heterogeneous nucleation rate of DeMott et al. (1998), named D'98, also exists in eq. 4 (hidden in T_{eff}), but this cannot be well detected in Figure 4a due the low nucleation efficiency. The strength of nucleation rate D'98 is determined by two coefficients which were determined by only one flight in cirrus clouds.
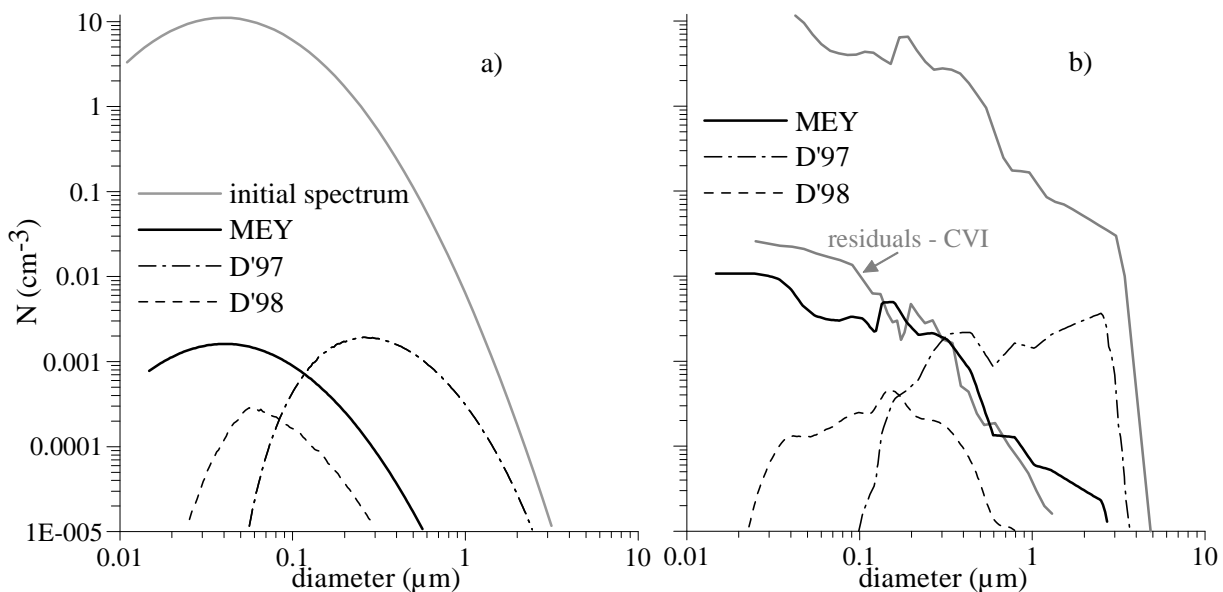

Figure 4. Modelling results for number distribution of residual particles using the heterogeneous nucleation rates MEY, D'97, and D'98 . In a) a log normal distribution is used for the ambient aerosol particle spectra, in part b) the interstitial spectrum measured on 30 March 2000 during INCA (cp. Fig. 3).

The maximum supersaturation values obtained during the ascent of the air parcel using these heterogeneous nucleation rates differ clearly from those for homogeneous nucleation given in Table 1. While D'98 still reaches 44.6 % supersaturation, the maximum values of D'97 only gives 27.8 % and MEY just 15.3 %. Running homogeneous and heterogeneous nucleation both together in the air parcel Figure 4a will not change for the schemes MEY and D'97 as the high values of supersaturation needed for the homogeneous nucleation cannot be reached. In a combination of D'98 with one of the homogeneous schemes T, D, or K, however, both rates for nucleation become visible through two maxima in the residual spectra of Figure 4a (not displayed).

Similar to the above performed air parcel simulation for w = 20 cm/s and $T = -40$ °C we run the same three schemes for heterogeneous nucleation but with the observed aerosol spectrum given in Fig. 3a. The results are presented in Figure 4b. The behaviour of the different heterogeneous nucleation rates stay the same as already discussed in Figure 4a. It is surprising that the approach of Meyers et al. (1992) agrees best the observed crystal residual aerosol spectra. For the crystal number controlling factor F in equation 5 we have taken the value 1.

5 CONCLUSION

From the modelling results we can conclude that the ice crystal number depends in the first place on the strength of the vertical velocity, as this one determines the value of maximum supersaturation which can be reached. A clear importance of the temperature on the crystal number nucleation becomes less visible from the different case studies.

For mean and high updraft velocities the employed parameterisations for homogeneous nucleation typically differ by a factor of 2. For low velocities however the discrepancy between the results can increase to a factor of 5 and more. These differences result from the size dependency of the nucleation rates which vary significantly between the schemes T, K and D.

A comparison of the homogeneous nucleation model results for the ice crystal residual particles with those measured during the INCA experiment in cirrus clouds points out a dramatic discrepancy in the shape of the size dependency. Observations in cirrus clouds for the northern and southern hemisphere do not confirm a stronger nucleation efficiency for the larger aerosol particles but show rather a size independent nucleation efficiency.

Similar to the homogeneous nucleation the parameterisations for heterogeneous nucleation D'97 and D'98 deviate also from the observational results. This is due to the fact that these two approaches also consider a size dependency. Surprisingly the parameterisation of Meyers et al. (1992) which simply depends on the ambient ice supersaturation but does not consider the physico-chemical properties of the aerosol particles reproduces the observation reasonably well.

REFERENCES

DeMott, P., D. C. Rogers, and S. M. Kreidenweiss, 1997: The susceptibility of ice formation in upper tropospheric clouds to insoluble aerosol components, *J. Geo. Res. ,* 102, 19575-19584.

DeMott P.J., Y. Chen, C.H. Twohy, D. Baumgardner, A.J. Heymsfield, and K.R. Chan, 1998: The role of heterogeneous freezing nucleation in upper tropospheric clouds: inferences from SUCCESS. *Geophys. Res. Lett.* 25, 1387-1390.

Koop, T. H. P. Ng., B. Luo, A. Tsias, and T. Peter, 2000: Water activity as the determinant for homogeneous ice nucleation in aqueous solutions, *Nature,* 406, 611-614.

Lin, R.-F., D. O'C Starr, P. J. DeMott, R. Cotton, K. Sassen, E. Jensen, B. Kärcher, X. Liu: Cirrus parcel model comparison project, 2002 : Phase 1: The critical components to simulate cirrus initiation explicitly, *J. Atm. Sci.*, 59, 15, 2305-2329.

Martin J. J., P.K. Wang, H. R. Pruppacher: A theoritical determination with which Aerosols Particles are collected by simple Ice crystal Plates, 1980: *J. Atm. Sci.*, 37, 1628-1638

Meyers M. P., P. J. DeMott, and W. R. Cotton: New primary Ice Nucleation Parametrizations in an Explicit Cloud Model, 1992: *J. Appl. Met.,* 31, 708-721.

Pruppacher and Klett, : Microphysics of clouds and precipitation, 1997. Kluwer Academic Publisher. 2nd revised and enlarged edition. 954pp.

Ström, J., et al.,2002: Aerosol and cirrus measurements at midlatitudes on the Southern hemisphere: An overview based on the first INCA experiment, *Air Pollut. Rep. 74, Rep. EUR 19,428 EN,* European Commission, Brussels.

Tabazadeh, A., S. T. Martin, J. S. Lin, 2000: The effect of particle size and nitric acid uptake on the homogeneous freezing of aqueous sulfuric acid particles, *Geophys. Res. Let.,* 27, No.8, 1111-1114

Wang, P., J. Wusheng,: Collision efficiencies of Ice Crystals at Low Intermediate Reynolds Number Colliding with Supercooled Cloud Droplets, 2000: A Numerical Study, *J. Atmo. Sci.*, 57, 1001-1009.

Simulation of Contrail Coverage over the USA Missed During the Air Traffic Shutdown

Patrick Minnis[3], Louis Nguyen, Donald P. Garber,
Atmospheric Sciences, NASA Langley Research Center, Hampton, Virginia, USA

David P. Duda
Hampton University, Hampton, Virginia, USA

Rabindra Palikonda, David R. Doelling
AS&M, Inc., Hampton, Virginia, USA

ABSTRACT: Contrails were simulated for the northeastern USA during the first part of the air traffic shutdown following the 9-11 terrorist attacks. Analysis of military contrails observed during the shutdown provided a baseline set of contrail properties that were employed to tune a contrail prediction scheme using high-resolution numerical weather analyses and normal air traffic flight data. The simulation produced a large area of contrails that started developing around 1000 UTC, 12 September 2001 and peaked in areal coverage of more than 200,000 km^2 around 1800 UTC. The simulation results were used to alter existing infrared satellite images to visualize the area for air traffic conditions. Initial estimates of the contrail radiative forcing are biased low because of improper treatment of different contrails overlapping on the same satellite imager pixels. Improvements were suggested for a more accurate and complete simulation of the contrail properties.

1 INTRODUCTION

Following the tragic events of 11 September 2001, commercial and personal air traffic over the United States of America (USA) was halted for at least 36 hours with resumption of more normal flight activity by 15 September 2001. During the air traffic shutdown, the contrail coverage decreased dramatically. This lack of contrails over the USA was even noticed by astronauts. Analyses of weather data during the shutdown period indicate an anomaly in the diurnal range of surface air temperature that was attributed to the lack of contrails (Travis et al. 2003). Such an anomaly would result from the lack of radiative forcing by contrails and would indicate not only that contrails affect climate but they can also affect the daily weather. To determine if such an anomaly can be realistically attributed to the absence of normal air traffic, it is necessary to accurately estimate the radiative forcing that would have occurred if normal air traffic had occurred.

Normally, it is difficult to determine the radiative forcing by contrails because air traffic is relatively continuous throughout much of the day (Garber et al. 2003). New and old contrails overlap with each other and with natural cirrus clouds making it difficult to determine the evolution and dissipation of individual contrails and their radiative impacts. The air traffic shutdown was essentially complete by 1600 UTC, 11 September 2001. Thus, the air over the USA should have been free almost all cirrus clouds produced by commercial air traffic by ~ 0000 UTC 12 September. A few isolated contrails from military flights developed over the northeastern USA, an area normally criss-crossed by thousands of flights. By analyzing the evolution and decay of those contrails, Minnis et al. (2002) were able to relate the contrail formation to a specific relative humidity range and estimate the properties of the individual contrails during each hour of their lifetimes. Those initial analyses provide the basis for realistically simulating the effects of the missing air traffic. This paper continues that effort by simulating the contrails that would have

---
[3] *Corresponding author:* Patrick Minnis, MS 420, NASA Langley Research Center, Hampton, VA, USA 23681. Email: p.minnis@nasa.gov

developed during that fateful day and by providing preliminary estimates of their potential radiative impact.

2 DATA AND METHODOLOGY

The basic approach taken here is to use the satellite analyses of Minnis et al. (2002) to determine a relative humidity with respect to ice (RHI) for a given meteorological analysis that can serve as threshold for persistent contrail formation. Flight tracks from a normal air traffic day are then used to simulate the flights through the atmosphere as defined by the meteorological analysis. If the RHI at the location of the plane at a given instant exceeds the threshold RHI value (RHI_t) and the temperature is low enough according to the Appleman criteria, then a persistent contrail is defined for that location. Contrail processes such as spreading, advecting, and dissipating are simulated in a relatively crude fashion and their optical properties are estimated as functions of time. Each contrail is geo-located according to its width, length, and height. This information is then used to alter the satellite image for the given time and location. The original and altered infrared (IR, 10.8 µm) satellite images for each hour are then used to compute the contrail longwave radiative forcing (CLRF).

2.1 *Data*

Hourly data from the eighth Geostationary Operational Environmental Satellite (GOES-8) are used in the simulation. These were also used by Minnis et al. (2002) to analyze the isolated contrails. The GOES-8 4-km IR images from 12 September 2001 serve as the primary dataset, while 1-km IR and split window (12 µm) data from the *NOAA* Advanced Very High Resolution Radiometer (AVHRR) and *Terra* Moderate Resolution Spectroradiometer (MODIS) provide supplementary information.

The temperature (*T*) and humidity fields are specified using an early version of the NOAA Rapid Update Cycle (RUC) analysis that is based on a hybrid-isentropic model (Benjamin et al. 2003). The RUC reanalyses used here have a 25-hPa vertical resolution in the upper troposphere and a 4-km horizontal resolution, and are available at each hour. RHI is computed from the relative humidity with respect to liquid water derived by the model. The RUC RHI output is similar to the radiosonde profiles in the northeastern USA, but differ by as much as $\pm 20\%$ between 8 and 13 km. (Minnis et al. 2002). The RUC tends to smooth the vertical profiles, reducing the humidity at some locations and increasing it at others. The hourly temperatures, winds (*V*), and relative humidities were assigned to the satellite data taken closest in time.

It was assumed that the 12 September air traffic would have been identical to the traffic from the previous Thursday. Thus, the simulation uses linear flight tracks (Garber et al. 2003) from 5 September 2001 that were located within the domain bounded by 33°N, 52°N, 66°W, and 93°W. The position of the flight at a given time was associated with the values of *T*, RHI, and *V* of the nearest vertical level and the relevant 40-km RUC box.

2.2 *Simulation process*

To persist, contrails and cirrus require RHI $\geq$ 100%. Because of negative biases in the relative humidity measured at cold temperatures (Miloshevich et al. 1999), RHI infrequently exceeds 100% in the USA radiosonde record. Furthermore, the RUC model adjusts and smoothes the RHI field so that it differs from the radiosonde measurements. While the older version of the RUC used here (discontinued 18 April 2002) yields RHI > 100% more often than the radiosondes, it is still biased low. Thus, it is necessary to increase the RHI from radiosonde measurements for $T < 0°C$ or set an artificially low value of RHI_t.

The threshold was determined by comparing the RUC RHI fields to satellite images of contrail and cirrus distributions using the RUC level having the greatest RHI values in the 150-350 hPa range. Figure 1 shows an example of contrails forming in heavy air traffic over the northeastern USA during 18 November 2001. The leading line of contrails in the *Terra* MODIS 11-12 µm brightness temperature difference image is located in east central Pennsylvania and New York (Fig. 1a). Contrails and cirrus cover most of the image west of that line. Comparison of the 225-hPa RHI contours (Fig. 1b) with the contrails indicate that few contrails formed over areas with RHI < 80%. This value is slightly less than the 85% found by Duda et al. (2003) for a different day. Comparison

of the isolated contrails from 12 September yield a different threshold as expected since the RUC alters the humidity field from the measured values as noted earlier. Figure 2a shows a single, but broken linear contrail over Ohio and Pennsylvania at 1108 UTC, 12 September 2001. Cirrus clouds are evident in northern and southern Ohio as well as northeastern Pennsylvania. The contrail pressure was found to be closest to 225 hPa (Minnis et al. 2002). The corresponding RUC analysis (Fig. 2b) shows that the cirrus occurred for RHI > 80% while the contrail was persisting in air with RHI as low as 58%. Correction of the 1200-UTC local radiosonde data using the Miloshevich et al. (2001) formula indicate that the actual RHI in the domain is probably 30-40% greater than indicated by the RUC (Minnis et al. 2002). Thus, the actual RHI values could exceed 140% in portions (e.g., central Indiana) of domain and should be close to 110% in southeastern Pennsylvania. Comparisons of images and RUC analyses like those in Figure 2 for the remainder of the day led to the conclusion that $RHI_t = 70\%$ for 12 September.

Once formed, the contrails were allowed to spread based on wind shear. It was assumed that the contrails precipitated with a fall speed of 3 cm s^{-1}. This fall speed produced a spreading rate of 6 km h^{-1}, the same as that determined for the isolated military contrails. Although the isolated contrails spread to widths as large as 40 km, it was assumed that the maximum width would be 12 km because it corresponds to the length-weighted average width of the military contrails. No new nucleation was allowed so that the optical mass (*OM*) remained constant as the product of the optical depth (*OD*) and the width once the *OD* reached it peak according to the log-normal function,

$$OM = a \exp\{-0.5 \, [\, \ln(x / x_o) / b]^2\}, \tag{1}$$

where x is the mean contrail age, x_o is the time of peak *OM* (2.5 hours), a is peak contrail OM = 0.6, b is the width of the peak (0.5). This function mimics the average behavior of the isolated contrails in the same domain. The contrails are then advected each hour using the winds at the contrail altitude. In the new time step, the contrail is compared to the RHI at its new location. If RHI < 70% in the RUC box, the portion of the contrail within the box is deleted. It is also deleted if it is over 6 hours old to ensure that the average contrail lifetime is the same as that for the isolated contrails. The endpoints, width, and *OD* of each contrail are saved each hour.

The calculation of CLRF was accomplished in the following manner. The parameters for each contrail at a given hour were used to compute changes to the 4-km GOES-8 IR image by altering the brightness temperature T_{IR} of each pixel affected by the simulated contrail. Figure 3 shows a schematic drawing of four 4-km pixels divided into sixteen 1-km sub-pixels. The fractional contrail coverage in each 4-km pixel is simply the number of 1-km sub-pixels with centers between the lines defining the boundaries of the contrails based on the contrail endpoints and width. In Figure 3, pixel A has a fractional coverage $f_c = 9/16$ compared to 6/16 for pixel D. The contrail optical depth for overlapped sub-pixels is simply the sum of the optical depths for the overlapping contrails. In Figure 3, $OD(B) = [13*OD(2) + 8*OD(1)] / 15$, while $OD(C) = 14*OD(1) / 14$. This formulation yields a value that can exceed the pixel contrail optical depth because it includes only portions of the pixel that contain contrails. But it maintains the true OD of the contrails in the pixels. As seen in the schematic drawing, a contrail may be less than 4-km wide, but it can affect two 4-km pixels. To obtain the effective optical depth of the contrails in the pixels, the pixel OD is multiplied by f_c. In the current simulation, however, the OD for each overlap pixel was computed using only the value of OD corresponding to the last contrail that affected the pixel resulting in an underestimate of OD for the pixel. The new brightness temperature of a given contrail pixel is

$$TC_{IR} = B^{-1}\{[1 - \varepsilon(OD \, f_c)] \, B(T_{IR}) + \varepsilon(OD \, f_c) \, B(TC)\} \tag{2}$$

where the emissivity ε is computed using the formula of Minnis et al. (1993) for an axi-symmetrical hexagonal ice column with a length of 20 μm, B is the 10.8-μm Planck function, and *TC* is the contrail temperature. For this simulation *TC* is the temperature at 225 hPa. The longwave (5 - 100 μm) fluxes with (M_{LW}) and without (MC_{LW}) contrails is computed as in Minnis and Smith (1998) using a new set of coefficients based on broadband data from the Clouds and Earth's Radiant Energy System scanners. The narrowband IR fluxes (M_{IR}) were computed from the GOES-8 IR brightness temperatures as in Minnis and Smith (1998). The new formula,

$$M_{LW} = 69.56 + 5.516 \, M_{IR} - 0.0186 \, M_{IR}^2 + -0.123 \, M_{IR} \ln(h) \tag{3}$$

where h is the average column-weighted relative humidity (in percent) above the altitude corresponding to T_{IR} in the RUC profile up to 300 hPa. MC_{LW} is also computed from (3) using the contrail flux, MC_{IR}. The contrail radiative forcing is $CLRF = M_{LW} - MC_{LW}$, where the fluxes represent a single pixel or an average of many pixels over a given area.

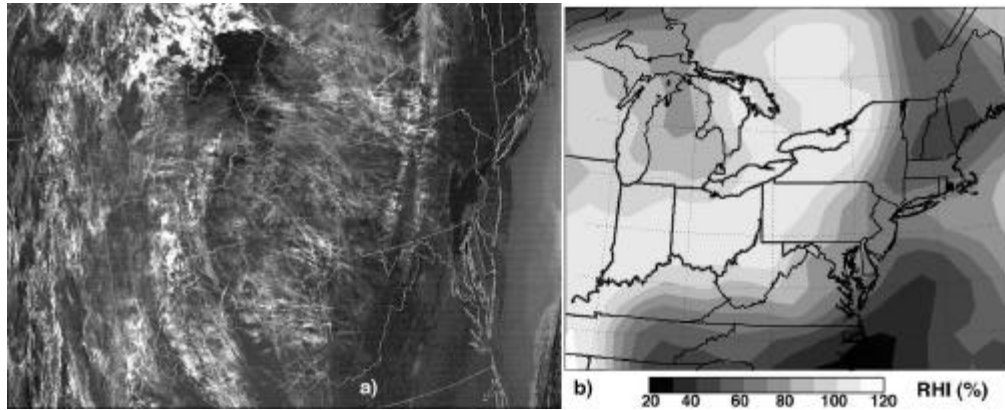The simulation process was performed using all GOES-8 pixels in the domain for each hour between 0945 and 2045 UTC.

Figure 1. Contrails and humidity over northeastern USA, 18 November 2001. (a) Terra MODIS T11-T12 image, 1624 UTC. (b) 225-hPa RHI (%) from RUC reanalysis, 1600 UTC.
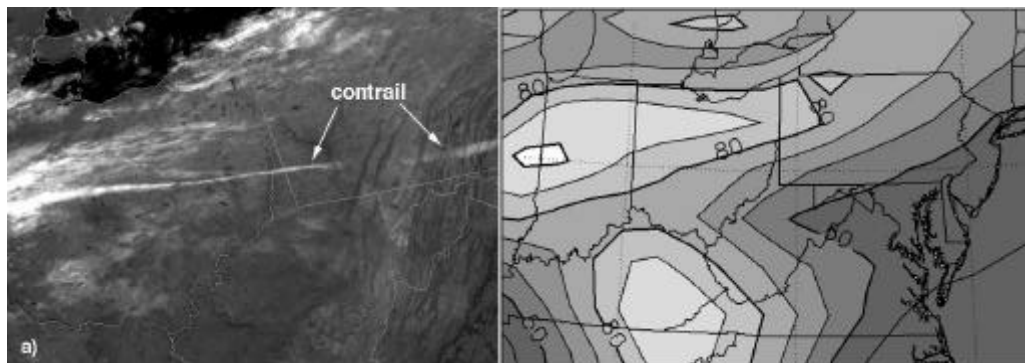
Figure 2. Extended contrail and humidity over northeastern USA, 12 September 2001. (a) NOAA-14 IR image, 1108 UTC. (b) RUC RHI (%) at 225 hPa, 1100 UTC; RHI < 50% in darkest areas.
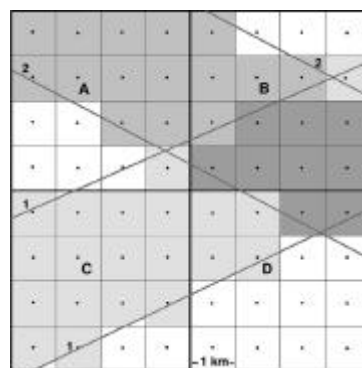
Figure 3. Schematic of method for altering 4-km GOES IR pixels (A - D). Boundaries of contrails 1 and 2 are denoted by the numbered gray lines. 1-km sub-pixels filled by light gray (contrail 1), medium gray (contrail 2), dark gray (overlap).

3 RESULTS & DISCUSSION

Figure 4 shows examples of the original GOES-8 IR images, the contrail masks, and the GOES-IR images containing the simulated contrails for 1045, 1345, 1645, and 1945 UTC. The southern extent of the domain is best represented by the simulated image, but the northern portion is cut off. At 1045 UTC (Fig. 4a), the air traffic for the normal day has just begun over the eastern North America resulting in the generation of a few contrails over South Carolina, western Pennsylvania, and southern Canada. The Canadian contrails are primarily imbedded in extant cirrus and would not be detectable and are cut off in the image. The simulated contrails in northwestern Pennsylvania are similar in appearance to the existing military contrail in southwestern Pennsylvania (Fig. 2 and Fig. 4a3). By 1345 UTC (Fig. 4b), the air traffic is well underway and the contrail coverage is rapidly increasing. The new simulated contrails continue to appear realistic compared to their real counterparts. For example, three military contrails cross West Virginia in an east-west direction while the simulated contrails are oriented north-south. Another east-west contrail in northern Virginia appears to be a continuation of the military contrail in West Virginia. A pronounced mass of overlapping contrails is evident over New Jersey. By 1645 UTC (Fig. 4c), that same mass has moved off the coast and thinned out somewhat (Fig. 4c3). Many new contrails formed while others dissipated. At 1945 UTC (Fig. 4d), many of the contrails have dissipated although the cirrus deck in western Pennsylvania and eastern Ohio has been enhanced considerably by the relatively old contrails that formed in that area. The few spreading contrails over New England appear less realistic than the younger ones, probably as a result of the uniform spreading process used in the simulation. Nevertheless, the resulting imagery, is relatively realistic overall in terms of appearance and compared to the actual contrails that were present.

The total contrail coverage and CLRF for the domain are plotted in Figure 5. The contrail coverage is based on the sum of f_c for the domain divided by total number of pixels, 307,200. The CLRF, however, is based on TC_{IR}, which was computed using the OD for only one of the contrails in the overlapped cases and not the sum of the two. The resulting value is, therefore, an underestimate of the CLRF. Contrail coverage (Fig. 5a) peaked at 1745 UTC with a value of 3.66% or slightly more than 200,000 km². This result is comparable to the average global linear contrail coverage estimated to be between 200,000 and 400,000 km². The total area covered by individual contrails (counting overlapped sub-pixels more than once) peaked at 1745 UTC with 8.85%, 2.4 times more than the actual number of pixels that would be identified as contrail pixels. Thus, overlapped pixels play a critical role in the climatic impact of contrails and need to be treated carefully. Because the mean OD was computed only for the individual contrails, it is underestimated. It peaked at a value of 0.257 at 1245 UTC and slowly dropped to 0.138 by 1945 UTC. The ODs should be roughly 2.5 times the values found here because of the impact of contrail overlap.

The unit CLRF (Fig. 5b) rises from a negligible value at 0945 UTC to a relatively broad maximum of ~6 Wm⁻² between 1245 and 1545 UTC. This maximum and the gradual decrease is mostly governed by the variation in OD. The total CLRF (contrail forcing relative to the entire domain) is dominated by the contrail coverage and rises to a maximum of 0.25 Wm⁻² between 1745 and 1845 UTC. The unit CLRF values are 2 - 4 times less than those found by Palikonda et al. (2003) from satellite observations of actual contrails. Some of the difference is due to the co-occurrence of the contrails with cirrus clouds, but the great portion of the difference is most likely due to the underestimate of contrail OD for the overlapped pixels. If the ODs were increased by 250%, then the unit CLRF would peak at 15.2 Wm⁻², a value closer to the daytime September 2001 mean for the linear contrails as derived from AVHRR data (Palikonda et al. 2003). Similarly, the maximum CLRF would be around 0.63 Wm⁻². Thus, more realistic values for the simulation can be obtained by multiplying those in Figure 5b by 2.5.

The simulation presented here represents the first step in theoretically evaluating the possible impact of contrails on the daily surface temperature and for explicitly representing contrails in mesoscale weather predictions. A number of improvements and additions are needed to complete the simulation. These include the proper assignment of optical depth for overlapped pixels, more realistic spreading and dissipation schemes, and computation of the shortwave radiative forcing.

This latter factor has a more direct and immediate impact on the surface temperature and should act to reduce the maximum daytime temperature more than the CLRF increases it. More detailed radiative transfer modelling will be needed for accurately estimating the shortwave component of the radiation effect. The radiative forcing will then need to be translated into changes in the surface air temperatures over the region to determine of the magnitude of the anomalies reported by Travis et al. (2003) can be realistically attributed to the absence of contrails during the shutdown. Additional improvements to the simulation should account for variations in contrail optical depths and dissipation rates in order to make the contrails more realistic.
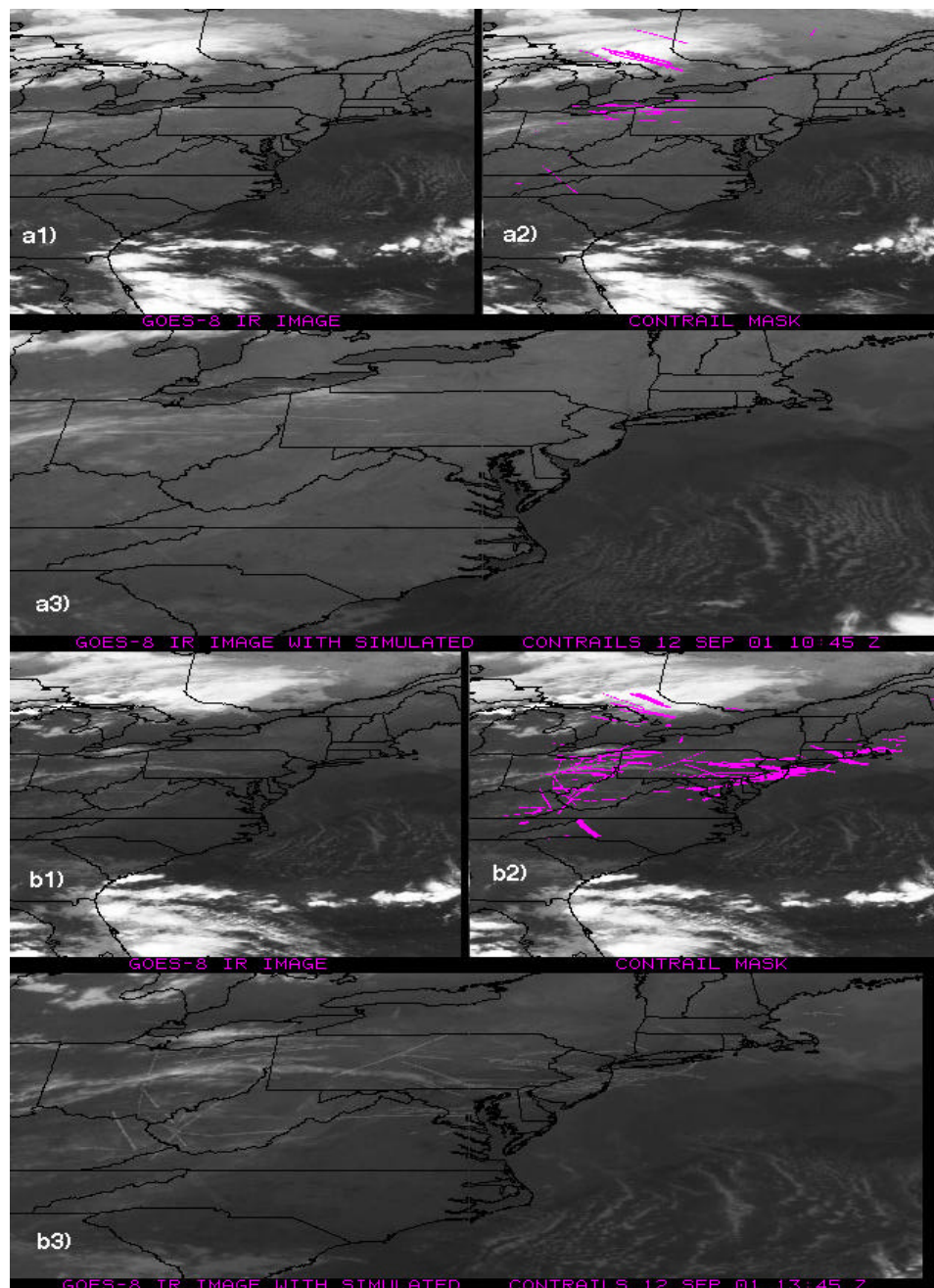
Figure 4. Simulated contrails for 12 September 2001 over northeastern USA. (a) 1045 UTC, (b) 1345 UTC. (1) GOES-8 IR image, (2) IR image with locations of simulated contrails, (3) IR image with simulated contrail IR brightness temperature.
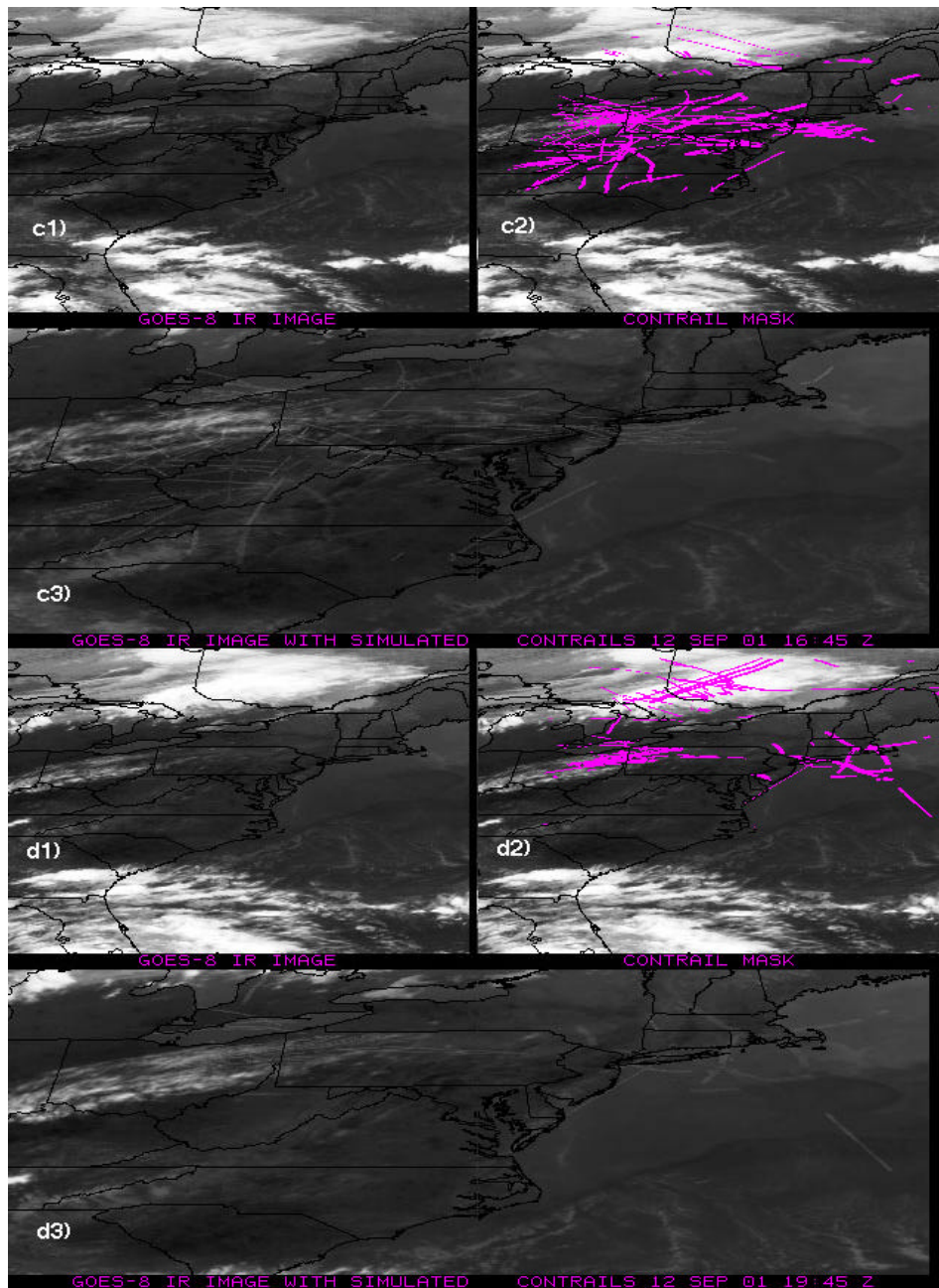
Figure 4 continued. (c) 1645 UTC and (d) 1945 UTC.
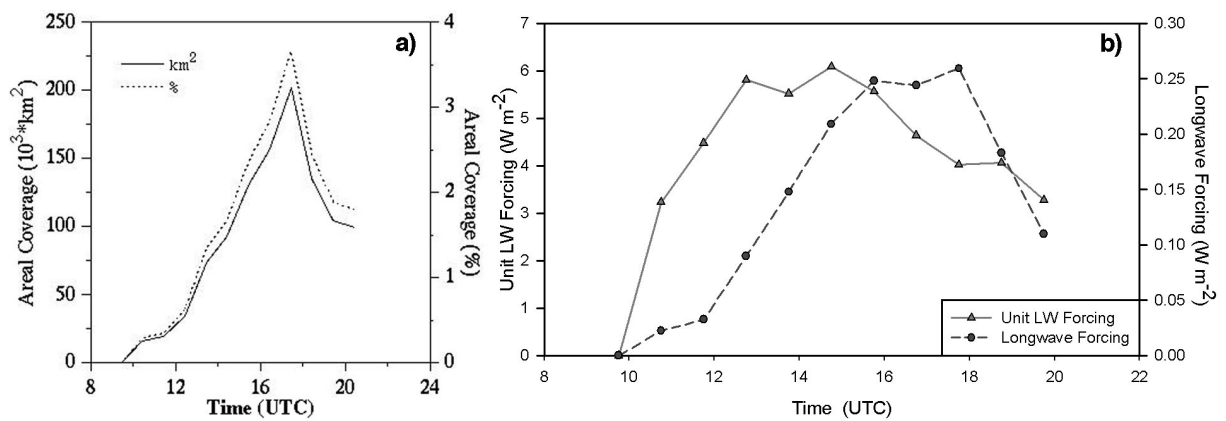
Figure 5. Simulated contrail effects over northeastern USA, 12 September 2001. (a) contrail coverage. (b) contrail longwave radiative forcing.

4 CONCLUDING REMARKS

This initial simulation during the air traffic shutdown, in general, appears to produce realistic contrails. They form in areas where the military contrails persist and are similar in appearance. They also dissipate in areas free of natural cirrus clouds. The analysis confirms the existence of large areas of clear, ice-supersaturated air that are available for additional cirrus formation. The simulations demonstrate that a huge area of contrails would have formed over the northeastern USA if air traffic was normal. This result may help explain of the temperature anomaly found over the same area. With the projected improvements, this simulation should help improve the prediction of contrail formation conditions and contrail lifetimes, and eventually aid the development of reliable predictions of future air traffic effects.

REFERENCES

Benjamin, S. A., G. A. Grell, J. M. Brown, T. G. Smirnova, and R. Bleck, 2003: Mesoscale weather prediction with the RUC hybrid isentropic / terrain-following coordinate model. *Mon Wea. Rev.*, accepted.

Duda, D. P., P. Minnis, P. K. Costulis, and R. Palikonda, 2003: CONUS contrail frequency estimated from RUC and flight track data. *Proc. European Conf. Aviation, Atmosphere, and Climate*, Friedrichshafen at Lake Constance, Germany, June 30 - July 3.

Duda, D. P., P. Minnis, L. Nguyen, and R. Palikonda, 2003: A case study of contrail evolution over the Great Lakes. *J. Atmos. Sci.,* In press.

Garber, D. P., P. Minnis, and P. K. Costulis, 2003: A USA commercial flight track database for upper tropospheric aircraft emission studies. *Proc. European Conf. Aviation, Atmosphere, and Climate*, Friedrichshafen at Lake Constance, Germany, June 30 - July 3.

Miloshevich, L. M., H. Vömel, A. Paukkunen, A. J. Heymsfield, and S. J. Oltmans, 2001: Characterization and correction of relative humidity measurements from Vaisala RS80-A radiosondes at cold temperatures. *J. Atmos. Oceanic Technol.* **18,** 135-156.

Minnis, P. and W. L. Smith, Jr., 1998: Cloud and radiative fields derived from GOES-8 during SUCCESS and the ARM-UAV Spring 1996 Flight Series. *Geophys. Res. Lett.*, **25**, 1113-1116.

Minnis, P., Y. Takano, and K.-N. Liou, 1993: Inference of cirrus cloud properties using satellite-observed visible and infrared radiances, Part I: Parameterization of radiance fields. *J. Atmos. Sci.*, **50**, 1279-1304.

Minnis, P., L. Nguyen, D. P. Duda, and R. Palikonda, 2002: Spreading of isolated contrails during the 2001 air traffic shutdown. *10th AMS Conf. Aviation, range, and Aerospace Meteorol.*, Portland, OR, May 13-16, 33-36.

Palikonda, R., D. N. Phan, V. Chakrapani, and P. Minnis, 2003: Contrail coverage over the USA from MODIS and AVHRR data. *Proc. European Conf. Aviation, Atmosphere, and Climate*, Friedrichshafen at Lake Constance, Germany, June 30 - July 3.

Travis, D., A. Carleton, and R. Lauritsen, 2002: Contrails reduce daily temperature range. *Nature*, **418**, 601.

CONUS Contrail Frequency Estimated from RUC and Flight Track Data

D. P. Duda[*]
Hampton University, Hampton, VA USA

P. Minnis, P. K. Costulis
Atmospheric Sciences, NASA Langley Research Center, Hampton, VA USA

R. Palikonda
Analytical Services and Materials, Inc., Hampton, VA USA

Keywords: air traffic, contrail coverage

ABSTRACT: Estimates of contrail frequency and coverage over the continental United States (CONUS) are developed using hourly meteorological analyses from the Rapid Update Cycle (RUC) numerical weather prediction model and commercial air traffic data from FlyteTrax. The potential contrail frequency over the CONUS is computed directly from RUC analyses using a modified form of the classical Appleman criteria for persistent contrail formation. The potential contrail frequency is adjusted to account for the occurrence of thick cloudiness in possible regions of persistent contrail formation. The air traffic density data is then combined with the potential contrail frequency to estimate the expected contrail coverage. This estimate is compared with a direct satellite estimate of contrail coverage based on an empirical contrail detection algorithm.

1 INTRODUCTION

Contrails can affect the global atmospheric radiation budget by increasing planetary albedo and reducing infrared emission. Our current knowledge of the magnitude of these effects is extremely uncertain; two recent estimates of global linear contrail radiative forcing (Minnis et al., 1999; Ponater et al., 2002) differ by nearly two orders of magnitude. Global radiative forcing is difficult to estimate since it depends on several poorly known factors including the global mean contrail coverage. Current theoretical estimates of global contrail coverage (Sausen et al., 1998; Ponater et al., 2002) are tuned to early estimates of linear contrail coverage determined visually from infrared satellite imagery over the North Atlantic and central Europe (Bakan et al., 1994). The estimates differ based on the parameterization used to diagnose contrails and the numerical weather analyses employed to determine the ambient conditions. Recent estimates of contrail coverage over these areas from an objective detection algorithm (Mannstein et al., 1999; Meyer et al., 2002) are significantly smaller than those given by Bakan et al. (1994). Additionally, a comparison of the empirical contrail coverage of Sausen et al. (1998) with contrail coverage analyses of Advanced Very High Resolution Radiometer (AVHRR) data taken over the continental United States (CONUS) (Palikonda et al., 1999) show they compare well in overall magnitude of coverage, but differ in spatial distribution. These results illustrate the current uncertainty in contrail coverage estimation, a key component in the determination of contrail climate effects.

Development of reliable methods for diagnosing persistent contrails and their physical and radiative properties from numerical weather analyses is essential for predicting future contrail climate impacts. Because air traffic is expected to grow by 2 to 5% annually (Minnis et al., 1999), it is becoming more important to estimate contrail coverage accurately.

To address this concern, we use actual flight data and coincident meteorological data to compute an estimate of contrail coverage over the CONUS. This estimate is compared with a satellite retrieval of contrail coverage based on an objective contrail detection algorithm.

[*]*Corresponding author:* David P. Duda, NASA Langley Research Center, Mail Stop 420, Hampton, VA 23681-2199 USA. Email: d.p.duda@larc.nasa.gov

2 DATA

2.1 *Air traffic data*

Commercial air traffic data from the FlyteTrax product (FT; FlyteComm, Inc., San Jose, CA) as compiled by Garber et al. (2003) were used to determine air traffic density over the continental United States during September 2001 and November 2001. The database consists of 2 or 5-minute readings of aircraft (flight number, aircraft type), position (latitude, longitude, altitude), and heading for every non-military flight over the USA and a portion of Canada, including related transoceanic flights. Although the FT database does not include military flights, it contains most of the air traffic over the CONUS. Air traffic densities were tabulated on a 1°×1° grid that extends from 20°N to 50°N in latitude, and from 135°W to 60°W in longitude.

2.2 *Meteorological data*

Atmospheric profiles of temperature and humidity were derived from the 40-km resolution, 1-hourly Rapid Update Cycle (RUC) analyses (Benjamin et al., 1998) in 25-hPa intervals from 400 hPa to 150 hPa. The RUC data were linearly interpolated at each pressure level to a 1°×1° grid that extends from 25°N to 56°N in latitude, and from 129°W to 67°W in longitude.

The RUC analyses at 00 UTC and 12 UTC were not used in this study to insure that the humidity fields for each hour were consistent. Before February 2002, a "quick-look" version of the 00 UTC and 12 UTC analyses was used. This version of the analysis does not include all available radiosonde data, and is noticeably drier in the upper troposphere than the analyses from other hours.

A major revision to the operational RUC model was implemented on 17 April 2002. The RUC20 model with 20-km horizontal resolution replaced the RUC40 model with 40-km horizontal resolution. The primary motivation for changes in the RUC model was improved quantitative precipitation forecasts. As a result, several changes in the way the model handles upper tropospheric moisture were added, including a more sharply defined tropopause, and the removal of most ice supersaturations for pressure levels less than 300 hPa (Benjamin et al., 2002).

The effect of these changes was to make the upper troposphere drier than in the RUC40. Thus, the relative humidity thresholds used to make the contrail diagnoses had to be changed for the RUC20. A serendipitous discovery of nearly simultaneous RUC20 (19 UTC) and RUC40 (20 UTC) model analyses from 26 May 2002 was used to relate the RUC20 humidity data to the older RUC40 data. The relative humidities with respect to ice (RHI) from the RUC20 analyses were adjusted based a level-by-level comparison of the mean RHI computed from the RUC20 and RUC40 data.

2.3 *Satellite data*

The satellite datasets for deriving contrail and cloud coverage consist of infrared radiances from the Sun-synchronous *NOAA-16* AVHRR 1-km imager (10.8 and 12.0 µm) and multispectral 1-km data from the MODerate Resolution Imaging Spectroradiometer (MODIS) on the *Terra* satellite. Half-hourly infrared data from the Geostationary Operational Environmental Satellite (*GOES* 8) imager (4-km resolution, 10.8 and 12.0 µm) was also used for tracking contrails over the continental US.

3 METHOD

Persistent contrail formation was computed according to the classical criteria of Appleman (1953) using the RUC profiles of temperature and humidity. The contrail formation algorithm follows Schrader (1997), modified with the aircraft propulsion efficiency parameter (η) of Busen and Schumann (1995). The mean value of the propulsion efficiency assumed for the present commercial fleet was 0.30 (Sausen et al., 1998). The saturation vapor pressure coefficients of Alduchov and Eskridge [1996, AERW(50,-80) and AERWi(0,-80)] were used to compute saturation vapor pressure over water and ice.

According to classical contrail formation theory, contrails can persist when the ambient air is supersaturated with respect to ice (that is, the environmental RHI is greater than 100 percent), but not with respect to water. In Sausen et al. (1998), the use of ECMWF reanalysis data required a contrail parameterization to compute persistent contrail coverage since the RHI in the ECMWF

model rarely exceed 100 percent. The RUC model contains a sophisticated cloud and moisture scheme that allows for ice-supersaturation. Assuming that the RUC upper tropospheric moisture variables are accurate, we can follow a much simpler statistical evaluation of potential persistent contrail frequency. For each $1° \times 1°$ grid location where the criterion for persistent contrails occurs at any level from 400 hPa to 150 hPa, a persistence indicator is given a value of 1 for each hourly analysis. The indicator equals zero when none of the levels satisfies the persistence criterion. The potential contrail frequency (PCF) over a time period becomes simply the frequency of occurrence of the persistence indicator at a particular location.

To compute the actual contrail coverage, the PCF must be multiplied by the air traffic density. For an initial estimate, we will assume that the air traffic density is sparse enough to relate contrail fractional coverage to traffic density linearly. An unknown quantity is the mean fractional persistent contrail coverage within an area resulting from a single flight track (c_{flt}). In this study c_{flt} was tuned so that the US mean contrail coverage would match monthly satellite-based contrail coverage estimates (Palikonda et al., 2003). The value of c_{flt} varied by only 5 percent between September 2001 (5.86×10^{-5}) and November 2001 (5.57×10^{-5}). Since the mean area of a $1° \times 1°$ grid cell in the midlatitudes is approximately 10,000 km^2, the mean coverage from a single flight track within a grid cell would be about 0.6 km^2. No overlap of the contrails is assumed because the coverage is tuned to a satellite estimate and contrail altitude is not considered in this study. The total persistent contrail coverage (c_{sum}) in a grid cell is simply

$$c_{sum} = P \times c_{flt} \times n \tag{1}$$

where P is the potential contrail frequency, c_{flt} is the mean fractional persistent contrail coverage within a grid cell from a single flight track, and n is the total number of flight tracks within a grid cell. To account for the effects of natural cloudiness obscuring the detection of contrails, the persistence indicator used in the computation of PCF was set to zero whenever a grid box was more than 50 percent covered by high cloud.

4   RESULTS AND DISCUSSION

4.1   *Potential contrail frequency*

Figures 1 and 2 present the potential contrail frequency computed for September 2001 and November 2001 respectively. RUC analyses were available for only 26 of 30 possible days during each month. In both figures, the region with the highest PCF was the Pacific Northwest, where values reach 0.33 in September and 0.50 in November. Another region of high frequency in November is the eastern Midwest portion of the US. The overall distribution and the magnitude of potential contrail frequency changed dramatically as a result of changes in the synoptic-scale weather patterns between September and November. The mean PCF for grid points over the continental US was 0.118 in September and increased to 0.272 in November.
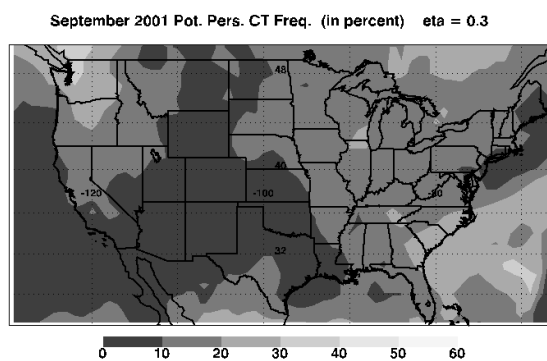

Figure 1: Potential persistent contrail frequency computed from RUC analyses for September 2001.
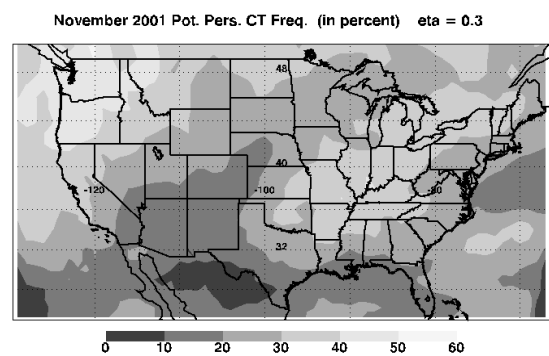
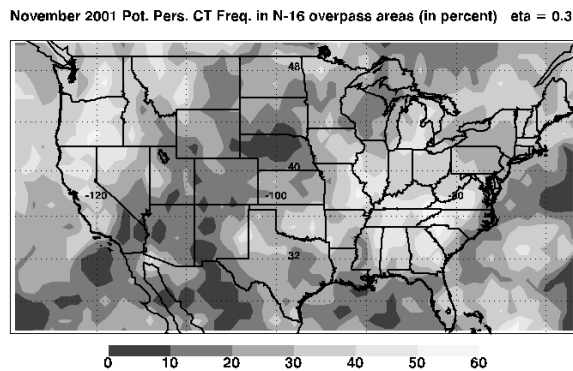Figure 2: Potential persistent contrail frequency computed from RUC analyses for November 2001.

Figure 3. Potential persistent contrail frequency computed from RUC analyses during available RUC afternoon overpass times for November 2001.
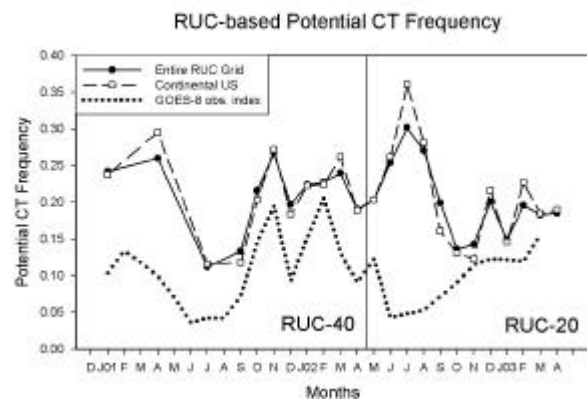

Figure 4. Time series of potential contrail frequency computed from RUC analyses between December 2000 and April 2003. The solid line is the frequency computed for all RUC grid points, while the dashed line only includes grid points over the CONUS. The dotted line indicates the *GOES-8* observation index.

Figure 3 presents the PCF computed for November 2001 during 54 afternoon overpasses of the *NOAA-16* satellite. To approximate the satellite coverage in the calculation of the contrail frequencies, only grid points within ±12 degrees of longitude of the sub-satellite point at 37°N were counted during each overpass. Although the mean potential contrail frequency computed for the CONUS region was almost identical to the monthly average (0.269), the distribution of PCF shows much more variability due to the limited sample size.

To check the quality of the RUC-based potential contrail frequencies, they were compared to a daily, manual analysis of CONUS contrail coverage based on 4-km *GOES-8* imagery. The 10.8 μm minus 12.0 μm brightness temperature difference images between 1045 UTC and 0045 UTC were examined for the occurrence of contrails within each state of the US. For each day of the analysis, a persistence indicator value of 1 was given for each state in which at least one contrail appeared. The contrail frequency for each state is simply the percentage of the total analysed days with contrail occurrence. The mean of the contrail frequency for all states in the CONUS region was defined as the observation index. The comparison is shown in Figure 4.

As expected, the contrail frequencies computed from the RUC model are higher than the observation index since the index is based on observations of 4-km resolution data that miss narrow contrails. In addition, any satellite-based estimate is affected by obscuration by natural clouds. Both the potential contrail frequencies and the observation index show a similar seasonal cycle except for the summer months of 2002 when the RUC20 model data was used. The overestimate in potential contrail frequency during this period is likely the result of differences in the convective parameterization between the RUC40 and the RUC20.

4.2 *Contrail coverage*

Figure 5 shows a plot of persistent contrail coverage c_{sum} (assuming contrail coverage is proportional to air traffic density) computed for November 2001. The contrail coverage is heavily influenced by the air traffic density pattern, and is similar in appearance to Sausen et al. (1998), with a maximum of more than 0.03 in the eastern half of the CONUS, and relatively little coverage in the northern Great Plains. The mean theoretical contrail coverage for the CONUS is 0.0092. In high air traffic regions, however, contrail coverage may not be linearly related to air traffic density due to "saturation" effects (i.e. competition for moisture or overlapping of contrails in air traffic corridors may limit the number of linear contrails that are visible by satellite). If a square-root relation between coverage and air traffic is assumed, the contrail coverage is less dependent on air traffic density (Figure 6). High cloud coverage (cloud tops > 5 km) for November 2001 (see Figure 7) was derived from *Terra* MODIS multispectral observations (Minnis et al., 2002), and was used in the estimate of c_{sum} to account for the effects of natural cloudiness obscuring the detection of contrails.

The satellite-based CONUS contrail coverage estimates for September and November 2001 (Palikonda et al., 2003) used NOAA AVHRR data and an objective contrail detection algorithm (Mannstein et al., 1999) to compute contrail coverage. The results from both September (not shown) and November (Figure 8) suggest that the contrail coverage may be more dependent on the potential contrail coverage (in other words, the environmental conditions) than the estimates in Figures 5 and 6 suggest. Several unresolved factors may account for this difference. These factors include the likelihood that contrail coverage is non-linearly related to air traffic density, and the contrail coverage saturates in high traffic areas. Also, the current analysis neglects the advection of contrails and assumes that the RUC40 analyses provide an accurate characterization of the upper tropospheric temperature and moisture fields over the entire domain.
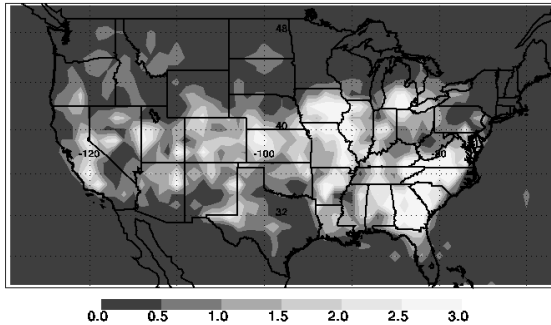

Figure 5: Persistent contrail coverage computed for November 2001 assuming linear relationship between contrail coverage and air traffic density.
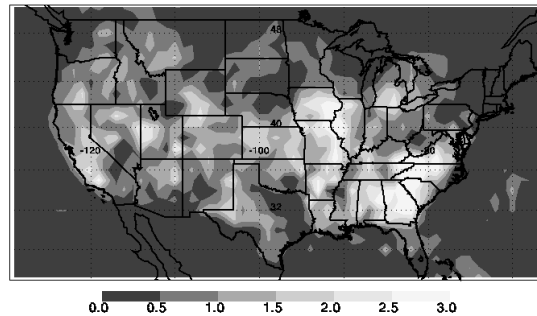

Figure 6: Persistent contrail coverage computed for November 2001 assuming square root relationship between contrail coverage and air traffic density.
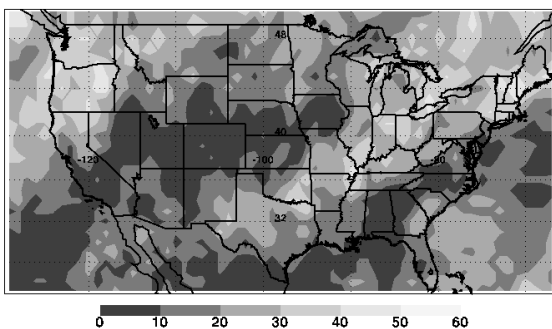
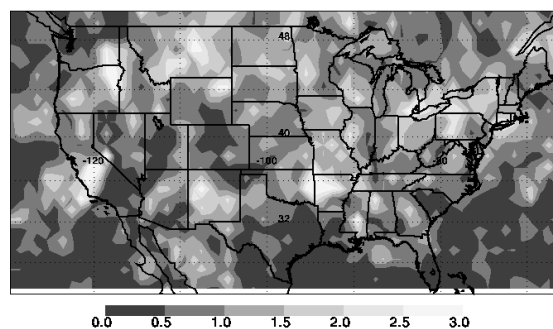Figure 7. Cloud coverage above 5 km computed from *Terra* morning overpass measurements.

Figure 8. Contrail coverage computed from *NOAA-16* afternoon overpasses for November 2001 using an objective analysis.

5 CONCLUSIONS AND FUTURE WORK

The simulated persistent contrail coverage presented here is heavily influenced by the air traffic pattern, similar to earlier studies. The contrail coverage computed from *NOAA-16* imagery, however, is more closely related to the potential contrail frequency (and high cloud coverage) than air traffic density. Thus, the coverage of *line-shaped* contrails is non-linearly related to air traffic, and "saturation" effects are important in high traffic areas. Additional tuning and testing of the contrail coverage estimates is in progress. More work is necessary to compare satellite-based estimates of contrail coverage with potential coverage diagnosed from RUC analyses. The effects of flight altitude, synoptic-scale vertical motions, contrail advection, and RUC uncertainties have not been included in this study. More *NOAA-16* data must be analysed since a sample size of one or two months is still too small. The results from other satellite platforms such as *NOAA-17* (with a

crossover time approximately 4 hours before *NOAA-16*) would help determine whether the relation between contrail coverage and air traffic changes throughout the day.

REFERENCES

Alduchov, O. A., and R. E. Eskridge, 1996: Improved Magnus form approximation of saturation vapor pressure. *J. Appl. Meteor. 35,* 601–609.

Appleman, H., 1953: The formation of exhaust condensation trails by jet aircraft. *Bull. Amer. Meteor. Soc. 34,* 14–20.

Bakan, S., M. Betancor, V. Gayler, and H. Grassl, 1994: Contrail frequency over Europe from NOAA-satellite images. *Ann. Geophys. 12,* 962–968.

Benjamin, S. G., J. M. Brown, K. J. Brundage, B. E. Schwartz, T. G. Smirnova, and T. L. Smith, 1998: The operational RUC-2. In: *Preprints, 16th AMS Conference on Weather Analysis and Forecasting,* Phoenix, AZ. American Meteorological Society, Boston, USA, pp. 249-252.

Benjamin, S. G., J. M. Brown, K. J. Brundage, D. Dévényi, G. A. Grell, D. Kim, B. E. Schwartz, T. G. Smirnova, T. L. Smith, S. S. Weygandt, and G. S. Manikin, 2002: RUC20 – The 20-km version of the Rapid Update Cycle. *NWS Technical Procedures Bulletin No. 490.*

Busen, R., and U. Schumann, 1995: Visible contrail formation from fuels with different sulfur contents. *Geophys. Res. Lett. 22,* 1357–1360.

Garber, D. P., P. Minnis, and K. P. Costulis, 2003: A USA commercial flight track database for upper tropospheric aircraft emission studies. In: *Proceedings of the European Conference on Aviation, Atmosphere, and Climate,* June 30 - July 3, 2003, Friederichshafen at Lake Constance, Germany.

Mannstein, H., R. Meyer, and P. Wendling, 1999: Operational detection of contrails from NOAA-AVHRR-data. *Int. J. Remote Sensing 20,* 1641–1660.

Meyer, R., H. Mannstein, R. Meerkötter, U. Schumann, and P. Wendling, 2002: Regional radiative forcing by line-shaped contrails derived from satellite data. *J. Geophys. Res. 107 (D10), doi: 10.1029/ 2001JD000426, 31 May 2002.*

Minnis, P., U. Schumann, D. R. Doelling, K. M. Gierens, and D. W. Fahey, 1999: Global distribution of contrail radiative forcing. *Geophys. Res. Lett. 26,* 1853–1856.

Minnis, P., D. F .Young, B. A. Wielicki, D. P. Kratz, P. W. Heck, S. Sun-Mack, Q. Z. Trepte, Y. Chen, S. L. Gibson, R. R. Brown, 2002: Seasonal and diurnal variations of cloud properties derived for CERES from VIRS and MODIS data. In: *Proceedings of the 11th AMS Conference on Atmospheric Radiation*, June 3 - 7, 2002, Ogden, Utah, USA, pp.20-23.

Palikonda, R., P. Minnis, D. R. Doelling, P. W. Heck, D. P. Duda, H. Mannstein and U. Schumann, 1999: Potential radiative impact of contrail coverage over continental USA estimated from AVHRR data. In: *Preprints, 10th AMS Conference on Atmospheric Radiation,* June 28-July 2, 1999, Madison, Wisconsin. American Meteorological Society, Boston, USA, pp. 181-184.

Palikonda, R., D. N. Phan, and P. Minnis, 2003: Contrail coverage over the USA derived from MODIS and AVHRR data. In: *Proceedings of the European Conference on Aviation, Atmosphere, and Climate,* June 30 - July 3, 2003, Friederichshafen at Lake Constance, Germany.

Ponater, M., S. Marquart, and R. Sausen, 2002: Contrails in a comprehensive global climate model: Parameterization and radiative forcing results. *J. Geophys. Res. 107, 10.1029/2001JD000429, 3 July 2002.*

Sausen, R., K. Gierens, M. Ponater, and U. Schumann, 1998: A diagnostic study of the global distribution of contrails. Part I: Present day climate. *Theor. Appl. Climatol. 61,* 127–141.

Schrader, M. L., 1997: Calculations of aircraft contrail formation critical temperatures. *J. Appl. Meteor. 36,* 1725–1729.

Contrail Coverage Derived from UARS MLS Measurements

M.Y. Danilin[*], S.L. Baughcum
The Boeing Company, Seattle, Washington, USA

W.G. Read
NASA JPL, Pasadena, California, USA

Keywords: contrails, satellite measurements

ABSTRACT: We use Upper Atmosphere Research Satellite (UARS) Microwave Limb Sounder (MLS) measurements of relative humidity above ice (RHI) during 1991-1997 and the NASA 1992 air traffic scenario for deriving global contrail coverage. Additionally, we perform sensitivity studies of our results to subgrid processes and higher propulsion efficiency of future aircraft. We found that while our results are reasonably consistent with previously published model calculations and measurements, there are several poorly justified tuning parameters in contrail calculations and limitations of the MLS measurements used. Better RHI data sets near the tropopause and additional work is required in order to improve estimates of contrail coverage and optical properties.

1 INTRODUCTION

Condensation trails (contrails) are formed when hot and humid aircraft exhaust is mixed with cold and dry ambient air (Appleman, 1953). Contrails are the most uncertain aspect of the aviation impact on the atmosphere contributing to the climate change (IPCC, 1999). Indeed, uncertainties of direct radiative forcing (RF) by contrails are at least several times larger than those caused by aircraft CO_2 emissions, while indirect effects of contrails (i.e. via change of cloudiness) are even more uncertain (IPCC, 1999). Contrail RF on the global scale depends on their coverage and optical properties. Since only long-lived contrails, which persist at ice-supersaturated conditions, are important for climate change, high fidelity RHI measurements with good vertical and horizontal resolution over the globe are required for these calculations. Unfortunately, such an RHI data set does not exist yet. Usually, assimilated RHI values from the European Centre for Medium Weather Forecast (ECMFW) (Sausen et al., 1998) or ECHAM4 GCM calculations (Ponater et al., 2002) are used for contrail analysis. However, water vapor (H_2O) and temperature (T) (which are used to derive RHI) in the ECHAM4 GCM deviate from those observed in the real atmosphere (Marquart et al., 2003), thus introducing poorly quantified errors in contrail calculations. In order to avoid the use of potentially incorrect H_2O and T, we decided to use MLS measurements of RHI for our contrail calculations. We focus our paper on calculations of global contrail coverage only and perform several sensitivity studies of our results to parameters and assumptions used in our calculations.

2 DATA USED

The UARS MLS instrument retrieves humidity near the tropopause by using the 203 GHz radiometer (Read et al., 2001). MLS provides 1318 profiles daily with a vertical resolution of approximately 3 km and horizontal resolution of 100 km x 200 km covering the latitude band from 80°S to 80°N. We utilize MLS version 4.9 level 2 RHI data spanning the time period from October 1991 to October 1997 at the 316, 215, and 147 hPa pressure levels. We ignored MLS individual profiles with negative uncertainty and values larger than 230% following the recommendations of Read et al. (2001). In our analysis we used MLS measurements grouped in a 2°x2° resolution in January, March, July, and October, which provides 112,000-141,000 individual profiles for each

---

[*] *Corresponding author:* Dr. Mikhail Y. Danilin, The Boeing Company, MS 02-XL, P.O. Box 3707, Seattle, WA 98124-3707, USA. Email: Mikhail.Y.Danilin@boeing.com.

month. Since contrail evolution is a non-linear function of RHI, we calculated the RHI probability distribution (instead of RHI mean value) for each grid box for our contrail coverage calculations described below.

We used scheduled civil aircraft inventory for 1992 (Baughcum et al., 1996) using the distance flown as a measure of air traffic. The scheduled aviation flew about 9.5×10^9 nautical miles in 1992 with most intensive traffic in the Northern hemisphere (93% of all traffic).

3 ESTIMATING CONTRAIL COVERAGE

Our analysis is focused on long-lived contrails, which persist at ambient conditions with RHI≥100% and may affect climate. The following steps were made for estimating contrail coverage:

1) We checked that a contrail is formed at each grid box using the RHI probability distribution and assuming an overall propulsion efficiency of 0.3 (Schumann, 2000).

2) We calculated the contrail probability distribution at each level and each grid following the methodology of Ponater et al. (2002), using the threshold values for contrail and cirrus cloud formation of 50% and 70% for our baseline case. These reduced (i.e., <100%) values are used in order to account for subgrid processes, since it is quite likely that there are small scale ice-supersaturated regions in a 100 km x 200 km x 3 km MLS retrieval volume even at MLS RHI<100%. The values of 50% and 70% used in our baseline case are somewhat arbitrary and we performed a sensitivity run with 95% and 90%.

3) Since the number of contrails is proportional to air traffic, at the next step we calculate contrail coverage in each grid box as a product of the contrail probability and number of flight miles.

4) We determine vertically integrated contrail coverage assuming a random overlap of contrails at individual levels (Sausen et al., 1998).

5) In order to make our calculations consistent with contrail coverage measurements over Europe (Bakan et al., 1994), we normalize the calculated visible contrail coverage field to the value of 0.375% over the region between 35°N-75°N and 30°W and 30°E.

We considered contrails visible if their optical thickness t>0.02. Calculating t, we assumed that:

a) the vertical depth of contrails was 100 m (Ponater et al., 2002),

b) their effective radius depends on ambient temperature and H_2O and is determined according to Lohmann and Kärcher (2002), and

c) optical thickness was derived according to Ebert and Curry (1992).

Our calculations predict that visible contrails account for 80-85% of all contrails.

4 RESULTS AND DISCUSSION

Figure 1 shows the fractional coverage by contrails in a model grid as a function of RHI for the threshold values of contrail RHI_{co} and cirrus cloud formation RHI_{cl} of 50% and 70% (panel a) and 90% and 95% (panel b), respectively. The choice of these threshold values is somewhat arbitrary and our intention is to compare our results with those in Ponater et al. (2002). We applied equations (3) and (10) from Ponater et al. (2002) in deriving results shown in Figure 1. Panel (a) is used as our baseline case, while panel (b) is applied for our sensitivity analysis of the subgrid processes on contrail coverage. The areas under the contrail curves are quite different in these cases and we expect that this fact will affect our contrail coverage results as well.

Figure 2 depicts the geographical distribution of total contrail coverage in July for the RHI_{co} and RHI_{cl} values used in Figure 1. For the baseline case shown in the left panel, maximum contrail coverage is obtained over the regions with the most intensive air traffic, such as the United States, Europe and Japan. When we increased the RHI_{co} and RHI_{cl} values to 95% and 90%, respectively, and kept the contrail coverage equal to 0.375% over Europe (shown by a black rectangle) according to Bakan et al. (1994), the pattern of contrail coverage became more spotty. This behaviour may be understood as follows: for the small values of RHI_{co} and RHI_{cl}, the fractional coverage by contrails is a relatively broad function of RHI (see Figure 1), hence the pattern of contrails formed under broader atmospheric conditions and their coverage is similar to the air traffic pattern; while for high values of RHI_{co} and RHI_{cl}, the contrail coverage is determined by the geographical patterns of high

RHI in the ambient atmosphere. In order to better quantify the difference between these two runs, we show the results for visible contrail coverage in Table 1. To summarize, lack of knowledge about subgrid processes makes contrail calculations quite uncertain for some regions, such as Japan, where difference can easily be as large as a factor of 1.5.

Figure 1. Fractional coverage of contrail and cloud in a grid box as a function of RHI for the threshold values shown.
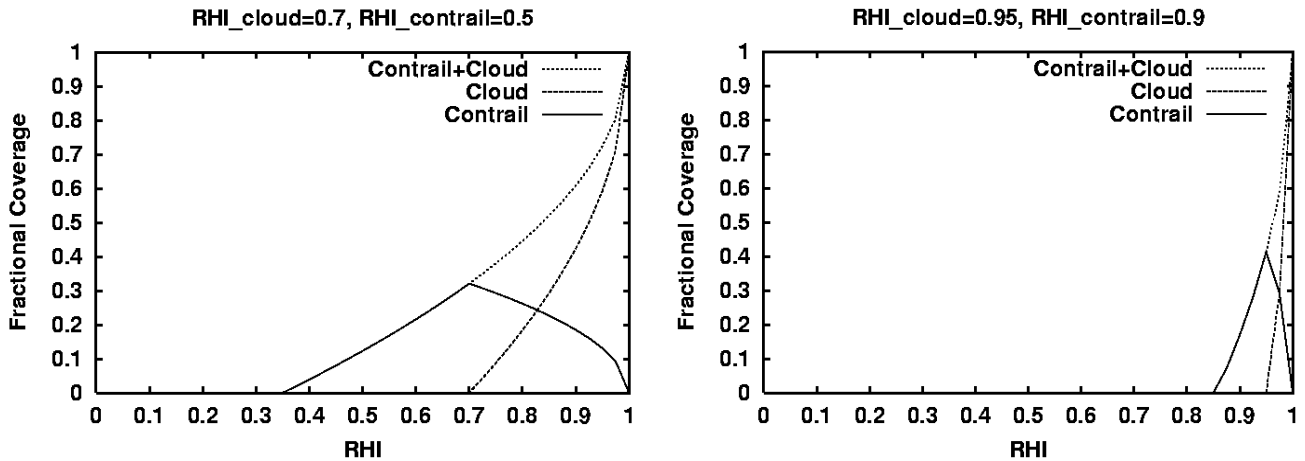

Table 1 compares our results for different sensitivity studies with available measurements. Overall, our baseline case calculations (third column) agree within 20%-40% with the observations at mid-latitudes. The largest discrepancies are obtained for the Thailand and Japan regions. It is possible that normalization of our results to the Bakan et al. (1994) data over Europe does not work in these regions. Indeed, this conventional way to normalize contrail coverage (Sausen et al., 1998; Ponater et al., 2002) implies that the probability distributions and uncertainties of RHI over Europe are the same for all other parts of the world regardless of local meteorology. This assumption is not very good, thus stimulating scientists to find a better way to account for available measurements in future contrail coverage calculations.

The fourth column of Table 1 depicts relatively high sensitivity of the contrail coverage to our representation of subgrid processes (i.e., RHI_{cl}=95% and RHI_{co}=90%), particularly over USA and Japan. Obviously, results for Western Europe were little changed, since normalization over Europe remained intact.

The right column of Table 1 shows that the derived contrail coverage is not very sensitive to the vertical interpolation of MLS data from its 3 km vertical resolution to a 1 km vertical resolution of the air traffic scenario. In all of our previous cases, we linearly interpolated MLS RHI data, while in this last case we first linearly interpolated MLS H_2O and T values and then calculated RHI for the interpolated values of H_2O and T. The RHI_{co} and RHI_{cl} values of 50% and 70% were used in this case.

Future aircraft engines will have a higher propulsion efficiency (i.e., larger fraction of the fuel energy will be used to propel an airplane) (Schumann, 2000). Since the increased propulsion efficiency facilitates contrail formation, it is important to estimate its effect on contrail coverage. Figure 3 shows the increase of contrail coverage at two individual levels of the most intensive traffic at 10.5 and 11.5 km when propulsion efficiency is increased from 0.3 to 0.4. We found a tiny effect of the order of 0.01-0.02% over USA and Europe with even smaller effect in a vertically integrated contrail coverage. Thus, our results show that current atmospheric conditions are far from the threshold conditions for contrail formation and confirm a similar conclusion by Sausen et al. (1998).

Table 1. Annual visible contrail coverage (in %) according to the observations and our calculations with different threshold values and when vertical interpolation of MLS RHI measurements is used. The regions shown are defined as follows: USA (25ºN-55ºN, 130ºW-65ºW), Western Europe (40ºN-55ºN, 10ºW-20ºE), Japan (30ºN-48ºN, 126ºE-148ºE), and Thailand (0ºN-25ºN, 90ºE-120ºE). Observations for USA, Western Europe, Japan, and Thailand are based on (Minnis et al., 2003), (Meyer et al., 2002), (Meyer et al., 2003), and (Meyer et al., 2003), respectively.

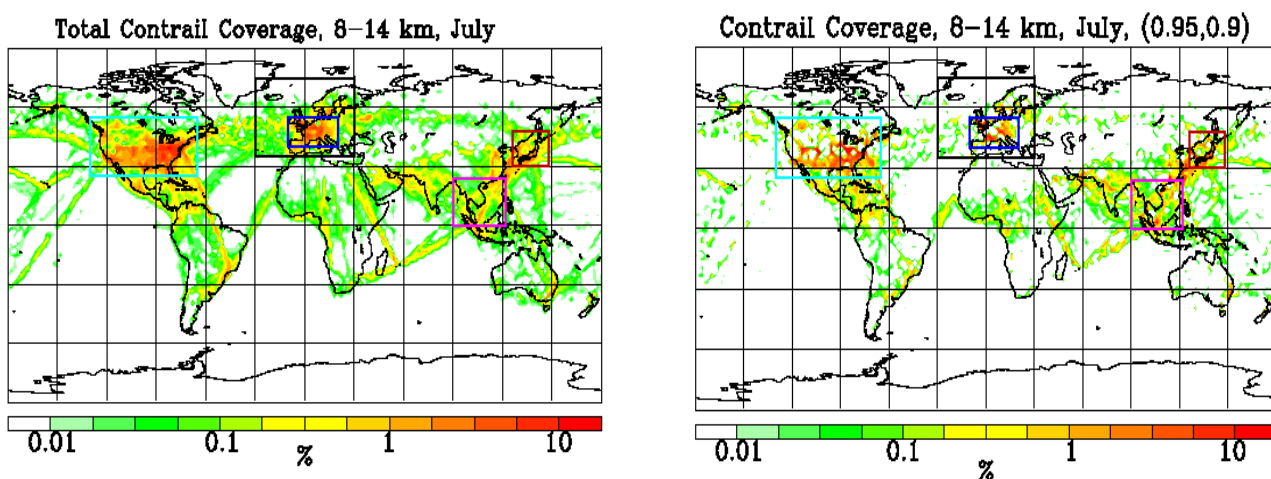| Regions	Observations	70%, 50%	95%, 90%	MLS Interpolation
USA	1.24	0.95	1.26	1.00
Western Europe	0.82	1.11	1.20	1.13
Japan	0.25	0.40	0.63	0.49
Thailand	0.13	0.28	0.24	0.33
World	-	0.09	0.11	0.09

Figure 2. Contrail coverage in July for the RHI_{co} and RH_{cl} values of 50% and 70% (left panel) and 90% and 95% (right panel), respectively.
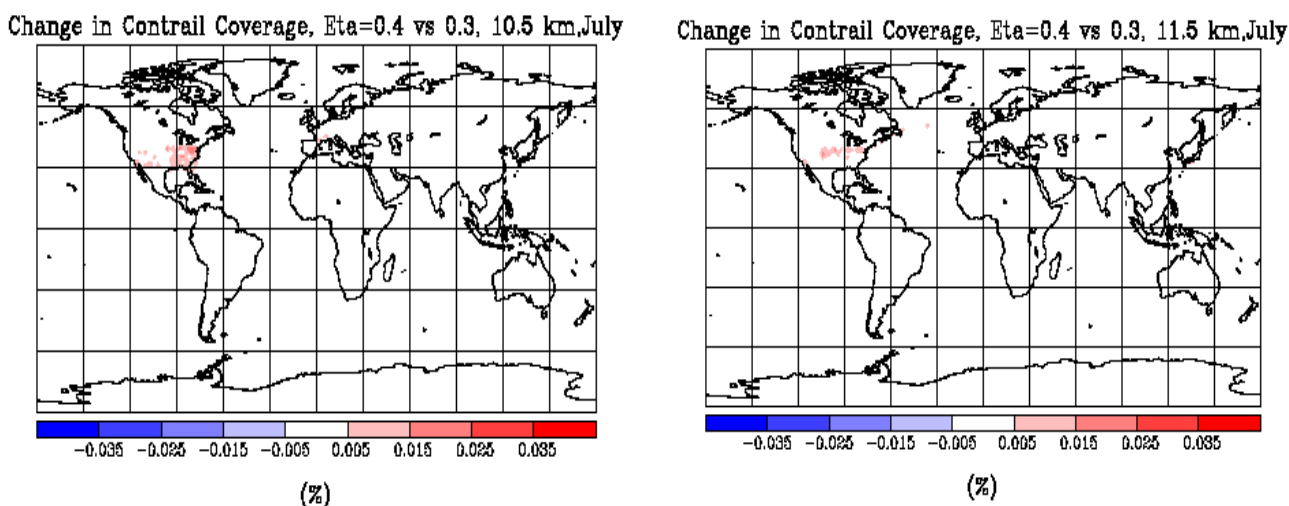

Figure 3. Change in contrail coverage (in %) at flight altitudes of 10-11 km and 11-12 km when the aircraft engine propulsion efficiency increased from 0.3 to 0.4.

5 SUMMARY

We estimated contrail coverage using for the first time UARS MLS measurements of RHI and the 1992 NASA air traffic scenario. Our major findings are:

1) Global and annually averaged visible contrail coverage is calculated to be 0.09% in our baseline case with the contrail and cirrus cloud threshold values of 50% and 70%, respectively; maximum contrail coverage (more than 1%) was predicted in the regions of the most intensive traffic, such as USA, Western Europe, and Japan.

2) Calculated contrail coverage is sensitive to the way that subgrid processes are addressed. For example, we calculated 0.11% of global and annually averaged visible contrail coverage using 95% and 90% as the threshold values for contrail and cirrus cloud formation. It is clear that the using a single set of values to account for subgrid scale variations in RHI at all locations and seasons is not the best approach but there is limited data to use for a more comprehensive analysis.

3) Potential improvements of the propulsion efficiency of future aircraft engines from 0.3 to 0.4 were calculated to not increase contrail coverage significantly.

4) Comparison of calculated contrail coverage with available data shows agreement within 20-40%; we speculate that one of the reasons for this disagreement is that normalization of our results over Europe according to Bakan et al (1994) does not work for other regions, such as the United States or Japan.

In order to improve future analysis of contrail coverage and optical properties, RHI global measurements with a better vertical and spatial resolution are required. For example, the relatively poor vertical resolution of MLS data limits our ability to evaluate the sensitivity of contrail coverge to changes in aircraft cruise altitudes. Future data sets also should span at least several years in order to get better statistics. Likely, merging satellite and in situ measurements (such as MOZAIC campaign data (Gierens et al., 1999)) may help if small-scale processes from in situ data can be properly accounted for in global satellite data. Also, better experimental constraints on the vertical extent of contrails and their optical properties as the contrail age are needed. Similarly, we expect that the optical properties of contrails will depend on temperature and RHI, producing contrails with different size particles. Little data is available on how contrail properties differ in different geographical regions (e.g., tropics versus mid-latitudes) or different seasons.

REFERENCES:

Appleman, H., 1953: The formation of exhaust condensation trails by jet aircraft, *Bull. Amer. Meteor. Soc., 34*, 14-20.

Bakan, S., M. Betancor, V. Gayler, and H. Graßl, 1994: Contrail frequency over Europe from NOAA satellite images, *Ann. Geophys., 12,* 962-968.

Baughcum, S.L., T.G. Tritz, S.C. Henderson, and D.C. Pickett, 1996: Scheduled civil aircraft emission inventories for 1992: Database development and analysis, *NASA Contr. Rep. 4700.*

Ebert, E.E., and J.A. Curry, 1992: A parameterization of ice cloud optical properties for climate model, *J. Geophys. Res., 97*, 3831-3836.

Gierens, K., U. Schumann, M. Helten, H. Smit, and A. Marenco, 1999: A distribution law for relative humidity in the upper troposphere and lower stratosphere derived from three years of MOZAIC measurements, *Ann. Geophys., 17,* 1218-1226.

IPCC, 1999: *Aviation and the global atmosphere,* (eds. J.E. Penner, D.H. Lister, D.J. Griggs, D.J. Dokken, and M. McFarland), Cambridge Univ. Press., 373 pp.

Lohmann, U., and B. Kärcher, 2002: First interactive simulations of cirrus clouds formed by homogeneous freezing in the ECHAM general circulation model, *J. Geophys. Res., 107*, D10, 10.1029/2001JD000767.

Marquart, S., M. Ponater, F. Mager, and R. Sausen, 2003: Future development of contrail cover, optical depth, and radiative forcing: Impacts of increasing air traffic and climate change, *J. Climate, 16,* 2890-2904.

Meyer, R., H. Mannstein, R. Meerkötter, U. Schumann, and P. Wendling, 2002: Regional radiative forcing by line-shaped contrails derived from satellite data, *J. Geophys. Res., 107,* D10, 10.1029/2001JD000426.

Meyer, R., R. Buell, C. Leiter, H. Mannstein, S. Marquart, T. Oki, and P. Wendling, 2003: Contrail observations over Southern and Eastern Asia in NOAA/AVHRR data and comparisons to contrail simulations in a GCM, *Int. J. Rem. Sens., in press*.

Minnis, P., J.K. Ayers, R. Palikonda, and D. Phan, 2003: Contrails, cirrus trends, and climate, *J. Climate, submitted.*

Ponater, M., S. Marquart, and R. Sausen, 2002: Contrails in a comprehensive climate model: Parameterization and radiative forcing, *J. Geophys. Res., 107,* D13, 10.1029/2001JD000429.

Read, W.G., et al., 2001: UARS MLS upper tropospheric humidity measurements: Method and validation*, J. Geophys. Res., 106,* 32,207-32,258.

Sausen, R., K. Gierens, M. Ponater, and U. Schumann, 1998: A diagnostic study of the global distribution of contrails, Part I: Present day climate, *Theor. Appl. Climatol., 61,* 127-141.

Schumann, U., 2000: Influence of propulsion efficiency on contrail formation, *Aerosp. Sci. Techn., 4,* 391-401.

Observations of Contrails and Cirrus Over Europe

H. Mannstein[*], U. Schumann
DLR-Institut für Physik der Atmosphäre Oberpfaffenhofen, Germany

ABSTRACT: Condensation trails (contrails) and aircraft induced cirrus are nowadays a common feature at the mid latitude skies. The impact of aircraft induced cirrus changes has been roughly estimated before from observed decadal trends in cirrus cover but the direct attribution of observed cirrus changes to changes in aviation activity remains uncertain. In this paper the amount of additional cirrus induced from spreading contrails in humid air is estimated from the direct correlation between observed cirrus cover derived with suitable methods from METEOSAT and aviation flight density reported by EUROCONTROL at high spatial and temporal resolution. The results indicate that the radiative forcing from the additional cirrus is at least 10 times higher than that of linear contrails and aviation induced CO_2 increases.

1   INTRODUCTION

A contrail forms in the wake of an aircraft if the ambient air is cold and moist enough. The Schmidt-Appleman criterion quantifies the atmospheric conditions (Schumann, 1996). If the ambient air is not supersaturated with respect to ice, the contrail disappears within the next seconds. Otherwise the ice crystals grow by uptake of ambient moisture while the contrail is spreading due to dissipation and vertical wind shear (Minnis, 1998; Schumann, 2002) In this case the further development of the contrail is governed by the moisture and vertical motion of the ambient air and the sedimentation of the ice particles. Young contrails can be easily identified by their linear appearance (Bakan, 1994; Mannstein 1999), but during their ageing both, their macroscopic structure and their microscopic composition approach that of natural cirrus clouds. Optically thin cirrus has a positive climate impact (Liou,1986; Boucher, 1999) i.e. it warms the Earth – atmosphere system. In the International Panel on Climate Change (IPCC) special report on 'Aviation and the Global Atmosphere' from 1999 the impact of linear (young) contrails is estimated to be in the same order of magnitude as the impact caused by emitted CO_2, the impact of aircraft induced cirrus (i. e. aged contrails and indirect influence on cirrus formation) is not quantified due to the 'very poor' knowledge.

2   AN ESTIMATE OF CONTRAIL CIRRUS COVERAGE

Independent from any measurements of cloud coverage the following considerations give a simplified estimate on the influence of air traffic on cirrus coverage: Over Europe in up to 25% of all cases super-saturation of water vapour with respect to ice is found in measurements performed by instruments operated on regular airliners (Gierens, 1999; Gierens, 2000). In most cases the Schmidt-Appleman criterion for contrail formation is fulfilled within these super-saturated areas. Part of them might be already filled by cirrus clouds or hidden by cirrus layers above, but in the remaining fraction air traffic leads to additional cloud coverage. Here this part of the super saturated regions is called c_{pot}, the fraction in time and space of the total area with potential contrail coverage.

   Horizontal spreading rates of contrails between 1 and 8 km/h with a mean of about 4 km/h are found by Freudenthaler (1995) from tracking and scanning contrails with a LIDAR system. Considering a super saturated air parcel void of any contrails at the beginning, an air traffic density

---

given in km flight-path per km^2 and per hour during a time interval Δt leads to total length of contrails of $d\Delta t$ per unit area. The mean width of the contrails is $s_h \bar{t}$, where $\bar{t}$ is the mean age of the contrails. Therefore the fractional coverage of spreading contrails is:

$$c_f = d\Delta t s_h \bar{t}$$

(1)

Already after 1 h of air traffic, - the mean contrail age is then ½ h-, the full coverage would be reached with an air traffic density of d=0.5[km/km2/h]. Therefore an overlap of the evolving cirrus clouds has to be considered. Assuming N equal contrails, the remaining cloud free part is $1 - c_f = (1 - d\Delta t s_h \bar{t} / N)^N$. In the extreme case of infinitesimal random overlap ($N \rightarrow \infty$) the cirrus coverage reads as:

$$c_f = 1 - e^{-d\Delta t s \bar{t}}$$.

(2)

Looking for the dependency of c_f on d Eq.(2) becomes clearer if $\Delta t s_h \bar{t}$ is replaced by $1/d^*$, where d^* represents the air traffic density leading to a full coverage at a given contrail age, spreading rate and time interval Δt without considering any overlap.

Now the total coverage with cirrus clouds written as a function of air traffic density can be written as:

$$c_{tot}(d) = c_0 + c_{pot}(1 - e^{-\frac{d}{d^*}})$$

(3)

where c_0 gives the background cirrus coverage without any air traffic.

For longer time-scales also the decay of contrail cirrus has to be considered. From tracking cirrus clusters in METEOSAT data from June and July 1998 we found a half-life time in the order of 2.5 hours, but these data include strong mesoscale convective events and might therefore not represent the lifetime of contrail cirrus. Nevertheless the order of magnitude supports the assumption, that cirrus decay can be neglected at least for the first hour.
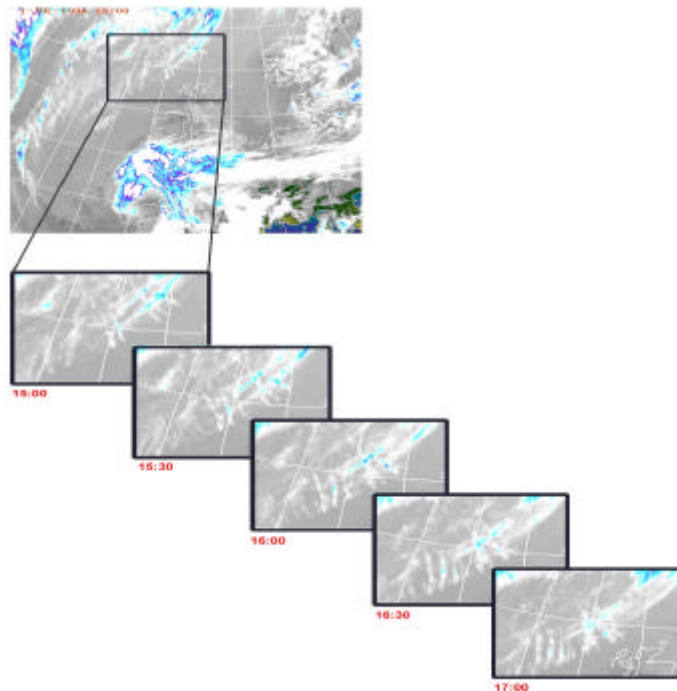

Figure 1: Contrail cirrus in METEOSAT images. Crossing a band of moist air with some cirrus clouds NW of Scotland the westbound air traffic on July 1st 1998 left bundles of contrails which remain visible in the METEOSAT infrared channel data for several hours.
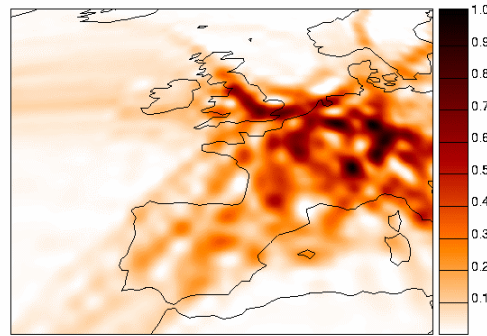
Figure 2: Mean air traffic density in June and July 1998. Flight paths above 8 km altitude according to EUROCONTROL data have been summarised into a $1^0 \times 1^0$ grid. The air traffic density is given in km flight path per km^2 and per hour. The data is mapped into the METEOSAT projection by interpolation. All results refer to the region displayed here.

3   METHODS TO DETECT CIRRUS IN METEOSAT DATA

The main problem in cirrus detection by remote sensing methods is that no natural boundary exists which discriminates cirrus from clear sky. Therefore the amount of detected cirrus depends on the sensitivity of the sensor and the applied algorithm. Different methods will give different absolute values for cirrus coverage. High clouds, which are usually cirrus clouds, can be detected within the METEOSAT data making use of the water vapour (WV) channel, which has it main sensitivity in the upper troposphere. For this study we developed two different methods. The first one is based on the local spatial correlation between the equivalent blackbody temperatures in the infrared (IR) and the WV channel. A high positive correlation indicates an horizontally structured emitter in the upper troposphere - i.e. a high level cloud. Cirrus clouds down to a effective transmissivity in the visible of 0.3 should be detected by this method. The correlation coefficient is calculated for each pixel in a 7 x 7 pixel surrounding weighted with a rotationally symmetric Gaussian filter. A threshold of 0.5 is used to discriminate between background noise and clouds. Additionally all pixels with temperatures colder than -50°C are considered to be covered by cirrus clouds. This method will overestimate the cirrus coverage, as gaps are filled, some pixels adjacent to clouds are included, and the sub-pixel structure is not taken into account. On the other hand single young and narrow contrails cannot be detected, as their effect on the thermal emission is far below the sensitivity of the IR and WV sensors of METEOSAT. The second method has the aim to detect thin cirrus clouds and uses only the information in the WV channel: If the standard deviation of the equivalent blackbody temperature in a 5x5 pixel surrounding exceeds the normal noise level of 0.5 K, a cirrus cloud is assumed. This method detects more cirrus clouds, but has also a higher false alarm rate. To concentrate on thin cirrus clouds, the optically thick and therefore cold high clouds are excluded by a threshold of -50°C. This criterion was chosen to eliminate the possible correlation between strong convective clouds that in summer often occur in the afternoon over land and the air traffic, which also shows its maximum during daytime over land.

4   OBSERVATION OF CIRRUS

The direct observation of cirrus clouds resulting from air traffic is currently not possible because we do not know how to separate these clouds from natural cirrus clouds. Nevertheless the dependency of cirrus coverage on air traffic density as given in Eq.(3) can be verified. Due to the high spatial and temporal variation of air traffic, such a study is only possible with observations from geostationary satellites like METEOSAT. Concerning air traffic data, two data sets of the so called

'corrected scheduled flights' were available from EUROCONTROL, showing the flight path for every commercial flight over Europe defined by the time and altitude of passing way points. The data sets for the two time periods, from June 22 to July 27 1998 and from September 27 to October 21 2000 were processed by summarising all flight paths above 8 km to derive the air traffic density for each hour on an $1^0 x 1^0$ grid.

Cirrus coverage was derived with two different methods from half hourly METEOSAT data, which was obtained from the 'METEOSAT archive and retrieval facility' (MARF) of EUMETSAT. As shown in Fig. 3 the cirrus coverage determined by both methods increases with the air traffic density as expected by Eq. 3. In this figures the air traffic data within each hour is compared to the satellite data at the end of this hour. Therefore a Δt of 1 h and mean contrail age $\bar{t}$ of ½ h together with a estimated potential contrail coverage c_{pot} of 0.2 is used to calculate the expected values. The data was sampled into 7 classes of air traffic density with logarithmic class boundaries to account for the data distribution. c_0 in Eq. (3) is matched to result in the same mean cirrus coverage as in the data except for the class with the lowest air traffic density. This class comprises nearly 40% of all pixels. The cirrus coverage of this class therefore dominates the mean value, while the classes with low air traffic density (d<0.1[km/km2/h]) show lower values. Due to the spatial and temporal coherence of the air traffic data these values seem to represent the cirrus coverage without essential influence of air traffic better then the values at d=0. With both methods of cirrus detection the mean cirrus coverage is 0.03 higher then c_0 , which results in a 14% higher cirrus coverage due to air traffic with the first cirrus detection method and in a 11% increase with the second method (thin cirrus).

Independent from any cirrus classification the equivalent blackbody temperature measured by the satellite shows also the expected variation with air traffic density. In both channels significantly lower temperatures are found at times and in areas with high air traffic density than in low traffic regions (Fig. 3, right). Again the class with air traffic close to zero deviates from the overall picture. Its mean temperature is close to the overall mean temperature and lower than the temperature of the low air traffic classes. Air traffic is positively correlated with land surface and daytime, both being warmer in summer and autumn, which would result in the opposite behaviour in the infrared data if this would not be masked by additional cirrus clouds.
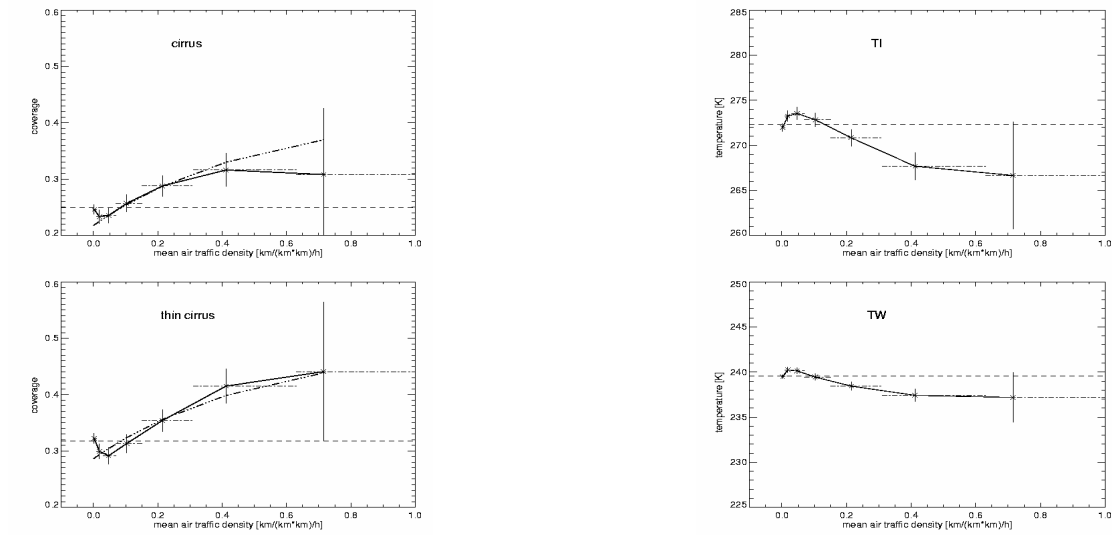

Figure 3: Cirrus coverage as a function of air traffic density. Two different versions of cirrus detection from METEOSAT data show a strong increase of cirrus cloudiness with increasing air traffic density. (Left side). Plotted is in each figure the mean cirrus coverage within seven air traffic density classes indicated by the dash-dotted horizontal bars. The vertical bars indicate the range of confidence for the single air traffic density classes, the horizontal dashed line the mean value of cloud coverage as defined by the algorithm. The theoretical cirrus coverage is indicated by the thick dash-dot-dotted curve. Equivalent mean blackbody temperature in the infrared (IR, left) and water vapour (WV, right) channel of METEOSAT data as a function of air traffic density are plotted on the right hand side.

5 CONCLUSIONS AND OUTLOOK

The statistical method to derive the cirrus coverage depending on air traffic density does not allow to infer the optical properties of these additional clouds. Thus it is not possible to calculate their radiative impact without further information. The analysis of linear contrails from NOAA14 AVHRR data for Central Europe (Meyer, R. & HM, in preparation) using an automated contrail detection algorithm described in Mannstein (1999) results in a mean contrail coverage for the same period and nearly the same area of 0.3%. Therefore it can be stated, that the coverage by additional cirrus clouds is in Europe about 10 times higher than by linear contrails. The optical depth of these additional cirrus cannot be less then 0.2, the optical depth usually attributed to linear contrails, otherwise they would not be detected by METEOSAT. Therefore we have to conclude, that the impact of the additional cirrus clouds is at least 10 times the effect of the linear contrails.

The high amount of contrail cirrus compared to linear contrails indicates, that the lifetime of contrail cirrus has to be measured in hours rather then in minutes. This leads to an additional temporal effect, which has not been considered in previous studies. During daylight conditions the cooling effect of cirrus clouds due to enhanced reflection nearly balances the warming effect in the infrared part of the spectrum, while after sunset only the warming effect is remaining. The cloud coverage by cirrus clouds resulting from contrails has a considerable time lag behind the air traffic. Therefore part of the impact of air traffic over Europe is shifted to the night hours, where only the warming effect of cirrus clouds is remaining.

In future studies it will be necessary to consider a further, secondary contrail effect. The additional ice particles formed in contrails can either lead to an enhanced net sedimentation rate resulting in a dryer upper troposphere, or to a reduced one, as the particles formed in contrails are smaller and therefore slower. The details of these processes depend strongly on the vertical motion and the small scale structure of the moisture field in this altitudes, which are both not known sufficiently.

REFERENCES

Bakan, S., Betancor-Gothe, M., Gayler, V. & Grassl, H., 1994, Contrail frequency over Europe from NOAA-satellite images. *Ann. Geophys.,* 12, 962-968.

Boucher, O., 1999. Air traffic may increase cirrus cloudiness. *Nature*, 397,30-31.

Freudenthaler, V., Homburg, F. and Jäger, H., 1995. Contrail observations by ground-based scanning lidar: cross-sectional growth. *Geophys. Res. Lett.*, 22,3501-3504

Gierens, K., Schumann, U., Helten, M., Smit, H. and Marenco, A., 1999. A distribution law for relative humidity in the upper troposphere and lower stratosphere derived from three years of MOZAIC measurements. *Ann. Geophys.,* 17,1218-1226

Gierens, K., Schumann, U., Helten, M., Smit, H. and Wang, P., 2000. Ice-supersaturated regions and subvisible cirrus in the northern midlatitude upper troposphere. *J. Geoph.. Res.,* 105(D18), 22,743-22,753

Intergovernmental Panel on Climate Change (IPCC), 1999. *Aviation and the Global Atmosphere*. edited by J. E. Penner et al., Cambridge Univ. Press.

Liou, K.N. Influence of cirrus clouds on weather and climate processes: a global perspective. *Mon. Wea. Rev.,* 114, 1167-1198 (1986).

Mannstein, H., Meyer, R. & Wendling, P., 1999 Operational detection of contrails from NOAA-AVHRR-data, *Int. J. Remote Sensing*, 20(8), 1641-1660.

Minnis, P., Young, D. F., Garber, D. P., Nguyen, L. N., Smith, W. L. Jr., and Palikonda, R.. 1998 Transformation of contrails into cirrus during SUCCESS, *Geophys. Res. Lett.,* 25(8), 1157-1160

Sausen, R. and U. Schumann, 2000 *Estimates of the Climate Response to Aircraft CO_2 and NO_X Emissions Scenarios,* Climatic Change 44, 27-58.

Schumann, U., 1994: On the effect of emissions from aircraft on the state of the atmosphere. *Ann. Geophys.* 12, 365–384.

Schumann, U., 1996. On conditions for contrail formation from aircraft exhausts. *Met. Zeitschr.,N.F.,* 5, 4-23

Schumann, U., 2002. Contrail cirrus. In Lynch et al.(Ed.):*Cirrus*, Oxford University Press, 231-255.

Potential Impact of Aviation-Induced Black Carbon on Cirrus Clouds: Global Model Studies with the ECHAM GCM

J. Hendricks[*], B. Kärcher
DLR-Institut für Physik der Atmosphäre, Oberpfaffenhofen, Germany

A. Döpelheuer
DLR-Institut für Antriebstechnik, Köln-Porz, Germany

J. Feichter
Max-Planck-Institut für Meteorologie, Hamburg, Germany

U. Lohmann
Dalhousie University, Halifax, Canada

Keywords: Aviation, Black carbon, Cirrus

ABSTRACT: In this study, global simulations on the potential impact of aircraft-generated black carbon (BC) particles on cirrus clouds via heterogeneous nucleation were performed. The general circulation model ECHAM4 has been applied including predictions of major aerosol species and cloud condensate. In a first step, the global impact of aircraft BC emissions on the availability of potential heterogeneous ice nuclei (IN), such as BC or mineral dust particles, in the upper troposphere and lowermost stratosphere (UTLS) was quantified. The results suggest a significant large-scale contribution of aviation to the number concentration of potential heterogeneous IN. This indicates the possibility that aviation-induced BC can impact cirrus cloud formation. Hence, in a second step, potential impacts of aircraft BC particles on cirrus clouds were simulated. Sensitivity experiments were performed considering various scenarios of ice nucleating efficiencies of different types of potential heterogeneous IN. The model experiments indicate a potential of aviation-induced BC to induce significant perturbations in cirrus microphysical properties.

1 INTRODUCTION

Potential impacts of aviation-induced aerosols on cirrus occurrence frequency and cirrus optical properties have been discussed (e.g., IPCC, 1999). Aircraft exhaust particles, especially BC and sulphate aerosols, may perturb the aerosol population of the UTLS and may act as ice nuclei via heterogeneous or homogeneous ice nucleation. Recent studies suggest that the impact of aircraft sulphur emissions on cirrus properties via homogeneous freezing of sulphate aerosols is probably small (e.g., Lohmann and Kärcher, 2002). Hence, the question has been addressed whether aircraft-generated BC particles serving as heterogeneous IN may have a significant impact on cirrus cloudiness and cirrus microphysical properties.

No consistent physically-based quantification of the relative aviation impact on the availability of potential heterogeneous IN, such as BC and mineral dust particles, in the UTLS has been performed yet. Therefore, simulations on the contribution of surface sources as well as aircraft BC emissions to the total amount of BC and dust particles in the UTLS were performed here using a global model. Since the simulations indicate a potential of aviation to induce significant perturbations of the UTLS heterogeneous IN budget, the sensitivity of cirrus microphysical properties to aviation BC emissions was investigated in additional model experiments.

---

[*] *Corresponding author:* Johannes Hendricks, DLR-Institut für Physik der Atmosphäre, Oberpfaffenhofen, D-82234 Wessling, Germany. Email: Johannes.Hendricks@dlr.de

2 MODEL AND METHODOLOGY

The general circulation model ECHAM4 was applied including predictions of major aerosol species and cloud condensate (Feichter et al., 1996; Lohmann et al., 1999; Lohmann and Kärcher, 2002). The model treats the atmospheric cycles of sulphate aerosols, carbonaceous particles (organic carbon as well as BC), sea-salt, and mineral dust aerosols. Prognostic fields of particle mass concentrations of the respective aerosol types are calculated considering emissions of particles and particle precursors, gas-to-particle conversion, transport, and removal by wet and dry deposition. The BC emission sources considered include fossil fuel combustion as well as biomass burning. In order to calculate particle number concentrations from the simulated aerosol mass concentrations, prescribed lognormal particle size distributions typical for the respective aerosol type (Hess et al., 1998) are employed.

For the present study, the model was extended by aircraft BC emissions calculated from global aviation fuel consumption data for 1992 (DLR2 inventory) including the global distribution of aircraft fuel use and its annual cycle. BC mass and particle number emission rates are derived from these data employing altitude dependent aircraft BC mass and particle number emission indices (Döpelheuer, 2002). In order to assess the relative contribution of aviation to the total UTLS aerosol budget, aircraft-induced BC is treated separately from BC resulting from surface sources. The aviation-induced BC number concentration is calculated by considering the number-to-mass ratios typical for the fresh exhaust as well as by taking into account potential reductions in the number-to-mass ratio owing to interactions with background aerosols and cloud particles. A comparison of the results obtained with this model set-up to observational data of UTLS BC mass concentrations suggests a fair representation of the UTLS BC budget in the model. In regions where a relevant aviation impact on UTLS BC is simulated, the BC concentrations observed by Blake and Kato (1995) mostly agree within a factor of 2 with the corresponding modelled values.

Homogeneous ice nucleation is considered as described by Lohmann and Kärcher (2002). Heterogeneous instead of homogeneous nucleation can be considered by transforming the available heterogeneous IN into ice crystals at prescribed supersaturations. The mechanisms of cirrus cloud formation are still not well understood. Especially the details of the competition between homogeneous and heterogeneous ice nucleation as well as the ice nucleating efficiency of the different types of potential heterogeneous IN are still uncertain. In order to cope with these deficiencies in the present study, maximum potential aviation impacts on cirrus microphysical properties were estimated rather than quantifying the effect in detail. The following assumptions on ice cloud formation were made promoting the aviation impact: i) The maximum number concentration of aviation BC particles was assumed (number-to-mass ratios of fresh exhaust); ii) Heterogeneous instead of homogeneous nucleation is assumed at ice supersaturations larger than 130%, provided that the number of heterogeneous IN exceeds $0.5/cm^3$ (Gierens, 2003); iii) BC particles from aviation generally serve as efficient heterogeneous IN; iv) The number of ice crystals formed during nucleation events can be limited by the vertical velocity. However, the sub-grid vertical velocity is a very uncertain parameter in a global model. This can lead to underestimations of the potential aviation impact on ice clouds. Therefore we limit the number of heterogeneously formed ice crystals by the number heterogeneous IN available and not by the number predicted from the vertical velocity.

Two different scenarios were considered. In scenario 1, all BC and mineral dust particles available are assumed to serve as heterogeneous IN. This leads to heterogeneous nucleation dominating homogeneous nucleation in the northern hemisphere (NH). Simulations including/excluding aviation BC emissions were compared. In scenario 2, a model experiment where heterogeneous nucleation can exclusively occur on BC from aviation is compared to a simulation considering homogeneous nucleation only. All model runs were performed for a 10 year time period. A horizontal resolution of approximately 3.75x3.75 degrees is considered. The vertical range from the surface up to 10 hPa is covered by 19 layers. Note that aerosol impacts on the sub-grid-scale ice cloud coverage were not taken into account here.
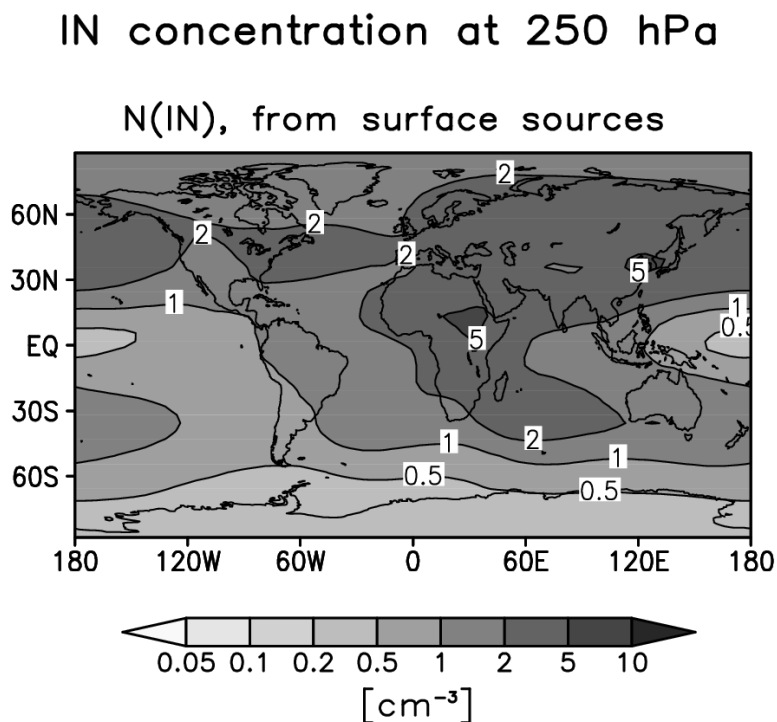
IN concentration at 250 hPa

N(IN), from surface sources

Figure 1: Annual mean number concentrations [$1/cm^3$] of potential heterogeneous IN (BC and mineral dust particles) at 250 hPa (main aircraft flight level). Only particles originating from surface sources are considered.

3 RESULTS AND DISCUSSION

The annual mean global distribution of the number concentration of potential heterogeneous IN particles (BC and mineral dust) simulated for the 250 hPa pressure level is shown in Figure 1. The 250 hPa level is chosen since it is located within the main flight levels. Only particles originating from the surface are considered. The annual mean concentrations of these particles at 250 hPa range between about 0.5 and 5 particles/cm^3. BC particles generally contribute to more than 50% (more than 70% at mid- and high latitudes) to these particle numbers. The major emission regions of BC from fossil fuel combustion are North America, Europe, and Southeast Asia. Due to upward transport of BC from the boundary layer, the plumes of these emission regions can clearly be identified at 250 hPa showing a significant spatial shift induced by westerly flows. The potential UTLS IN populations in the northern hemispheric equatorial regions as well as the southern hemisphere (SH) are to a larger extent influenced by BC emissions from biomass burning. The contribution of mineral dust particles is largest at low latitudes.

Large-scale number concentrations of aircraft-induced BC particles simulated for 250 hPa are highlighted in Figure 2. When reductions in the BC number-to-mass ratio due to ageing of aircraft exhaust (Section 2) are not considered, a maximum potential impact of aviation on the number concentration of UTLS BC particles or heterogeneous IN can be estimated. As displayed in Figure 2a, the maximum-estimate number concentrations of aircraft-generated BC particles at 250 hPa range between about 0.2 and 1/cm^3 at northern midlatitudes where most of the aircraft activity takes place. Taking into account the number concentrations obtained for surface-related potential IN (Figure 1), this maximum estimate results in a relative increase in the potential IN number concentration at 250 hPa of more than 20% in large parts of the NH. The largest increase at 250 hPa ranges up to 40%. Even when an efficient exhaust ageing is considered (Figure 2b), the aviation-induced increase in the potential IN number concentration at 250 hPa exceeds 10% in large parts of the NH and amounts up to 20% in the most frequented flight areas. Hence, the simulations indicate a large potential of BC from aircraft to contribute significantly to the UTLS IN particle number concentration. Note that despite the large potential perturbations in IN number concentration, the aviation impact on the BC or potential IN mass concentration is small due to the comparably small sizes of BC particles from aviation.

IN concentration at 250 hPa

a)   N(BC), from aircraft, maximum

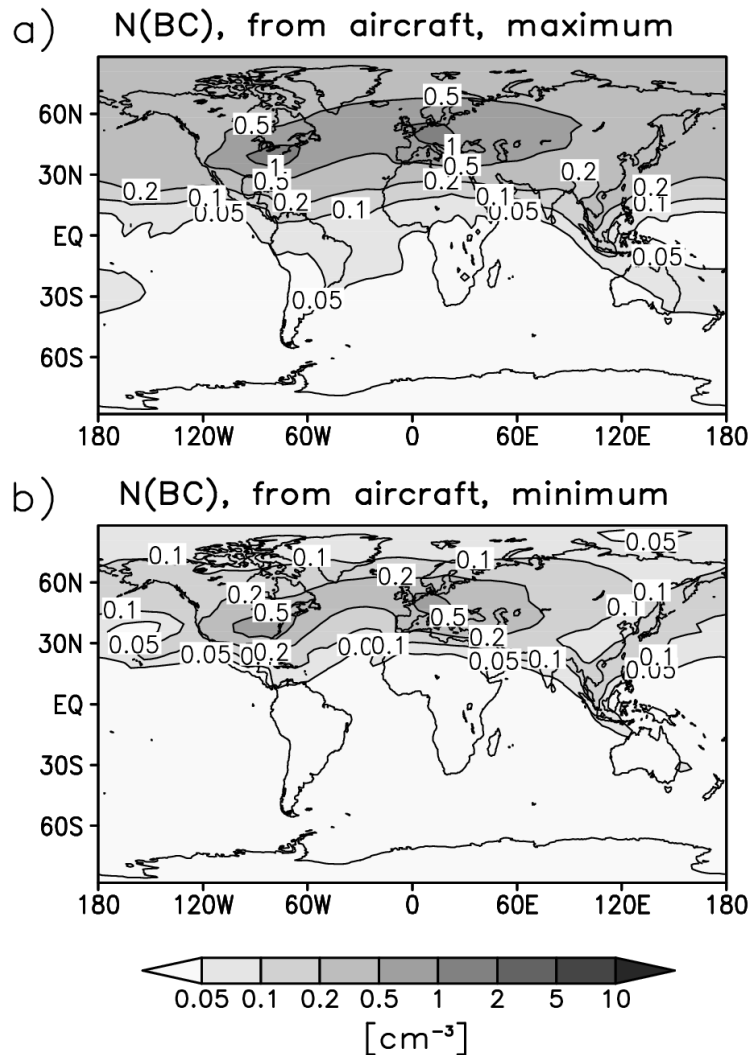### b)   N(BC), from aircraft, minimum

Figure 2: As Figure 1, but for BC particles from aircraft. a) BC number-to-mass ratios of fresh aircraft exhaust were considered. b) An efficient reduction of the aviation BC particle number-to-mass ratio during exhaust ageing was assumed.

Regarding the large potential aviation-induced increases in the heterogeneous IN number concentration, it should be evaluated whether these perturbations can result in significant changes in cirrus microphysical properties. As mentioned in Section 2, two different scenarios were considered to simulate maximum potential impacts of BC from aviation on ice cloud properties. Figure 3 highlights maximum estimates of the relative aviation impact on the annual mean ice crystal number concentration simulated for 250 hPa where the aircraft impact is largest. Note that typical annual mean (including cloud-free periods) ice crystal number concentrations simulated in the two scenarios range between 0.1 and 0.5/cm^3 at the NH midlatitude 250 hPa level. The corresponding annual mean ice cloud frequencies range between 20 and 40%. In scenario 1 (Figure 3a), mineral dust particles and BC particles in general serve as heterogeneous IN. In this case, cirrus formation is dominated by heterogeneous nucleation in the NH since the NH UTLS number concentrations of heterogeneous IN mostly exceed 0.5/cm^3 (Section 2). In agreement with the aircraft-induced increase in the heterogeneous IN concentration aviation BC emissions lead to an increase in ice crystal number concentration. Large increases are simulated which locally exceed 40%. The relative annual mean perturbation of ice crystal number density can be larger compared to the annual mean perturbation of heterogeneous IN since the ice cloud frequency is largest during winter when the IN perturbation exceeds its annual mean.
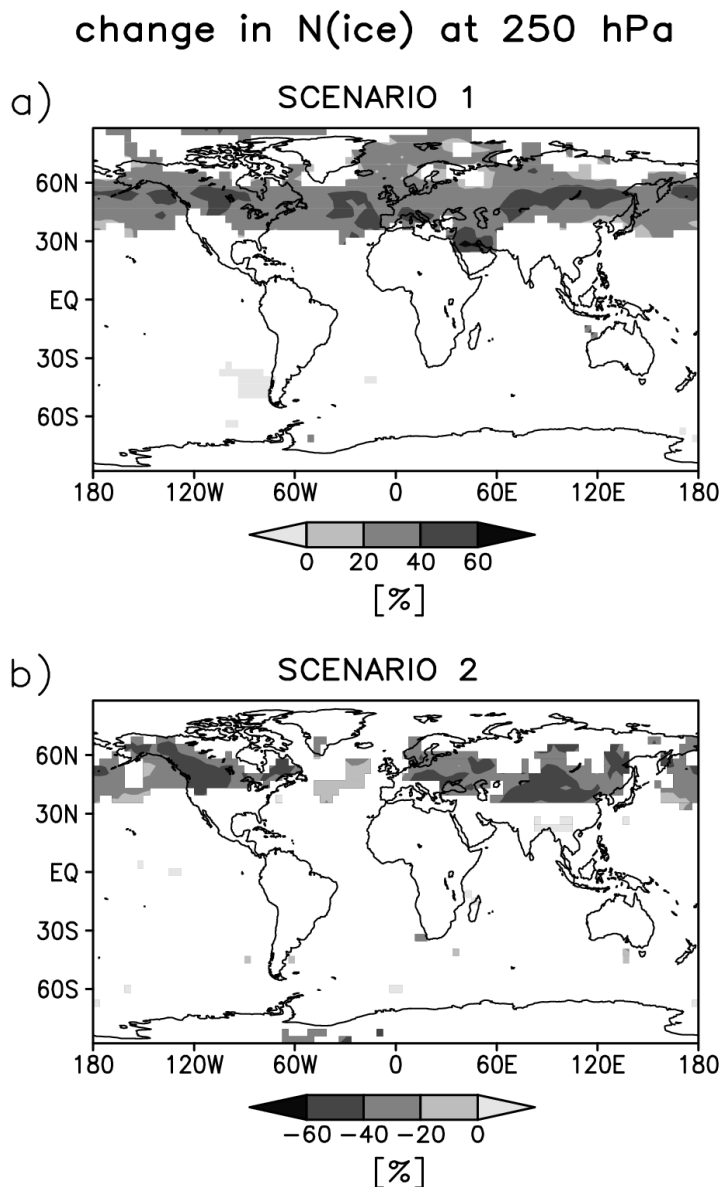
change in N(ice) at 250 hPa

Figure 3: Relative change of the annual mean ice crystal number concentration induced by heterogeneous ice nucleation on BC particles from aviation, simulated in scenario 1 (a) and scenario 2 (b). Only those changes are shown which are significant on a 95% level of the student t-test. The results represent maximum estimates of potential aviation impacts.

In scenario 2, heterogeneous nucleation can occur on aviation-induced BC only (Section 2). The impact of heterogeneous nucleation in the corresponding model experiment is to compete with homogeneous nucleation, provided that sufficient amounts of BC from aviation are available. Figure 2b reveals that aviation causes a reduction of the ice crystal number concentration under these assumptions. The reduction is largest (>40%) in areas of strong orographic forcing where large updrafts lead to high ice crystal number concentrations resulting from homogeneous nucleation when ice formation on aviation BC is neglected. In both scenarios, the aviation impact is significant in large areas of the northern hemisphere. The aircraft-induced increases/decreases in the ice crystal number concentration are accompanied by decreased/increased crystal sizes. No significant aviation-induced changes in the ice water content were simulated.

4 CONCLUSIONS

The simulations performed here reveal that the large-scale impact of aviation BC emissions on the UTLS BC mass concentration is small. Nevertheless, the simulations suggest a significant aviation

impact on the number concentrations of UTLS BC particles and potential heterogeneous IN (BC and mineral dust particles). Large-scale increases of the potential heterogeneous IN number concentration of up to 50% were simulated. Maximum estimates of the potential impacts of aviation BC on cirrus microphysical properties were performed. Provided that BC particles from aviation serve as efficient heterogeneous IN, maximum increases or decreases in ice crystal number concentrations of more than 40% were simulated assuming that 'background' (no aviation impact) cirrus cloud formation is dominated by heterogeneous or homogeneous nucleation, respectively.

The uncertainties on the details of cirrus cloud formation are currently too large for a more detailed quantification of the aviation impacts on ice cloud properties. Further in-situ observations of aerosols and cirrus as well as laboratory measurements on ice particle formation and the nucleation ability of different aerosol types are urgently required to constrain future global model scenarios. The representation of aerosols in global models should be improved by including prognostic aerosol size distributions and composition. The representation of ice clouds should be further improved by i) considering more detailed parametrizations of ice nucleation mechanisms and subscale vertical fluxes; ii) including aerosol impacts on subscale ice cloud coverage; and iii) considering the dispersion of contrails to cirrus clouds.

REFRENCES

Blake, D.F., and K. Kato, 1995: Latitudinal distribution of black carbon soot in the upper troposphere and lower stratosphere, *J. Geophys. Res.*, *100*, 7195-7202.

Döpelheuer, A., 2002: *Anwendungsorientierte Verfahren zur Bestimmung von CO, HC und Ruß aus Luftfahrttriebwerken*, thesis, Deutsches Zentrum für Luft- und Raumfahrt, Report 2002-10, ISSN 1434-8454, Cologne, Germany.

Feichter, J., E. Kjellström, H. Rodhe, F. Dentener, J. Lelieveld, and G.-J. Roelofs, 1996: Simulation of the tropospheric sulfur cycle in a global climate model, *Atmos. Environ.*, *30*, 1693-1707.

Gierens, K., 2003: On the transition between heterogeneous and homogeneous freezing, *Atmos. Chem. Phys.*, *3*, 437-446.

Hess, M., P. Köpke, and I. Schult, 1998: Optical properties of aerosols and clouds: The software package OPAC, *Bull. Americ. Met. Soc.*, *79*, 831-844.

Intergovernmental Panel on Climate Change (IPCC), 1999: *Aviation and the Global Atmosphere*, edited by J. Penner *et al.*, Cambridge Univ. Press, New York.

Lohmann, U., and B. Kärcher, 2002: First interactive simulations of cirrus clouds formed by homogeneous freezing in the ECHAM GCM, *J. Geophys. Res*, *107*, 4105, doi:10.1029/2001JD000767.

Lohmann, U., J. Feichter, C.C. Chuang, and J.E. Penner, 1999: Prediction of the number of cloud droplets in the ECHAM GCM, *J. Geophys. Res.*, *104*, 9169-9198.